University of Bremen
Faculty 01: Physics / Electrical Engineering

MASTER THESIS

Lukas Grosch

Investigation of the Greenhouse Gas Emissions from the Steel Production Site in Bremen

Institute for Environmental Physics IUP
Department for Remote Sensing

Supervisor of the master thesis:	Prof. Dr. Thorsten Warneke
Second Supervisor:	PD Dr. Andreas Richter
Study programme:	Environmental Physics M. Sc.

Bremen 2024

Investigation of the Greenhouse Gas Emissions from the Steel Production Site in Bremen

Lukas Grosch

Abstract

This thesis investigates the greenhouse gas (GHG) emissions from the steel production site in Bremen using the EM27/SUN spectrometer together with the IFS 125HR spectrometer and other supportive methods. The research focuses on measuring carbon monoxide (CO) and carbon dioxide (CO_2) emissions at varying distances from the source of emission, with the objective of determining the CO/CO_2 emission ratio. Three methodologies are presented for the effective quantification of these emissions: stack tip measurements, ratio estimation from absolute emission values, and from differential emission values. The calculated emission ratio exhibits slight discrepancies across the various methodologies, yet it consistently falls within the range of 1.0 to 2.05 % with an estimated best value of 1.54 ± 0.85 %. This ratio represents the emissions from the entire steel production site including the furnace gas fired power plants and may potentially be applied to use CO measured by spaceborne remote sensing as a proxy for CO_2 emissions. Moreover, the findings indicate that measurements from more distant stations provide a more consistent emission ratio than those taken in close proximity, given the high temporal and spatial variability of the plume. In order to enhance the analysis, Lagrangian transport models were employed to simulate the properties of the emission plume. The simulations demonstrate the potential for total emission estimates through inversion. Furthermore, the integration of the EM27/SUN spectrometer with a Differential Optical Absorption Spectroscopy (DOAS) instrument provides a comprehensive approach to the validation and improvement of GHG emission estimates. The findings of this study contribute to the field of atmospheric research by presenting an approach for measuring GHG emissions from individual emission sources, which can be adapted for broader environmental monitoring applications.

Acknowledgements

I would like to express my gratitude to my primary supervisor, Prof. Dr. Thorsten Warneke, for providing guidance throughout this project, accompanying me to the measurement stations at the steel plant and providing me with all the necessary facilities for the research.

I would also like to thank PD Dr. Andreas Richter for sharing expertise, and valuable guidance.

I place on record, my sincere thank you to Dr. Alexandra Klemme who especially at the beginning of the project provided helpful suggestions and ideas.

I wish to acknowledge the invaluable assistance provided by Dr. Winfried Markert and Dr. Christof Petri in adressing technical questions that arose during the experiments.

I am also indebted to Dr. Alexandros Panagiotis Poulidis, Dr. Kezia Lange, Thomas Visarius, and Jonas Hachmeister for their contributions in their respective specialised fields.

I take this opportunity to express gratitude to all of the faculty members for their help and constructive discussions.

I also thank my parents and my brother for the unceasing encouragement, support and attention.

I am also grateful to Elli and Martin who supported me through this venture.

Contents

Chapter 1

Introduction

In order to tackle one of the most important challenges of the modern world, climate change, the global society has to achieve better understanding of the underlying processes, driving forces and complex interrelations. A major contributor to global warming are GHGs, such as CO_2, methane (CH_4), water vapour (H_2O), and nitrous oxide (N_2O). Despite an atmospheric CO_2 concentration of just 417 parts per million (ppm) in 2022, it accounts for the majority of the anthropogenic greenhouse effect (NOAA 2023). And the concentration keeps rising since 1850, when it stood at approximately 280 ppm. Similar trends are observed for the other GHGs (Meinshausen et al. 2017). Without significant reductions in GHG emissions, global temperatures are projected to rise by up to 3.6°C until 2100 as the best estimate (Scenario SSP3-7.0 in Climate Change (IPCC) 2023).

The increase in global mean temperature has already resulted in several effects, including rising sea levels (Fox-Kemper et al. 2021), more frequent and severe extreme weather events (Seneviratne et al. 2021), and changes in the hydrological cycle, which increase the likelihood of droughts (Douville et al. 2021). Recognizing the urgent need to reduce GHG emissions, political leaders worldwide have committed to limiting global warming to well below 2°C under the Paris Agreement (United-Nations 2015). Achieving this goal requires precise knowledge of GHG concentrations and effective monitoring of their sources and sinks.

In order to monitor GHG emissions, two primary approaches are used: the bottom-up approach and the top-down approach. The bottom-up approach involves creating emission inventories based on natural sources and sinks (Schulze 2006; Hodson et al. 2011), as well as fossil fuel consumption statistics. However, the accuracy of bottom-up inventories is limited by the precision of the data on both natural and anthropogenic sources.

The top-down approach relies on direct measurements of GHG concentrations in the atmosphere and complements the bottom-up method. These measurements can be obtained through in-situ observations, such as those conducted by the Integrated Carbon Observation System (ICOS) network in Europe (Bergamaschi et al. 2022). However, in-situ measurements offer limited global coverage and do not capture variations at different atmospheric heights. Satellites, such as the Japanese Greenhouse gases Observing SATellite (GOSAT) (Yokota et al. 2009) and the European

TROPOspheric Monitoring Instrument (TROPOMI) onboard the Sentinel-5 precursor satellite (Veefkind et al. 2012), provide an alternative by offering quasi-global coverage of column-averaged dry-air mole fractions (DMF). These data are crucial for estimating the emission strengths of various sources worldwide (e.g. Tu et al. 2022a; Cusworth et al. 2021).

Ground-based reference measurements are essential in order to verify the satellite data by correcting for spatial bias and temporal drifts. Additionally, these reference measurements are needed in order to tie the data to the standards defined by the World Meteorological Organisation (WMO) (Hall et al. 2021). Fourier Transform Infrared (FTIR) spectrometers, which operate on principles analogous to those employed by satellites, are optimal for this purpose. There are three principal FTIR networks: the Infrared Working Group (IRWG) of the Network for Detection of Atmospheric Composition Change (NDACC) (Kurylo 1991), the Total Carbon Column Observing Network (TCCON) (Wunch et al. 2011), and the Collaborative Carbon Column Observing Network (COCCON) (Frey et al. 2019). The NDACC-IRWG operates within the mid-infrared (MIR) spectral range, whereas the TCCON and the COCCON concentrates on the near-infrared (NIR) range.

The TCCON network employs 32 Bruker IFS 125HR spectrometers around the globe. They operate on an optical path difference (OPD) of 418 mm. Consequently, they offer high-resolution measurements with a spectral resolution of 0.02 cm^{-1} but are of considerable size and weight. The operation of such an instrument is only possible at sites with good infrastructure providing a reliable power supply and experienced personal (Kivi et al. 2016). The COCCON network uses the portable EM27/SUN spectrometer, which was developed in 2012 by the Institute for Meteorology and Climate Research - Atmospheric Trace Gases and Remote Sensing (IMK-ASF) in collaboration with Bruker. This lightweight instrument allows for measurements with a spectral resolution of 0.5 cm^{-1} conducted by a single person (Gisi et al. 2012).

A challenge remains in estimating the CO_2 emissions of individual emitters, such as industrial plants. Satellites face limits in their spatial resolution because CO_2 is well-mixed in the atmosphere resulting in small signals relative to large background values. Ground-based instruments do not supply the necessary temporal and spatial coverage for long-time observation. However, monitoring these emissions and verifying their reported values is crucial for several reasons, including ensuring regulatory compliance, maintaining accuracy in emissions data, and holding industries accountable for their environmental impact.

One potential solution is an approach that employs a trace gas to quantify CO_2 emissions based on a specified emission ratio (Wu et al. 2022; MacDonald et al. 2023). The majority of industrial plants co-emit CO as a by-product of incomplete combustion. In contrast to CO_2, this gas can give emission signals that are large enough for satellite observation, and its atmospheric lifetime of 1-2 months makes it suitable for the tracing of the plume. In a recent study, Schneising et al. 2024 determined a sector-specific CO/CO_2 emission ratio for steel plants in Germany. Steel industry facilities represent ideal candidates for testing this approach, as they are

not only among the most significant industrial contributors to global anthropogenic CO_2 emissions but also emit considerable quantities of CO. The study yields a sector specific CO/CO_2 ratio for the five investigated steel plants of 3.24 % (2.72 % - 3.89 %, 1σ) in a mass fraction, corresponding to a ratio of 5.09 % (4.27 % - 6.11 %, 1σ) considering the number of molecules. However, the findings have yet to be verified through ground-based measurements.

This thesis investigates the utilisation of the transportable EM27/SUN FTIR spectrometer for measurements in close proximity to the steel plant in Bremen and the employment of the IFS 125HR spectrometer at the University of Bremen for this purpose. The objective is to quantify the CO and CO_2 emissions and the CO/CO_2 ratio, which can then be used in conjunction with satellite observations to enhance the precision of CO_2 emission estimation. Moreover, additional techniques are examined with the objective of improving the estimation of emissions from individual sources. By combining various ground-based measurement techniques, this thesis aims to enhance our ability to monitor and manage industrial GHG emissions, thereby contributing to the broader effort to mitigate climate change.

Chapter 2

Theoretical Background

2.1 The Earth's Atmosphere and Climate Change

The Earth's atmosphere plays a crucial role in sustaining life by providing essential gases, blocking harmful ultraviolet (UV) - radiation, and regulating surface temperatures. This overview covers the composition, structure, and key processes affecting the atmosphere, including the greenhouse effect and climate change.

The atmosphere is composed of major gases that exhibit minimal spatial and temporal variability and trace gases with greater spatial and temporal fluctuations. Major gases constitute 99.9 % of the atmosphere's dry-air volume and include nitrogen (N_2, 78.09 %), oxygen (O_2, 20.95 %), and argon (Ar, 0.93 %) (Roedel et al. 2017). The remaining 0.1 % is comprised of trace gases, including CO_2 (421 ppm), CH_4 (1922 parts per billion (ppb)), and N_2O (337 ppb) (Lan et al. 2024). Water vapor is also a significant constitute of the atmosphere, although its concentration fluctuates between 1 % and 4 % depending on temperature (Klose et al. 2016). Other trace gases, such as CO, also play an important role, albeit in smaller amounts.

Despite their relatively minor volumetric fraction, trace gases exert a significant influence on atmospheric properties due to their distinctive physical and chemical characteristics. For instance, they contribute to the heating of the atmosphere and the absorption of UV-radiation (Möller 2019).

In order to quantify this influence, the structure of the atmosphere has to be described first. The atmosphere's vertical structure is defined by both pressure and temperature. Under the assumption that the atmosphere is comprised of an ideal gas in hydrostatic balance, a mathematical expression for the pressure profile can be derived. The equation reads

$$p(z) = p_0 \cdot \exp\left(-\int_0^z \frac{g(z') \cdot M}{N_A \cdot k_B \cdot T(z')} \cdot dz'\right) \tag{2.1}$$

representing the pressure p at a certain height z with respect to a ground pressure p_0 at sea level. Within this equation k_B is Boltzmann's constant, N_A is Avogadro's constant and $M = 0.02897\,\mathrm{kg\,mol^{-1}}$ is the molar mass of dry-air. The ratio $\frac{N_A \cdot k_B \cdot T(z')}{g(z') \cdot M}$ is frequently referred to as the scale height $H(z')$. It accounts for the

height dependence of the temperature T and the gravitational acceleration g. Under standard conditions, it can be approximated as 8.5 km (see Roedel et al. 2017 for a more detailed derivation).

The temperature in the atmosphere does not follow a decreasing trend with height. Instead the atmosphere is divided into layers from Earth surface to increasing altitudes, namely the troposphere (up to 6 to 18 km), stratosphere (up to 50 km), mesosphere (up to 80 km), thermosphere (up to 500 to 1000 km), and exosphere. Each layer exhibits a unique temperature gradient. This gradient shows a change in sign after each layer starting with a declining temperature with increasing altitude in the troposphere (Efremenko et al. 2021; Klose et al. 2016).

The Earth's climate is determined by the energy balance between incoming solar radiation and outgoing terrestrial radiation. The solar constant, $S_0 \approx 1360$ W/m^2, represents the power flux density of the Sun at the Earth's orbit (Crommelynck et al. 1996; Fröhlich et al. 2004). The average power flux S absorbed by the Earth, accounting for its spherical shape, is given by the following equation:

$$S = \frac{S_0}{4} \approx 340\text{W/m}^2 \tag{2.2}$$

The total power emitted can be described by the Stefan-Boltzmann law for a black body:

$$F = \sigma \cdot T^4 \tag{2.3}$$

where $\sigma \approx 5.67 \times 10^{-8}$ W m^{-2}K^{-4} is the Stefan-Boltzmann constant and T is temperature (Roedel et al. 2017; Efremenko et al. 2021). In order to account for the fact that a real object like the Earth is not a black body, the emissivity ϵ is introduced, representing the radiation efficiency of the material, as well as the albedo A, taking into account that not all radiation is absorbed but is also reflected back. By setting the absorbed and emitted radiation equal, it is possible to calculate the surface temperature T_s:

$$\frac{S_0}{4} \cdot (1 - A) = \epsilon_s \cdot \sigma \cdot T_s^4 \longrightarrow T_s^4 = \frac{S_0}{4} \cdot \frac{1 - A}{\epsilon_s \cdot \sigma} \tag{2.4}$$

Treating the Earth as a thermal emitter with $A = 0.3$ and $\epsilon_s = 0.95$, this yields a theoretical surface temperature of about 258 K (-15 °C), which is lower than the observed mean temperature of 288 K (15 °C) (Jones et al. 1999).

The difference between the theoretical and observed temperatures can be attributed to the greenhouse effect. In a simplified model that does not include an atmosphere, the Earth would be considerably colder. It disregards thermal emitters in the atmosphere, which absorb and re-emit long-wave radiation. The equations that govern this are as follows:

$$\epsilon_s \cdot \sigma \cdot T_s^4 = (1 - A) \cdot \frac{S_0}{4} + \epsilon_a \cdot \sigma \cdot T_a^4 \tag{2.5}$$

$$\epsilon_s \cdot \sigma \cdot T_s^4 = (1 - \epsilon_a) \cdot \sigma \cdot T_s^4 + 2 \cdot \epsilon_a \cdot \sigma T_a^4 \tag{2.6}$$

where ϵ_a and T_a are the emissivity and temperature of the atmosphere, respectively. Solving these equations with $\epsilon_a = 0.75$ yields a more accurate surface temperature of approximately 287 K (13.85 °C) (Jones et al. 1999).

Thermal emitters dominating the greenhouse effect, including CO_2, CH_4, and N_2O, are called greenhouse gases (GHGs). The short-wave radiation emitted by the Sun can penetrate through these gases whereas the long-wave radiation emitted by the Earth is absorbed by them, resulting in an additional warming of Earth's surface by trapping heat in the atmosphere. This natural process is in first place essential for life on Earth but is being intensified by human activities, leading to global climate change. The concentrations of GHG increased significantly due to the burning of fossil fuels since the beginning of the industrial era. For example CO_2 has increased from approximately 280 ppm in 1850 to 421 ppm in 2023.

It is crucial to monitor the levels of greenhouse gases in the atmosphere as a key aspect of combating and monitoring climate change. This thesis will contribute to this endeavour by enhancing the quality of remote sensing measurements of point sources for CO_2.

2.2 Molecular Spectroscopy

The absorption of radiation in the atmosphere originates in the interaction between molecules and electromagnetic radiation. Absorption of radiation leads to an excitement of the molecule into a higher state of energy which can be de-excited to a lower state by emission of radiation. Treating the molecule as a quantum mechanical system shows that its energy can only be at discrete levels. Only radiation matching the energy difference (and hence frequency) between two levels can be absorbed or emitted. The properties of these energy levels are described in the following section based on Demtröder 2018 and Wolf et al. 2006.

For the general case of diatomic molecules, the total energy E_{tot} can be divided into the energy of the electrons E_e, the rotational energy of the molecule E_r and the vibrational energy E_v. According to the Born-Oppenheimer-Approximation, these energies can be treated independently and summed up to

$$E_{tot} = E_e + E_r + E_v \tag{2.7}$$

The electronic transitions mainly correspond to radiation in the visible range (wavelength $\lambda = 690\,\text{nm}$ to $\lambda = 380\,\text{nm}$) of the electromagnetic spectrum. They are not further considered here since this thesis focuses on the infrared (IR) spectrum. Rotational and vibrational energy states are mostly in the IR range ($\lambda = 1\,\text{nm}$ to $\lambda = 690\,\text{nm}$) and most important for GHGs.

The vibrational states can be approximated by an harmonic oscillator with the following solution to the Schrödinger equation:

$$E_v = \hbar\omega \left(\nu + \frac{1}{2}\right) \tag{2.8}$$

with the reduced Planck constant $\hbar$, the vibrational frequency $\omega = \sqrt{k/\mu}$ defined by the force constant k and the reduced mass $\mu = \frac{m_1 m_2}{m_1+m_2}$, and the quantum number $\nu = 1, 2, 3, \ldots$. Consequently, the difference between two vibrational states is given by $\triangle E = \hbar\omega$. This energy can be directly translated into wavenumbers via $\tilde{\nu} = E/(hc)$. Hence, the resulting spectrum has only single absorption lines at $\triangle E$ since the selection rules for the harmonic oscillator are $\triangle\nu = \pm 1$. This approximation only holds for the low energy states. States of higher energy are often described by an empirical approximation in form of the so-called Morse-potential. It takes the possible dissociation of a molecule into account and adds a second part to the mathematical description of the vibrational energies originating in the inharmonicity of the potential as seen in equation 2.9.

$$E_v = \hbar\omega \left(\nu + \frac{1}{2}\right) \left[1 - \frac{\hbar\omega}{4D_e}\left(\nu + \frac{1}{2}\right)\right] \tag{2.9}$$

where D_e is the dissociation energy. The energy levels are no longer equidistant and the selection rules are extended to be $\triangle\nu = \pm 1, \pm 2, \pm 3, \ldots$. As a result, the spectrum is represented by multiple lines converging for larger ν and decreasing in their intensity due to decreasing probability for $|\triangle\nu| > 1$.

The rotational states are in first approximation derived by a semi-classical approach assuming a constant distance r between the two atoms. The rotational energy for this rigid body is given by:

$$E_r = \frac{1}{2} I\omega^2 = \frac{\mathbf{L}^2}{2I} \tag{2.10}$$

with the moment of inertia I and the classical angular momentum $\mathbf{L} = I\omega$. Considering the specific moment of inertia $I = \mu r^2$ for the reduced mass $\mu = \frac{m_1 m_2}{m_1+m_2}$ and the quantum mechanical angular momentum $|\mathbf{L}|^2 = \hbar^2 J(J+1)$ gives the energy levels:

$$E_r = \frac{\hbar^2}{2\mu r} \cdot J(J+1) \tag{2.11}$$

with the quantum number $J = 0, 1, 2, ...$ following the selection rule $\triangle J = \pm 1$. The energy difference between two states is given by

$$\triangle E_r = \frac{\hbar^2}{\mu r} \cdot (J+1) \tag{2.12}$$

This means that the rotational spectrum is represented by equidistant lines. However, this is not observed in experiments since the approximation neglects the centrifugal force between the atoms leading to an increase of the intermolecular distance r. Including this fact into the derivation (Demtröder 2018) and taking the selection rule $\triangle J = \pm 1$ into account leads to energy level differences as:

$$\triangle E_r = \frac{\hbar^2}{\mu r^2} \cdot (J+1) - \frac{2\hbar^4}{\mu^2 k r^6} \cdot (J+1)^3 \tag{2.13}$$

Here, k is a constant introduced by the restoring force counteracting the centrifugal force.

In experiments a combination of the rotational and vibrational spectrum, known as rovibrational spectrum, is observed. A typical energy scheme is shown in Figure 2.1. The energy gap between vibrational states is notably larger than that between rotational states. The rotational levels denoted by a single prime J' are associated with the vibrational state $\nu' = 1$, while those with a double prime J'' correspond to the vibrational state $\nu'' = 0$. The transitions with $\triangle\nu = +1$ and $\triangle J = -1$, which generate the lines of the P-branch, are depicted in blue. Conversely, the transitions with $\triangle\nu = +1$ and $\triangle J = +1$, resulting in the R-branch lines, are shown in red. The transitions with $\triangle\nu = +1$ and $\triangle J = 0$, drawn in dashed green, are permissible only for molecules where the angular momentum aligns with the symmetry axis.

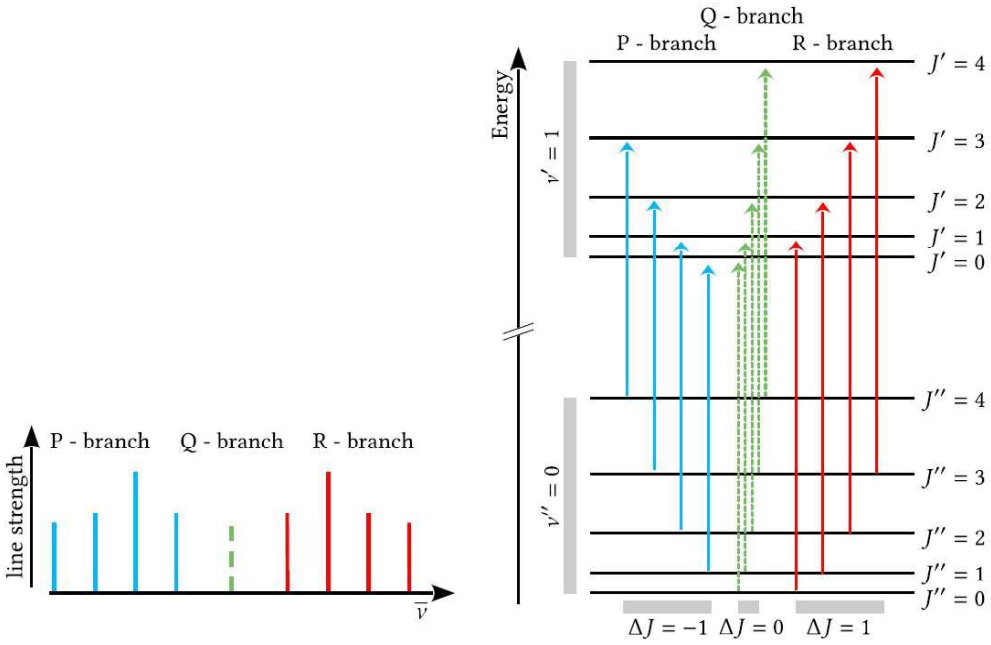

Figure 2.1: A schematic drawing of a rovibrational spectrum in the left panel and the corresponding level scheme in the right panel (Benedikt Herkommer 2024).

This description can be further improved by considering the coupling between the vibrational and rotational energy states. It becomes even more complex for polyatomic molecules for which a general formulation of the energy levels cannot be given. Further quantum numbers have to be introduced to describe the different vibrational modes resulting from the increased number of degrees of freedom. For more details see Demtröder 2018; Wolf et al. 2006.

Spectral lines in atmospheric remote sensing are not purely monochromatic as shown before but exhibit various broadening effects. Three key contributors to line broadening are natural line shape, Doppler broadening, and pressure broadening.

The **natural line shape** results from the finite lifetime of excited states. The energy-time uncertainty relationship of quantum mechanics leads to an uncertainty in the energy differences, causing a Lorentzian line shape. However, in atmospheric studies, the natural line shape is often negligible compared to other broadening effects, typically having a full width at half maximum (FWHM) around $8 * 10^{-8}\,\mathrm{cm}^{-1}$.

Doppler broadening arises from the thermal motion of molecules. Molecules moving at different velocities cause shifts in the observed wavenumber, broadening the absorption lines. This broadening results in a Gaussian distribution of line shape. The line width $\tilde{\nu_D}$ defined as FWHM is given by:

$$\tilde{\nu_D} = \tilde{\nu_0}\sqrt{\frac{8k_B T ln(2)}{mc^2}} \tag{2.14}$$

Here, c is the speed of light, k_B is the Boltzmann constant, T is the temperature of molecules with total mass m modulating the wavenumber of a molecule at rest $\tilde{\nu_0}$.

Pressure broadening occurs due to molecular collisions that shorten the excited states' lifetime, leading to a Lorentzian profile. The width parameter γ can be estimated by the mean collision time τ, which depends on temperature T and pressure p:

$$\gamma = \frac{1}{2\pi c\tau} = \frac{1}{2\pi c}\sqrt{\frac{p}{T}} \tag{2.15}$$

Under atmospheric conditions, where both Doppler and pressure broadening are significant, the Voigt-profile combines these effects. It is computed by convolving the Lorentzian and Gaussian profiles but requires numerical methods for efficient solutions (see e.g. Liu et al. 2001).

This section has shown that the electromagnetic spectrum contains a wealth of information. On the one hand, the line spacing depends on the energy levels, which in turn depend on molecular properties such as molecular mass and intermolecular distance; a unique signature for a molecule. On the other hand, the line shape contains information about the environment of the molecule, namely temperature and pressure. To retrieve this information, the spectrum must first be measured. A commonly used technique is Fourier Transform Infrared Spectroscopy, which will be explained in the next section.

2.3 Fourier Transform Infrared Spectroscopy

FTIR spectroscopy is used for the qualitative and quantitative analysis of substances. The following description is based on Griffith et al. 2007. The measurement principle is based on a two-beam interferometer originally designed by Michelson in 1891 and shown in figure 2.2.

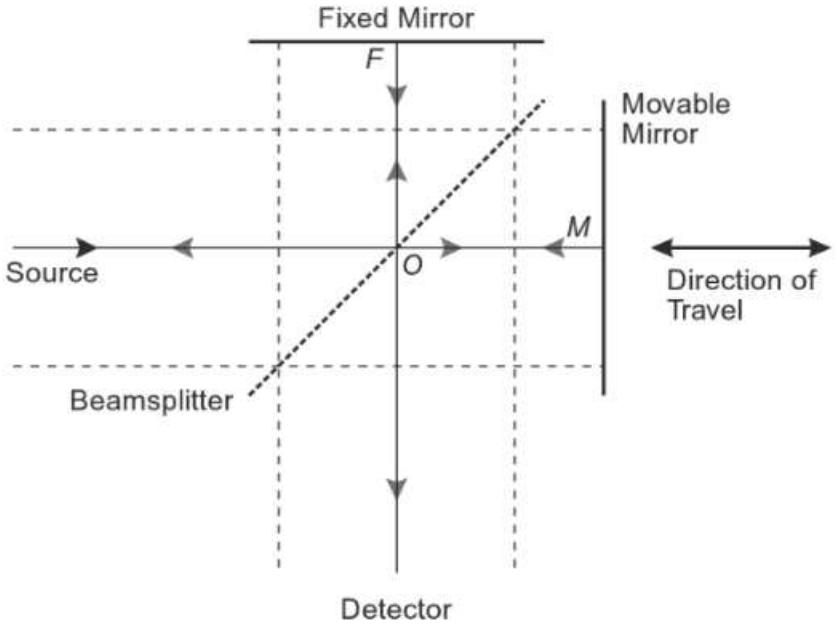

Figure 2.2: Schematic structure of a Michelson interferometer (Griffith et al. 2007).

A polychromatic light source's beam is split using a beamsplitter, creating two different light paths. The reflected light hits a mirror with a fixed position. The transmitted light reaches a movable mirror. After reflection on the mirrors, both light paths hit the beamsplitter again, where they recombine. A portion of the light is directed back to the light source, while the other portion is directed towards a detector. By changing the distance between beamsplitter and the movable mirror, a path difference between the two light paths is created. This can result in interference phenomena in the recombined light beam, leading to changes in intensity. The produced interferogram represents the detected light intensity as a function of the OPD. This time-domain signal can be converted into a frequency-domain signal, the spectrum, by a mathematical tool called Fourier transformation.

Considering a monochromatic light source with wavelength λ_0 and corresponding wavenumber $\tilde{\nu_0} = \frac{1}{\lambda_0}$, constructive interference and therefore an intensity maximum is registered each time that the optical path difference δ is an multiple of λ_0. If the mirror is moved at a constant velocity, the signal at the detector varies sinusoidally and the interferogram $I(\delta)$ is given by:

$$I(\delta) = \frac{1}{2} I(\tilde{\nu_0}) \cdot (1 + cos(2\pi\tilde{\nu_0}\delta)) \tag{2.16}$$

where $I(\tilde{\nu_0})$ is the intensity of the source at wavenumber $\tilde{\nu_0}$. For a polychromatic

source emitting multiple wavelengths, the total interferogram $S(\delta)$ is the superposition of all individual cosine waves:

$$S(\delta) = \int_0^\infty B(\tilde{\nu}) \cos(2\pi\tilde{\nu}\delta) d\tilde{\nu} \tag{2.17}$$

where $B(\tilde{\nu})$ is the spectral intensity as a function of wavenumber $\tilde{\nu}$. This integral is a cosine Fourier Transform. To retrieve the spectrum $B(\tilde{\nu})$ from the measured interferogram $S(\delta)$, the inverse Fourier Transform is applied:

$$B(\tilde{\nu}) = \int_{-\infty}^\infty S(\delta) \cos(2\pi\tilde{\nu}\delta) d\delta \tag{2.18}$$

Since $S(\delta)$ is an even function (symmetric around $\delta = 0$), this integral can be simplified to:

$$B(\tilde{\nu}) = 2\int_0^\infty S(\delta) \cos(2\pi\tilde{\nu}\delta) d\delta \tag{2.19}$$

In practice, interferograms are not continous but sampled at discrete intervals, and the Fourier Transform is computed numerically using the Fast Fourier Transform (FFT) algorithm. To prevent spectral artifacts, the interferogram must be sampled at a sufficiently high rate to avoid that large frequencies are folded back to the sampled range, known as aliasing. The minimum sampling rate δx for the correct reproduction of signals with frequencies smaller than $\tilde{\nu_N}$ is given by the Nyquist criterion:

$$\tilde{\nu_N} = \frac{1}{2\delta x} \tag{2.20}$$

In fact, obtaining accurate spectra from interferograms involves addressing several other real-world factors that lead to deviation from the ideal sinusoidal interferogram. One such factor is the **finite resolution** of the interferometer, determined by the maximum OPD, $\delta_{\max}$. The finite truncation of the interferogram with a "boxcar" function results in a spectrum convolved with a sinc function, limiting the resolution to $\Delta\tilde{\nu} = \frac{1}{\delta_{\max}}$. This causes broadening and distortion of spectral lines, which must be mitigated by techniques like apodization. Apodization applies a weighting function to reduce sidelobes of the sinc function, balancing resolution and spectral accuracy.

Phase errors present another significant deviation from ideal conditions. In theory, the phase of the interferogram should be zero; however, in practice, variations in the phase angle, $\theta_{\tilde{\nu}}$, occur due to optical and electronic imperfections. This necessitates phase correction to avoid distorted spectral lines. **Beam divergence** is also a concern, as a perfectly collimated beam is assumed in theoretical models, but real beams diverge, causing overlapping fringe patterns and reduced resolution. The Jacquinot stop is implemented to limit this divergence and retain spectral fidelity.

Furthermore, real-world spectrometers must account for instrumental factors such as **non-ideal detector response** and **beamsplitter efficiency**. These factors modify the interferogram's amplitude, described by a correction factor, $H(\tilde{\nu})$, dependent on the wavenumber. Thus, while theoretical models assume ideal conditions

for Fourier Transform spectrometry, real-world applications require careful consideration of these effects to ensure accurate spectral data. For more details see Griffith et al. 2007.

In FTIR spectroscopy, a broadband radiation source is employed, with the light beam hitting the Michelson interferometer being transmitted through the gaseous sample. The solar absorption FTIR spectrometer utilised in this thesis uses the Sun as the radiation source and the sample corresponds to the atmospheric column transected by the light beam reaching the detector. A variety of atmospheric gases, including CO_2, CO, N_2O, CH_4 and H_2O, absorb radiation within both the MIR spectral range, spanning from approximately 400 to 4 000 cm^{-1}, and the NIR wavelength range, extending from approximately 4000 to 12 500 cm^{-1}. The selection of the spectral range depends on the intended application. While many FTIR in-situ spectrometers utilise MIR due to the variety of absorbing gas species, atmospheric investigations, such as the EM27/SUN, employ the NIR for several reasons. One factor is the aforementioned variety of gas species in the MIR, which results in overlapping of the absorption bands and thus presents a challenge for spectrum analysis. The main gases of interest in atmospheric spectroscopy absorb also in the "less crowded" NIR. This approach enables the use of entire spectral absorption bands for retrieval, which also results in the reduction of temperature dependence. Lastly, a strong NIR absorption band is employed for the retrieval of oxygen (O_2), which is continually used as a quality measure and for the calculation of molar fractions. The retrieval of another gas species in the same spectral window results in the elimination of systematic errors, identical for both gases, thereby facilitating the calculation of the mole fraction. Figure 2.3 illustrates an example of a NIR spectrum with typical absorption lines for atmospheric gases considered in this thesis. This demonstrates that the absorption band for the gas retrieval must be selected with due consideration of the potential for overlap with other species, particularly the strong H_2O absorptions.

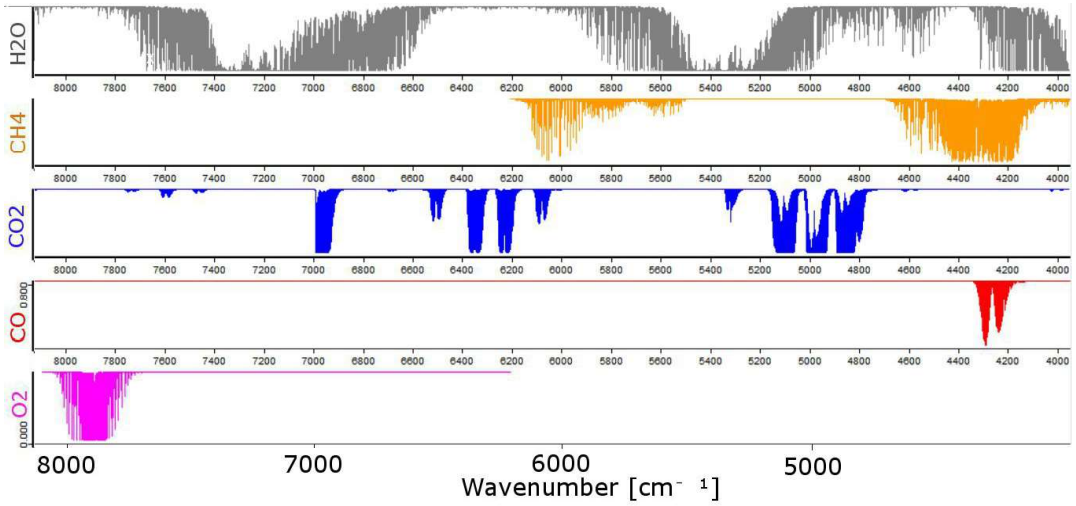

Figure 2.3: Near-infrared spectrum with typical absorption features for H_2O (grey), CH_4 (orange), CO_2 (blue), CO (red) and O_2 (pink).

In order to retrieve information about quantities that cannot be measured directly, such as the atmospheric properties of interest, the methodology of inversion theory is applied. The analysis demands a so-called forward model simulating the absorption in the atmosphere and the characteristics of the measuring instrument. The gas concentrations are obtained by iteratively minimizing the difference between the model predictions and the measured spectrum (Rodgers 2000).

The formula setting the base for the atmospheric model is called radiative transfer equation (RTE) and describes the transport of electromagnetic radiation through the atmosphere. Thereby, the radiation travels a distance dz changing its radiant flux L as (Burrows et al. 2011)

$$\begin{aligned} dL(z,\tilde{\nu},T) = &- \left[\epsilon_a(z,\tilde{\nu},T) + \epsilon_s(z,\tilde{\nu},T)\right] \cdot L(z,\tilde{\nu},T)\, dz \\ &+ \epsilon_a(z,\tilde{\nu},T) \cdot B(\tilde{\nu},T) \\ &+ \epsilon_s(z,\tilde{\nu},T) \int_0^{2\pi} \int_0^{\pi} L(z,\tilde{\nu},\theta,\phi) \cdot \frac{S(\theta,\phi)}{4\pi} d\phi\, \sin(\theta)\, d\theta \end{aligned} \tag{2.21}$$

The first line of equation 2.21 describes the losses of radiation. They consist of absorption and scattering of radiation quantified by the absorption coefficient ϵ_a and scattering coefficient ϵ_s, respectively. A flux increase results from thermal emissions of atmospheric gases described by the Planck function $B(\tilde{\nu},T)$ in the second line of the equation. The last line contributes to a flux increase by scattering of radiation into the line of sight described by a function S including the directional characteristics of the scattering.

The general RTE cannot be solved analytically. Simplifications are necessary to approximate the solution. For solar absorption measurements in the IR region two terms can be neglected. Scattering becomes minimal because of the large wavelengths in the IR range and the λ^{-4} dependence of the Rayleigh scattering describing the scattering on atmospheric molecules. Additionally, thermal emission can be neglected due to the large temperature difference between the temperatures of the atmosphere and the significantly higher temperature of the Sun (Burrows et al. 2011). This simplifies the RTE to

$$dL(z,\tilde{\nu},T) = -\epsilon_a(z,\tilde{\nu}) \cdot L(z,\tilde{\nu},T)\, dz \tag{2.22}$$

which can be solved to

$$L(s_1,\tilde{\nu},T) = L(s_0,\tilde{\nu},T) \cdot exp\left(-\int_{s_0}^{s_1} \epsilon_a(s,\tilde{\nu},T)\, ds\right) = L(s_0,\tilde{\nu},T) \cdot exp\left(-\tau(s_0,s_1,\tilde{\nu},T)\right) \tag{2.23}$$

Equation 2.23 is known as the Lambert-Beer equation describing the exponential attenuation of the radiant flux L travelling through a medium with optical depth τ between the two points s_0 and s_1. This model can be used to quantify the number of molecules of the different atmospheric gases for known atmospheric conditions. The individual absorption coefficients can be obtained through the line-by-line parameters given in the High-resolution Transmission Molecular Absorption Database (HITRAN) (Gordon et al. 2022).

In reality, the forward model $F(\mathbf{x})$ has to consider many more atmospheric variables as in the simple example above, as well as instrumental properties. The main concept is discussed here and is based on Rodgers 2000. The forward model calculates the spectrum - to the best of our understanding of the underlying physics - based on a given state vector $\mathbf{x}$, which represents the sample's physical properties (for example, concentrations or temperature). In order to account for the deviation of the model from the real physics of the true measurement $\mathbf{y}$, described by a function $f(\mathbf{x})$, the error term ϵ is introduced:

$$\mathbf{y} = f(\mathbf{x}) = F(\mathbf{x}) + \epsilon(\mathbf{x}) \tag{2.24}$$

The quantity of interest is the retrieval $\hat{\mathbf{x}}$, including for example the number of molecules, calculated from the measured spectrum $\mathbf{y}$. $\hat{\mathbf{x}}$ is to be understood as an estimate rather than a true state. It is the result of applying some inverse or retrieval method $\mathbf{R}$ on the measurement. Inverse problems in FTIR spectroscopy are typically ill-posed because they are underdetermined (fewer independent measurements than unknowns) and highly sensitive to noise. At the same time they provide an infinite number of possible solution. In order to find an appropriate estimate for the retrieval, an a priori estimate $\mathbf{x_a}$ of $\mathbf{x}$ is used. The retrieval method is a function of the a priori state and the forward model.

$$\hat{\mathbf{x}} = \mathbf{R}(\mathbf{y}, \mathbf{x_a}, \mathbf{c}) = \mathbf{R}\left[F(\mathbf{x}) + \epsilon, \mathbf{x_a}, \mathbf{c}\right] \tag{2.25}$$

where $\mathbf{c}$ are retrieval parameters that are not included in the forward model. In order to specify the retrieval method, the forward model is first linearised around the a priori, i. e. at $\mathbf{x} = \mathbf{x_a}$, such that

$$\hat{\mathbf{x}} = \mathbf{R}\left[F(\mathbf{x_a}) + \mathbf{K}(\mathbf{x} - \mathbf{x_a}) + \epsilon, \mathbf{x_a}, \mathbf{c}\right] \tag{2.26}$$

where $\mathbf{K}$ is a Jacobian matrix, known as the weighting function matrix. It represents the sensitivity of the spectrum calculated by the forward model $\mathbf{F}$ to changes in the true state $\mathbf{x}$. Next, the retrieval $\mathbf{R}$ is linearised around $\mathbf{y}_0$ such that $\mathbf{R}(\mathbf{y}_0) = \mathbf{x_a}$:

$$\hat{\mathbf{x}} = \mathbf{R}\left[F(\mathbf{x_a}), \mathbf{x_a}, \mathbf{c})\right] + \mathbf{G}\left[\mathbf{K}(\mathbf{x} - \mathbf{x_a}) + \epsilon\right] \tag{2.27}$$

where $\mathbf{G}$ is the gain matrix representing the sensitivity of the retrieval method $\mathbf{R}$ to changes in the measured spectral data $\mathbf{y}$. It essentially determines how much the retrieval should "adjust" the a priori state $\mathbf{x}_a$ based on the difference between the actual measurement $\mathbf{y}$ and the predicted measurement from the forward model.

The difference between the retrieved state $\hat{\mathbf{x}}$ and the a priori state $\mathbf{x_a}$ is then given by

$$\begin{aligned} \hat{\mathbf{x}} = \mathbf{R}\left[F(\mathbf{x_a}), \mathbf{x_a}, \mathbf{c})\right] - \mathbf{x_a} \\ + \mathbf{GK}(\mathbf{x} - \mathbf{x_a}) \\ + \mathbf{G}\left[\epsilon\right] \end{aligned} \tag{2.28}$$

Note that the first term should be zero as the linearisation point was chosen such that $\mathbf{R}\left[F(\mathbf{x_a})\right] = \mathbf{x_a}$.

Equation 2.28 can be simplified by introducing the averaging kernel A, which is given by

$$\mathbf{A} = \mathbf{G} \cdot \mathbf{K} = \left.\frac{\partial \mathbf{R}}{\partial \mathbf{y}}\right|_{\mathbf{y}=\mathbf{y_0}} \cdot \left.\frac{\partial \mathbf{F}}{\partial \mathbf{x}}\right|_{\mathbf{x}=\mathbf{x_a}} = \left.\frac{\partial \hat{\mathbf{x}}}{\partial \mathbf{x}}\right|_{\mathbf{x}=\mathbf{x_a}} \tag{2.29}$$

Combining equation 2.29 and 2.28 yields

$$\hat{\mathbf{x}} = \mathbf{x}_a + \mathbf{A}\left(\mathbf{x} - \mathbf{x}_a\right) + \mathbf{G}\epsilon \tag{2.30}$$

The averaging kernel $\mathbf{A}$ is a matrix that provides insight into the resolution of the retrieval and how much the retrieved state is smoothed relative to the true state. It indicates the sensitivity of the retrieval to changes in the measured column, making it essential for understanding the quality of an inverse model in FTIR spectroscopy and comparing different retrieval methods and instruments.

The FTIR spectrometer used in this thesis measures the total column instead of retrieving a vertical profile. Therefore, the averaging kernel is a vector function of altitude, dependent on ground pressure and solar zenith angle (SZA). It specifies the extent to which an excess partial column superimposed on the actual profile at a given input altitude is reflected in the retrieved total column amount (K. IMK-ASF 2023). The shape and values of the column sensitivities can be found in K. IMK-ASF 2023 and Hedelius et al. 2016.

2.4 EM27/SUN Spectrometer

The EM27/SUN spectrometer is a portable, low-resolution FTIR spectrometer designed for the precise and accurate measurement of column-averaged greenhouse gas abundances of CO_2, CH_4, and CO. This spectrometer operates with a RockSolid™ pendulum interferometer, comprising two cube corner mirrors and a calcium fluoride (CaF_2) beamsplitter, which offers high stability with respect to thermal and mechanical disturbances, crucial for field operations. The instrument employs a HeNe laser and an InGaAs detector. It achieves an OPD of 1.8 cm, corresponding to a spectral resolution of 0.5 cm^{-1} (Gisi et al. 2012).

The main channel of the EM27/SUN spectrometer covers a spectral range from 5 500 to 11 000 cm^{-1}. This range has been designed in order to avoid any compromise in measurement accuracy for the primary target gases (Hase et al. 2016). For the retrieval of individual species, the spectrometer uses specific spectral windows to maximize the accuracy of each gas's column retrieval. The retrieval of CO_2 and CH_4 columns is conducted in the spectral windows of 6173–6390 cm^{-1} and 5897-6145 cm^{-1} (Luther et al. 2019), respectively. The analysis of O_2 is performed over the range of 7765–8005 cm^{-1} (Hase et al. 2016).

Additionally, the EM27/SUN has been modified to include a second detector channel covering the 4000–5500 cm^{-1} spectral range, thereby enabling the measurement of CO in the spectral window of 4210–4320 cm^{-1}. The four spectral windows can be seen in Figure 2.3. The system employs a dual-channel configuration, utilising a small plane mirror to partially decouple the beam towards the secondary detector. This enables simultaneous observations without affecting the functionality of the primary detector channel (Hase et al. 2016).

The EM27/SUN routinely records double-sided interferograms. These are acquired in DC-coupled mode, thus allowing for the correction of variable atmospheric transmission due to the effects of aerosol and cloud cover in a manner similar to that described by Keppel-Aleks et al. 2007. The Fourier transformation is applied by using the Norton-Beer medium apodization function (Davis et al. 2010) to reduce sidelobes around the spectral lines (Frey et al. 2019).

In conclusion, the EM27/SUN spectrometer, with its dual-channel configuration and defined spectral windows for different gas retrievals, serves as a reliable tool for atmospheric research and satellite validation efforts (Hase et al. 2016). The compact design with a total weight of 30 kg and low power consumption of approximately 50 W, permits mobile operation during field campaigns, which can be conducted by a single person (see Figure 2.4). For the purposes of this thesis, the instrument with the serial number 82 (SN82) has been utilised.

The EM27/SUN spectrometer has been demonstrated to be highly reliable in a number of employments (B. Herkommer et al. 2024): In their studies, Frey et al. 2019 and Alberti et al. 2022 have demonstrated the long-term and collective stability of the EM27/SUN through the use of the instrumental line shape (ILS) of each spectrometer and comparisons of XGas values. The spectrometer has demon-

strated considerable flexibility, enabling its deployment in numerous urban measurement campaigns across the globe over the past decade (Tu et al. 2022b; Alberti et al. 2022; Hase et al. 2015). In addition to city campaigns, permanent monitoring stations are now being established in major cities (Dietrich et al. 2021), where multiple EM27/SUN spectrometers are deployed throughout the city to measure GHG emissions. Furthermore, the successful installation of the instrument on mobile platforms, including ships and trucks, has been demonstrated in several studies (Klappenbach et al. 2015; Butz et al. 2017; Luther et al. 2019; Knapp et al. 2021; Butz et al. 2022).

Figure 2.4: The EM27/SUN spectrometer.

2.5 PROFFAST

In this section, the retrieval software PROFFAST and the PROFFASTpylot are described based on B. Herkommer et al. 2024 and IMK-ASF 2023. The structure is illustrated in Figure 2.5. The PROFFAST software comprises of three discrete programs: 'preprocess', 'pcxs', and 'invers'. The 'preprocess' program is responsible for the conversion of interferograms into spectra. The atmospheric simulation, which constitutes a component of the forward model, is generated by the 'pcxs' program. The final step performed by the 'invers' program is the retrieval process. In order to assure a successful run, the software requires the following input files: the recorded ground pressure, the recorded interferograms and the a priori profiles, which are, by default, given as '.map'-files obtained from the Caltech server. The Python interface PROFFASTpylot provides comprehensive management of the PROFFAST software, overseeing all input files and subsequently executing the three processing programs.

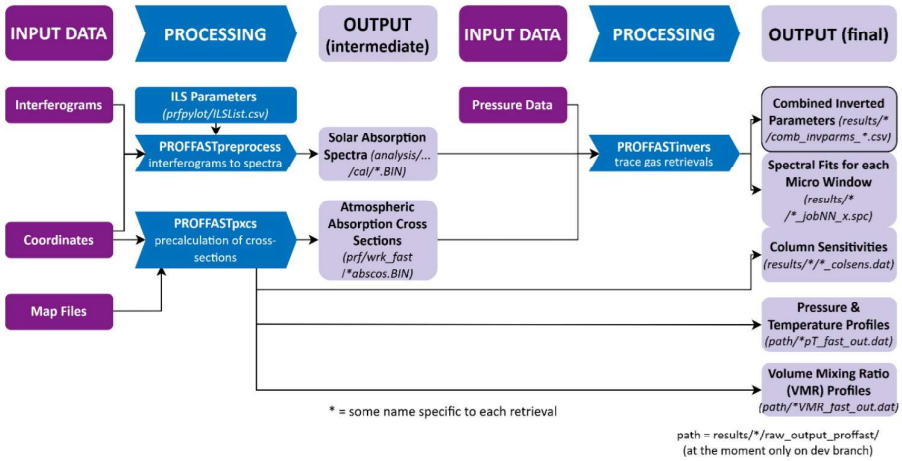

Figure 2.5: Schematic of the trace gas analysis within PROFFAST. The PROFFASTpylot coordinates the subsequent execution of the individual processing steps (blue) and the implementation of the input files (purple) (IMK-ASF 2023).

The process yields the total number of molecules of the specified gases present in the measured air column, represented as TC_{Gas}. The desired result, denoted as $XGas$, is the fraction of the number of molecules of a certain gas relative to the total number of molecules, averaged over the entire column. As the total column of dry air is not measurable, the known column-averaged dry-air mole fraction of O_2 is employed instead:

$$XO_2 = \frac{TC_{O_2}}{TC_{dry-air}} \approx 0.2095. \tag{2.31}$$

Therefore, the column-averaged dry-air mole fraction of the desired gas is given by the following equation:

$$XGas = \frac{TC_{Gas}}{TC_{O_2}} \cdot 0.2095. \tag{2.32}$$

This formula has the advantage of mitigating systematic errors occurring in TC_{O_2} and TC_{Gas} to a significant extent, thereby facilitating the experimental calculation (B. Herkommer et al. 2024).

2.6 Lagrangian Modelling and FLEXPART

Lagrangian modelling is a method used to describe and simulate dynamic atmospheric processes, including the emission and transport of an air mass, as well as the deposition of disposed particles. The fundamental premise is that the observer and its coordinate system are in motion with the air parcel under study, tracking its progression. The air parcel is characterised by a set of parameters, including density, temperature, humidity, and pollutant concentration (either aerosols or trace gases), and is treated as a point mass with four-dimensional coordinates. The movement of the air parcel is influenced by the surrounding meteorological conditions, including wind patterns, precipitation, fundamental chemical processes such as radioactive decay, and stochastic turbulence effects (Seibert et al. 2004).

In general, Lagrangian models simulate the behaviour of thousands of particles in three dimensions, dispersing in a variety of directions. While interactions between particles are typically excluded from the model, independent processes such as wet and dry deposition and radioactive decay are accounted for. The model's principal strength lies in its capacity to trace the trajectory of air masses both forward and backward, thereby establishing a link between their current state and their historical path (Seibert et al. 2004).

One specific implementation of Lagrangian modelling is the FLEXible PARTicle dispersion model (FLEXPART) software (Stohl et al. 2002), which is an open-source Lagrangian Particle Dispersion Mode (LPDM) released under the GNU General Public License (GPL) (Lin et al. 2012). FLEXPART employs forward and backward modelling to simulate a comprehensive range of atmospheric processes. In forward modelling, the dispersion of particles from an emitting source is simulated, and the resulting concentrations, wet deposition, and dry deposition across a selected grid and altitude are provided as output (Stohl et al. 2023).

In contrast, backward modelling involves tracing a measured concentration back to its source. Furthermore, FLEXPART generates four-dimensional fields (time, altitude, latitude, longitude) that illustrate the sensitivity of a measurement to specific grid cells in the atmosphere. These sensitivities reflect the residence time of air parcels in a grid cell, indicating the extent to which particles from that cell exert influence on the measured concentration. The dual capability of FLEXPART permits comprehensive analysis of atmospheric particle dispersion in both directions (Poulidis 2021).

2.7 Differential Optical Absorption Spectroscopy

The technique of DOAS is a powerful spectroscopic tool for measuring atmospheric trace gases and aerosols by analysing the absorption of light in the UV, visible (VIS), and NIR regions. In contrast to traditional absorption spectroscopy, which often deals with broad and overlapping absorption features, DOAS focuses on narrow-band absorption structures by differentiating them from the broad-band absorptions caused by other atmospheric components as well as Mie and Rayleigh scattering. The methodology is described in the following based on Platt et al. 2008.

The amount of the absorbing gas species is determined based on the RTE as described in equation 2.21. From this, the Lambert-Beer law is derived, but taking also into account scattering, which cannot be neglected in the UV-VIS range. The optical depth τ can be described in terms of the absorption cross-section σ_i of species i at wavelength λ, with the present density of the species ρ_i. The optical depth can be decomposed into contributions from absorption and Mie and Rayleigh scattering, which yields:

$$L(\lambda) = L_0(\lambda) \cdot \exp\left(- \int_{s_0}^{s_1} \left[\sum_i \sigma_i(\lambda, s)\rho_i(s) + \sigma_{Mie}(\lambda, s)\rho_{Mie}(s) + \sigma_{Ray}(\lambda, s)\rho_{Ray}(s) \right] ds \right) \tag{2.33}$$

for the radiant flux $L(\lambda)$ at wavelength λ after passing through the medium with the initial flux $L_0(\lambda)$. This approach allows the absorption spectrum to be divided into two components: a differential component comprising narrow-band absorption structures and a broad-band component incorporating scattering and spectrally broad absorption effects. This decomposition allows for the isolation of narrow absorption features specific to trace gases, thereby enhancing selectivity and sensitivity. As the broad-band features vary smoothly with wavelength, they can be approximated by a low-order polynomial $P(\lambda)$. Moreover, it can be assumed that the absorption cross-sections remain constant along the light path. This enables the path integral over the density to be solved, thereby yielding the slant columns (SC), which represent the integrated absorber amount along the light path. Including these elements into the equation 2.33 and taking the natural logarithm thereof yields:

$$\ln\left(\frac{L(\lambda)}{L_0(\lambda)}\right) = - \sum_i \sigma_i(\lambda) SC_i + P(\lambda) \tag{2.34}$$

In a simplified case, where only one absorber is considered, the polynomial can be subtracted to yield an equation for the differential optical depth τ of the form

$$\Delta\tau(\lambda) = \ln\left(\frac{L(\lambda)}{L_0(\lambda)}\right) = -\sigma(\lambda) SC \tag{2.35}$$

The slant column can then be obtained by a straightforward scaling of the absorption coefficients to the derived differential optical depth.

A key advantage of DOAS is its capacity to conduct measurements in real-world conditions, where overlapping absorptions and variable light paths present significant challenges. By focusing on differential absorption features, DOAS reduces the errors associated with scattering, which often introduces uncertainties in absolute concentration measurements in traditional absorption techniques. Furthermore, the DOAS method can be employed over a wide range of path lengths, from a few metres in laboratory settings to several kilometres in field applications. This allows for both remote sensing and in-situ analysis. Moreover, the brief duration of a single measurement renders it suitable for deployment on moving vehicles, including bicycles and cars. The versatility of DOAS makes it an ideal tool for atmospheric monitoring, where it is employed to detect trace gases such as nitrogen dioxide (NO_2), sulfur dioxide (SO_2), ozone (O_3), formaldehyde (HCHO), and several volatile organic compounds (VOCs). However, it is important to note that DOAS measurements provide an estimate of the total column load of the gas species under study, and do not offer insights into the vertical distributions.

2.8 Investigated Steel Production

The steel industry is responsible for approximately 7 % of the global anthropogenic CO_2 emissions (Agency 2020), and it is anticipated that production will increase in order to meet the demands of a growing global population. The highly CO_2-intensive blast furnace-basic oxygen furnace production route is thereby the predominant steelmaking process accounting for 70 % of steel production worldwide. The Linz-Donawitz process is employed, whereby iron ore serves as the primary raw material and coke functions as the reducing agent. A by-product of the process are substantial quantities of CO-rich gases (Ishioka et al. 1992; Kim et al. 2016).

Monitoring the greenhouse gas emissions of such large emitters on the scale of individual steel plants represents a significant challenge. While satellite measurements are limited in spatial resolution for accurate CO_2 estimates, ground-based techniques lack both spatial and temporal coverage. However, it is crucial to obtain an accurate understanding of the GHG emissions and the underlying processes in order to effectively address the rapid decarbonisation in this important industrial sector.

The environmental impact of steel production sites has been analysed in several studies employing a bottom-up approach, mainly focusing on CO_2 (Suer et al. 2022, and references therein). A detailed inventory for a steel production site was created by Burchart-Korol 2013, comprising a single steel plant in Poland. Remote sensing measurements obtained from satellites can be used to obtain estimates of the CO emissions. A few studies have quantified the CO emission rates for urban areas and industrial parks without attributing them to a specific sector (Park et al. 2021; Tian et al. 2022). In a recent study, Wu et al. 2022 derived CO/CO_2 ratios for two Chinese cities with a strong industrial and energy focus, suggesting that CO could be used as a proxy for CO_2 emissions. An illustrative case study for investigating this idea are the steel production sites in Germany that still utilise the conventional blast furnace–basic oxygen furnace production route, situated in Duisburg, Dillingen/Saar, Salzgitter, Bremen, and Eisenhüttenstadt. For these facilities, CO_2 emission data is available from emission trading data of the European Union Emissions Trading

System (EU ETS). In conjunction with the large amounts of CO emissions, which can be obtained from data from the TROPOMI on board the Sentinel-5 Precursor satellite, a CO/CO_2 ratio can be determined (Schneising et al. 2024). The CO and CO_2 emissions show a linear correlation for all five steel plants with a CO/CO_2 emission ratio of 3.24 % (2.73 % - 3.89 %; 1 σ) for a mass fraction and 5.09 % (4.27 % - 6.11 %, 1σ) considering the number of molecules. This result supports the feasibility of utilising CO as a proxy for CO_2 emissions for comparable steel production sites.

It is challenging to make a direct comparison between the derived emission ratio for the German steel plants and those obtained for other steel plants around the world. The aforementioned studies and global inventories (Crippa et al. 2020) underestimate the CO/CO_2 ratio by including other sectors with significant CO_2 emissions but virtually zero CO emissions. Similarly, the verification of the measured CO and CO_2 emissions from the satellite is a challenging undertaking. The emission register provided by the Umweltbundesamt, accessible via the thru.de portal (Umweltbundesamt 2022), offers data on installation-based GHG emissions. However, these values are based on measurements, calculations, or estimates provided by operators, and are not subject to independent verification (Schneising et al. 2024).

This thesis investigates the potential for utilising of the portable EM27/SUN and the IFS 125HR spectrometer in verifying the CO/CO_2 emission ratio for the steel production site in Bremen. The study conducted by Schneising et al. 2024 yielded a mean CO emission of 92 $\pm$ 59 kt/yr. Together with estimated CO_2 emissions from the EU ETS of 2.3 Mt/yr that yields an emission ratio of about 6.29 ± 4.09 % considering the number of molecules. This is higher than the averaged value for all five German steel plants and the obtained CO emission estimate is slightly higher than that reported by the operator (71.9 kt/yr for 2022) (Umweltbundesamt 2022). The thru.de portal can be used to obtain a first impression of the expected order of magnitude of the emissions in the vicinity of the steel plant (for 2022). Its CO_2 emissions are estimated through calculations to be 2.16 Mt/yr. Other estimated emissions include SO_2 (3.5 kt/yr), NO_2 (1.7 kt/yr), particulate matter (342 t/yr), zinc compounds (468 kg/yr) and mercury compounds (15 kg/yr). The CO/CO_2 ratio calculated from these values gives 3.33%. Two power plants situated to the north of the steel plant are fuelled by blast furnace gas from the steel production and contribute additional 2.66 Mt/yr of CO_2, 330 t/yr of SO_2, 22.6 t/yr of NO_2, but virtually no CO. Including these emissions in the ratio calculation by the thru.de values gives a revised result of 1.49 %. The additional CO_2 of the power plants is not included in the ratio calculation by Schneising et al. 2024 as their objective is to determine the CO/CO_2 ratio of the steel plant. Although the power plants generate additional energy, their emissions result in the firing of furnace gas from the steel plant, which would otherwise be released into the atmosphere. The emission product of the steelmaking process is subjected to further processing, yet the emission can still be attributed to the entire complex of the steel production site. In order to estimate these total emissions of the steel production site in Bremen and use CO as a proxy, it is also necessary to determine the CO/CO_2 emission ratio of the entire facility. Therefore, this thesis distinguishes between the emission ratio of the steel plant and the emission ratio of the steel production site. The latter is measured as a ratio considering the number of molecules by employing the two spectrometers.

Chapter 3

Research Question

The main goal of this thesis is to investigate the potential contribution of ground-based remote sensing techniques in determining the total CO and CO_2 emissions, as well as the CO/CO_2 emission ratio of the steel production site in Bremen. The deployment of a portable EM27/SUN spectrometer in the vicinity of the steel plant will facilitate the investigation of its capacity to measure the spatially and temporally varying plume of the emission stack, thereby providing precise information on the emission ratio.

The on-site measurements will be complemented by data from the IFS 125HR spectrometer at the University of Bremen. The combination of the two datasets is only meaningful if the measurement bias between the instruments are significantly less than the observed emissions. It is therefore necessary to ascertain the comparability of the two spectrometers and to perform an instrument-to-instrument calibration.

Additionally, the advantages of DOAS measurement of NO_2 for localising the emission plume will be examined. Furthermore, atmospheric Lagrangian modelling is used to examine the plume behaviour and facilitate total emission estimation.

This thesis aims to combine the advantages of the different measuring techniques employed in order to derive a robust methodology for the quantification of the measured emissions. If this permits the determination of the specific CO/CO_2 emission ratio, CO can be used as a proxy for satellite-based measurement in order to determine the total CO_2 emissions of individual large steel plants of the same type. The combination with atmospheric models ideally allows for a direct quantification of the total emissions and verification of the satellite measurements.

Chapter 4

Measurements and Discussion

4.1 Intercalibration via Side-by-Side Measurements

All EM27/SUN and IFS 125HR spectrometers undergo rigorous calibration procedures, wherein their ILS is derived from water vapour lines through measurements employing a calibrated gas cell. However, instrumental imperfections persist, resulting in biases in the retrieved gas abundances measured by different spectrometers (Alberti et al. 2022). In order to facilitate a comparison between data obtained from the two different spectrometers, it is necessary to perform empirical adjustments. This is achieved by introducing an empirical instrument-to-instrument calibration factor, designated as a bias compensation factor (BCF) in this thesis.

The initial section of this chapter outlines the methodology employed to derive the BCFs. Furthermore, the methodology is applied in a comparative analysis of side-by-side measurements of the EM27/SUN SN82, which is the principle instrument utilized in the data presented in this thesis, alongside the IFS 125HR spectrometer in Bremen, which will be employed to furnish background data for on-site measurements at the steel plant.

4.1.1 Defining the Bias Compensation Factor

In order to facilitate the analysis of data from two distinct instruments, it is essential to ensure that both instruments have been calibrated against one another. This implies that they must provide identical gas abundances when measuring the same air column. It is therefore necessary to calculate the observed bias between the two instruments. This is achieved by utilising a method known as BCFs (Benedikt Herkommer 2024). In this approach, XGas_{ref} and XGas_{cal} represent the XGas measurements obtained from a reference instrument and an instrument which is going to be calibrated, respectively. The bias compensation factor K_{ref}^{cal} is employed to describe the instrument-to-instrument bias by

$$\mathrm{XGas}_{cal} = K_{ref}^{cal} \cdot \mathrm{XGas}_{ref} \tag{4.1}$$

Given the pivotal role of the BCF calculation in ensuring the accuracy of subsequent analytical outcomes, only high quality data were used for the calculation. This was achieved by filtering the recorded data in accordance with the following criteria, which are analogous to those proposed by B. Herkommer et al. 2024:

1. All data recorded at a SZA exceeding 75 ° are excluded from the comparative analysis. This is due to the fact that at larger SZA, there is a greater variation in the air mass. As the air mass increases, the impact of spectroscopic inaccuracies also increases, leading to an expansion of the measurement uncertainty.

2. Measurements with obvious outliers in XAIR are filtered out. It is an artificial quantity which is used to check for consistency in the retrieval process. It becomes unity for a perfectly working spectrometer. The used upper-lower limits are 0.998-1.002 for SN82 and 0.997-1.003 for 125HR. They are based on the average performance of the devices on a cloud-free day.

3. Finally, any remaining evident outliers for each species are also removed. The upper-lower limits employed in this process are 1.6–1.95 ppm for XCH_4, 350–450 ppm for XCO_2 and 40–200 ppb for XCO.

These filters were used for all data considered in the calculation of the BCFs in an identical way. The approach is adapted from B. Herkommer et al. 2024 and described next.

Initially, the filtered data is binned into time intervals of 10 minutes. The value of the mean of all XGas values recorded by the reference instrument within the time interval, denoted by $\overline{\mathrm{XGas}_{ref,i}}$, is calculated for each bin i. Similarly, the data for the second instrument is binned to $\overline{\mathrm{XGas}_{cal,i}}$. The BCF for a single bin is given by equation 4.1 with the index i and averaged values. Rather than merely averaging the $K^{cal}_{ref,i}$ values, the method is enhanced by incorporating a cost function to optimise the BCF (Frey et al. 2015).

The discrepancy between the reference value $\overline{\mathrm{XGas}_{ref,i}}$ and the adjusted value for the second instrument, given by $\overline{\mathrm{XGas}_{cal,i}}/K^{cal}_{ref}$, is calculated for each bin i. The squared sum of all these residuals weighted by their standard errors s_i constitutes the cost function given in equation 4.2.

$$\text{Costfunction} = \sum_i \left(\frac{\frac{\mathrm{XGas}_{cal,i}}{K^{cal}_{ref}} - \mathrm{XGas}_{ref,i}}{\sqrt{s^2_{cal,i} + s^2_{ref,i}}} \right)^2 \tag{4.2}$$

In order to identify the most precise BCF $K^{cal}_{ref,opt}$, the cost function is minimised in an iterative procedure. For measurements with 10 scans, each bin contains between five and seven unfiltered data points. To prevent bins with a limited number of values from exerting an undue influence on the statistical weight of individual measurements, only bins with a minimum of four values are considered.

4.1.2 Bias Compensation Factors for the EM27/SUN SN82

Daily BCFs have been calculated for the EM27/SUN SN82 towards the reference instrument IFS 125HR and are presented in Table 4.1. In order to achieve this, the IFS 125HR spectrometer was operated with the same parameters as the EM27/SUN, i. e. it recorded double-sided interferograms with a spectral resolution of $0.5\,\mathrm{cm}^{-1}$, averaging 10 scans to one measurement.

The estimation of the error associated with the BCF requires an approximation of the variance in the measurements of the single XGas values. In order to achieve this, a time interval exhibiting a linear change in gas abundance was extracted. The recorded data were detrended, and the standard deviation with respect to a mean value was determined. This value represents the error of a single measurement (see A.4). The error for the average bin value is then given by the standard error taking the values per bin into account. In order to estimate the error associated with the final BCF, as shown in table 4.1, the weighted standard deviation of all single-bin BCFs $K^{cal}_{ref,i}$ with respect to the optimal BCF $K^{cal}_{ref,opt}$ is calculated (see A.5).

Table 4.1: Calculated bias compensation factors for CO_2, CO and CH_4 for the EM27/SUN SN82 spectrometer with respect to the IFS 125HR spectrometer on different days and with different measurement duration (number of bins).

Date	**bins**	$\mathbf{K^{ref}_{SN82}}$ **for** $\mathbf{CO_2}$	$\mathbf{K^{ref}_{SN82}}$ **for CO**	$\mathbf{K^{ref}_{SN82}}$ **for** $\mathbf{CH_4}$
08.05.24	29	0.998547 ± 0.000254	1.027336 ± 0.007102	0.999082 ± 0.000426
10.05.24	45	0.998651 ± 0.000226	1.011029 ± 0.004371	0.999304 ± 0.00019
11.05.24	42	0.998949 ± 0.000392	1.00601 ± 0.002205	0.999644 ± 0.000334
13.05.24	11	0.999311 ± 0.000357	0.99473 ± 0.00532	1.00041 ± 0.000187
08.07.24	3	0.998596 ± 0.000184	1.02236 ± 0.000214	0.998685 ± 0.000181
06.08.24	8	0.999204 ± 0.000157	1.016121 ± 0.002137	0.999624 ± 0.000157

The BCF for XCO_2 varies between 0.998547 and 0.999311. Taking the weighted mean gives in an average BCF of 0.998803. The BCF for XCH_4 varies between 0.998685 and 1.00041 with a weighted mean of 0.998752. The variation in the compensation factor for XCO appears to be greater. The BCF varies between 0.999473 and 1.027336 with a weighted mean of 1.01217. This means that the EM27/SUN SN82 measures a higher XCO_2 and CH_4 abundance than the 125HR but a lower XCO abundance. Figure 4.1 illustrates that the BCF for XCO shows a higher variability than the BCF for XCO_2 and XCH_4. As simultaneous measurements of the EM27/SUN SN82 and the 125HR are used in this thesis, the recorded data from the SN82 are always calibrated against the 125HR, and therefore BCFs of 0.998801 and 1.011283 are used for XCO_2 and XCO, respectively (weighted means not taking the most recent side-by-side measurement after the field measurements into account).

Furthermore, a closer look at the plotted calibration data in Section A.2 makes clear, how well the BCF for XCO should be chosen. While taking the average BCF for XCO_2 leads to consistent results, a clear difference in taking the average BCF for XCO and taking the daily BCFs is seen (see Figures A.3). It varies in two days within the magnitude of a percent, corresponding to a difference in the abundance of about 1 ppb. Consequently, the data for Stations 1 and 2 from the 14th May 2024 were calibrated with the most recent BCF at this time for XCO of 0.994524. However, the variation is still significantly lower than the observed emissions.

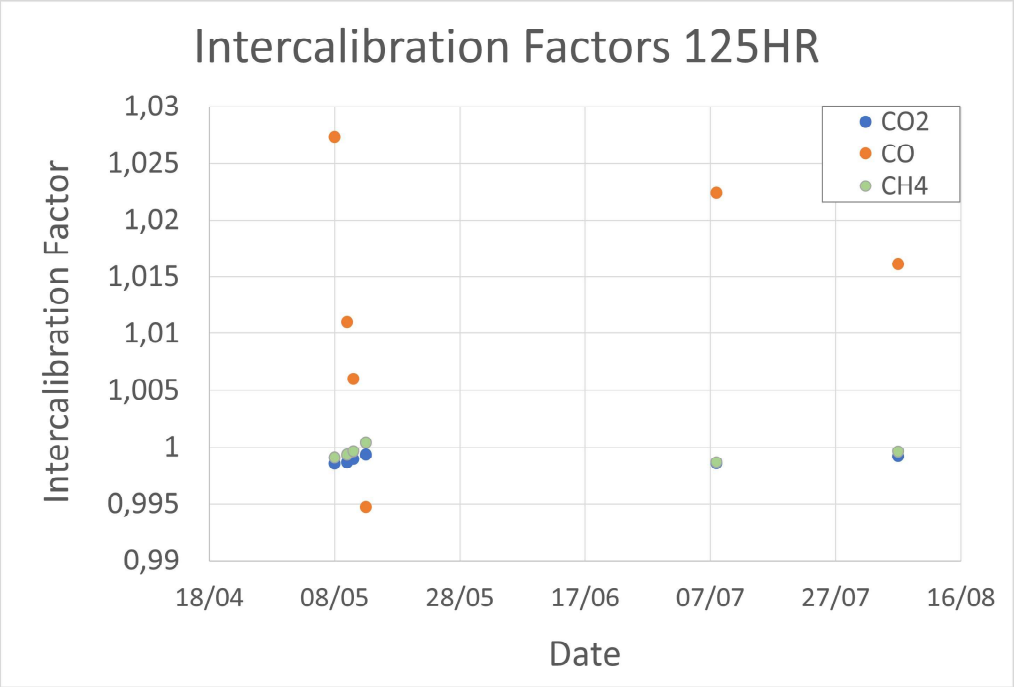

Figure 4.1: Change of the bias compensation factors for XCO_2, XCO and XCH_4 of the EM27/SUN SN82 spectrometer towards the IFS 125HR spectrometer in Bremen.

4.2 Setup of Measurement Site

The lightweight and compact design of the EM27/SUN spectrometer facilitates its deployment in diverse settings, restricted only to the availability of an appropriate power source. The instrument was operated at various locations around the steel plant of Bremen (see Figure 4.3). In addition to the spectrometer, the measurement setup comprises a laptop for spectrometer operation and data storage, as well as a pressure sensor (Vaisala PTB 330) connected to another laptop. All equipment is stored within a metal transport box, which can be transported by car to the designated measurement stations. At the station, the spectrometer is placed on top of the transport box in order to ensure a stable and secure footing. Furthermore, a reflective covering is employed to prevent the instrument from overheating. The requisite power is supplied by a portable power station (Jackery Explorer 2000 Pro). The battery capacity of 2160 Wh enables the device to operate for over ten hours. Furthermore, the operational time can be extended through the utilisation of an additional solar panel (Jackery SolarSaga 200), which generates a surplus of power in excess of that required by the setup. The complete configuration can be seen in Figure 4.2a.

Measurements do not have to be taken at a fixed location; they can also be conducted from a vehicle. In this case, the tailgate of the vehicle must be sufficiently large to allow sunlight to reach the sun tracker and the air conditioning must be operational to ensure that the equipment is adequately cooled. An example of this configuration can be seen in Figures 4.2b and 4.2c.

(a) (b) (c)

Figure 4.2: Different measurement site configurations as an example for measurements at a fixed measurement station (a) or mobile measurements were the EM27/SUN is placed in the trunk of the car (b) connected to the laptop and power supply on the backseats of the car (c).

4.3 Determining the XCO/XCO_2 Ratio in Steel Plant Emissions

This section presents a variety of approaches for quantifying the emission ratio R [%] = XCO [ppm] / XCO_2 [ppm] of the steel production site in Bremen. Method 1 presents a theoretical framework for measuring emissions from a production site stack in the immediate vicinity, whereas Methods 2 and 3 have been applied to EM27/SUN data collected at greater distance of the steel plant. The results are presented in this section. Field measurements have been conducted between the 14th May and 31st July 2024 at different locations around the steel plant, denoted by Station 1 to Station 9. They are shown in Figure 4.3 together with the locations of the three steel plant emission stacks (red) and the two power plant stacks (green). Some station setups are depicted in Section A.1. The location coordinates and the date of the measurement are collected in table A.1.

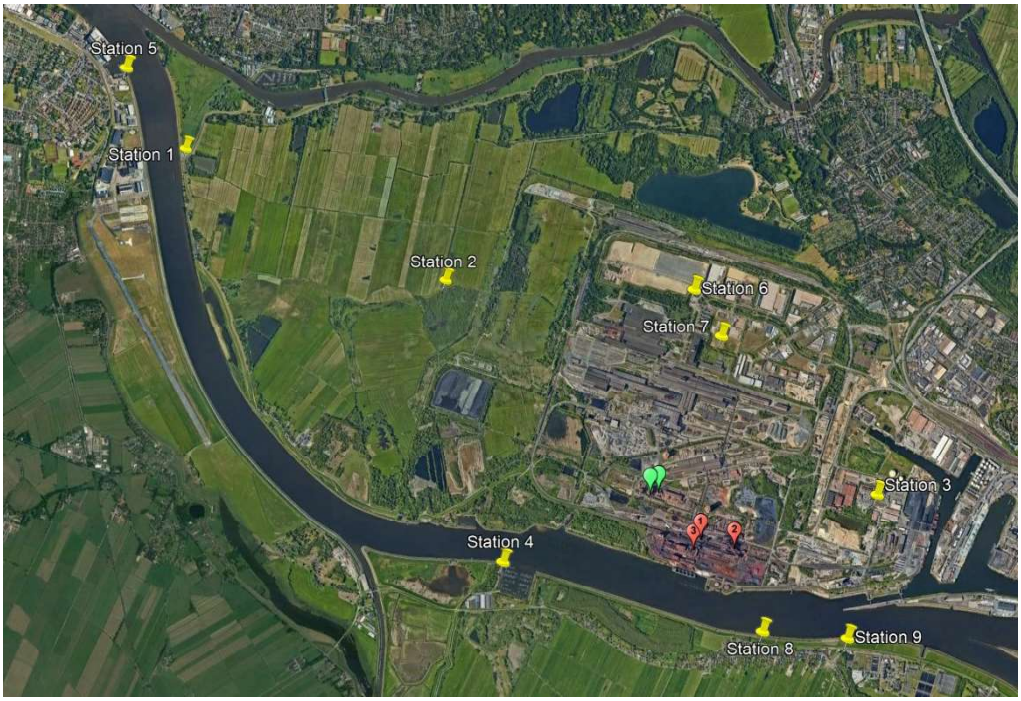

Figure 4.3: Map of the 9 different measurement locations (yellow), the three steel plant stacks (red), including the two blast furnaces (1 and 2), and the stacks of the two neighbouring power plants.

4.3.1 Method 1: Stack Tip Measurements

This method exploits the fact that the EM27/SUN measures the air column within the direct path between the Sun and the instrument. This allows the spectrometer to be configured in a way that it directly measures the air above the stack tip. Furthermore, the optimal position can be adjusted according to the shadow cast by the stack itself. In order to plan such a measurement, it is necessary to have knowledge of the trajectory of the Sun, including the change in azimuth and zenith angle over time, as well as the height of the stack of interest and the distance

to it. A number of websites are already available for this purpose (for example Hoffman 2024). A preliminary measurement for the setup of such an experiment was conducted on 29th July 2024 at the former SWB power plant stack. Figure 4.4 shows the website interface for this specific day including the sun position and the expected shadow of the stack and the chosen measurement location.

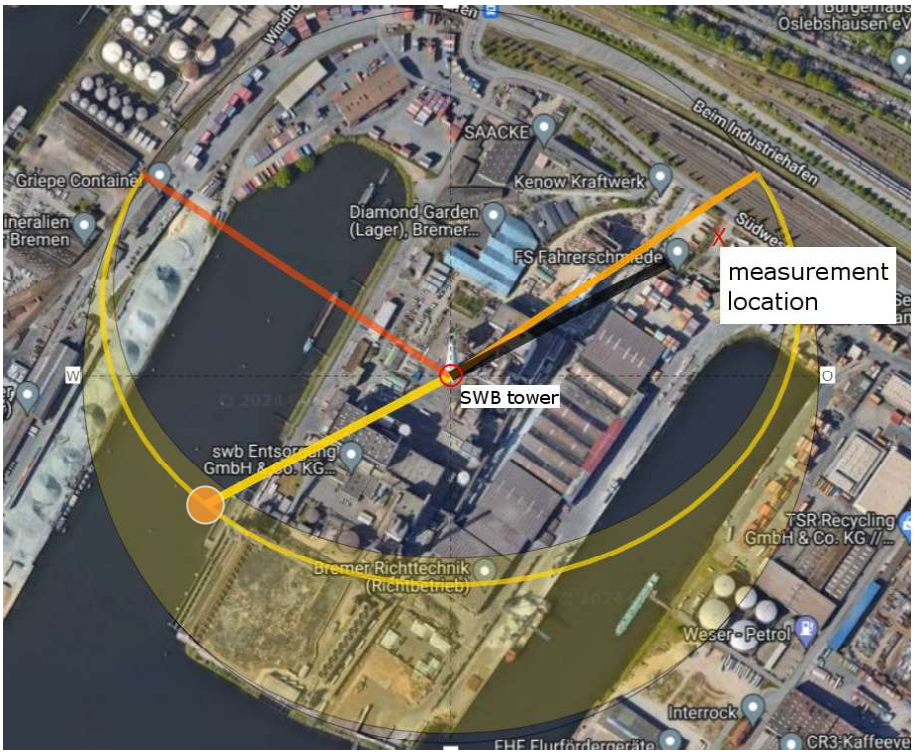

Figure 4.4: Representation of the sun trajectory (yellow line) and the expected shadow of the SWB stack (black line) as shown on the website by Hoffman 2024 on 29th July 2024 at 4.30 pm. The measurement location was chosen according to the shadow position.

Figure 4.5: Sun tracker of the EM27/SUN facing the sun above the SWB stack at 3.40 pm, 4.30 pm and 5.15 pm.

The day was selected based on the favourable meteorological conditions, namely a clear sky and minimal wind activity. These conditions permit the accumulation of the plume above the stack tip, thereby facilitating the measurements. The stack was selected as it was of an appropriate height and easily accessible, allowing for the measurement according to the shadow. Figure 4.5 illustrates the trajectory of the Sun as it crosses the stack tip.

It is not possible to present emission measurements, given that the power plant is no longer in use and no gases are emitted from the stack. Unfortunately, this method has not yet been applicable to the steel plant in Bremen, due to the unavailability of access to the production site. Consequently, alternative methods must be developed that can be applied from greater distances.

4.3.2 Method 2: Ratio Estimation from Absolute Emission Values

In order to measure the emissions of the steel production site from a greater distance, it is necessary to target the transported emission gases, i.e. the emission plume, with the EM27/SUN spectrometer. In order to accurately quantify the plume, it is essential to position the spectrometer in a downwind location relative to the stacks. This requires a certain degree of accuracy in regard to the knowledge of the wind direction. Given the unavailability of current wind data at a sufficiently fine scale around the measurement area, the orientation of active wind turbines was employed as an indicator. The high number of turbines in the vicinity of the steel plant permitted an estimation of the wind direction with a sufficient degree of certainty for locating the dispersed plume at a greater distance.

All measurement stations (see Figure 4.3 and Table A.1) were selected to be in the estimated downwind direction of the steel plant. However, the plume did not always cross the measured air column resulting in no recorded emission peaks at Stations 4 and 7 (see Figures 4.7, A.5). Furthermore, the presence of an excessive number of clouds resulted in the data quality at Station 6 being inadequate (see Figure A.4). Additionally, a modification to the setup at Station 3 rendered the data unsuitable for analysis with PROFFAST. Consequently, the following described methods are applied solely to data collected at Stations 1, 2, 5, 8 and 9. The data are analysed with PROFFAST and corrected in accordance with the BCF.

The collected data for XCO and XCO_2 abundances from the EM27/SUN at the stations and from the 125HR at the university are presented in Figures 4.6 to 4.8. The measurements were conducted at different times of day, defined by the weather conditions. Instead of a constantly increased gas abundance corresponding to the emission plume, emission peaks can be observed. However, the data from Stations 1, 2, 5, 8 and 9 indicate an increase in XCO and XCO_2 gas abundances at the measurement stations in comparison to the 125HR. The XCO_2 peaks exhibit an increase of up to 3 ppm for Stations 1, 2 and 5 and up to 5 ppm for Stations 8 and 9. The peaks in XCO exceed an 50 ppb increase at Stations 1, 2 and 5 with respect to the 125HR records and 100 ppb at Stations 8 and 9. The data from Station 4 do not show a notable difference compared to the 125HR data.

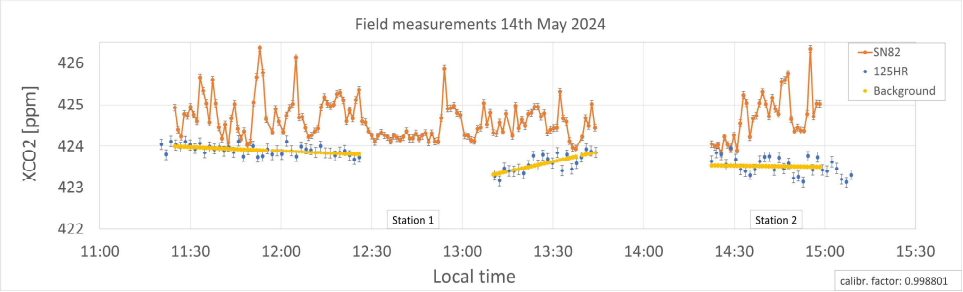

(a)

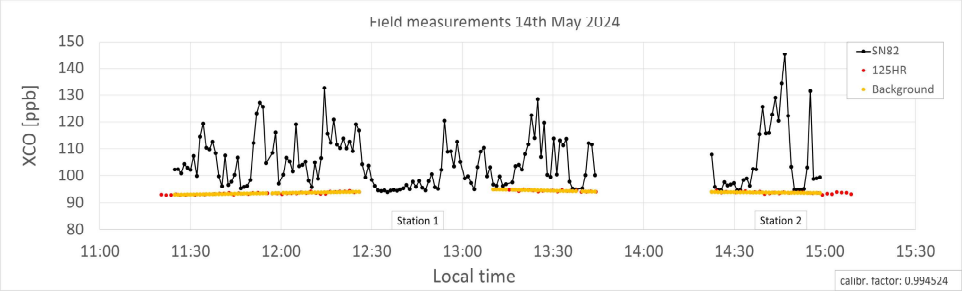

(b)

Figure 4.6: Corrected abundances for a) XCO_2 and b) XCO abundances collected with the EM 27/SUN SN82 at Stations 1 and 2 (orange/black) in comparison to data collected by the IFS 125HR (blue/red) and the fitted background (yellow).

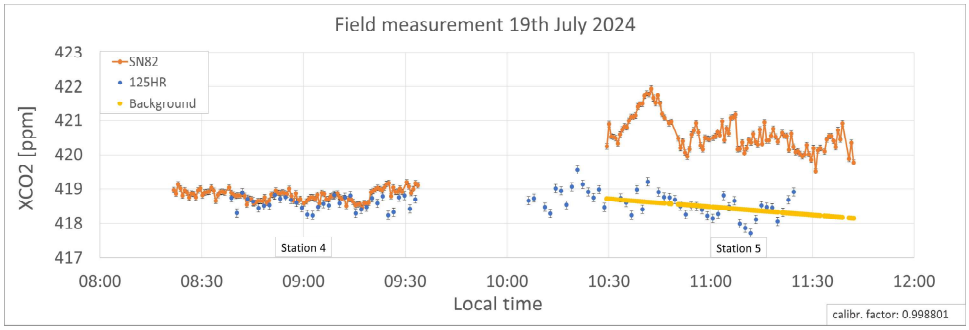

(a)

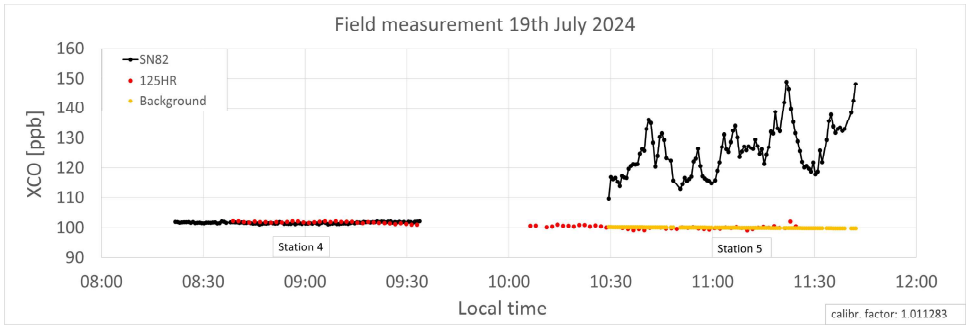

(b)

Figure 4.7: Corrected XCO_2 (a) and XCO (b) abundances collected with the EM27/SUN SN82 at Stations 4 and 5 (orange/black) in comparison to data collected by the IFS 125HR (blue/red) and the fitted background (yellow).

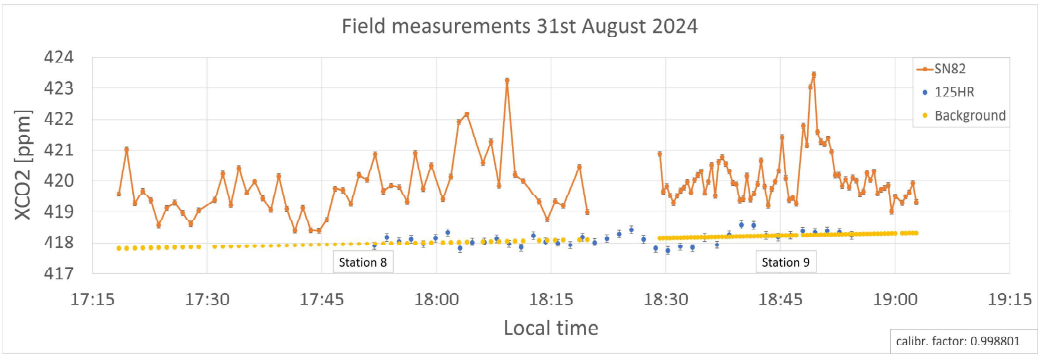

(a)

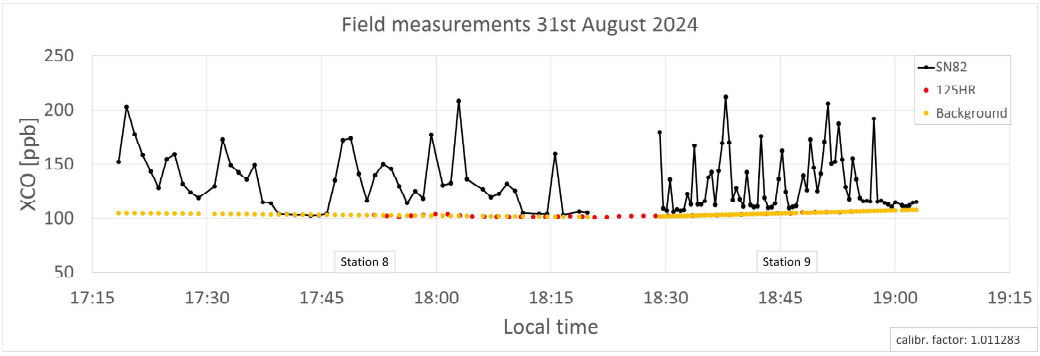

(b)

Figure 4.8: Corrected XCO_2 (a) and XCO (b) abundances collected with the EM27/SUN SN82 at Stations 8 and 9 (orange/black) in comparison to data collected by the IFS 125HR (blue/red) and the fitted background (yellow).

In order to obtain a quantitative measure of the absolute emissions from the steel production site, it is necessary to subtract a background value from the XGas values measured at the stations. This was conducted on the assumption that the background is represented by the measurements taken with the IFS 125HR spectrometer at the NW1 building of the University of Bremen. The location is sufficiently close to permit this approximation, situated to the east-southeast of the steel plant. Consequently, it is not in the downwind direction of the production stacks on the days of interest and is therefore not influenced by their emissions. Furthermore, an examination of data from Station 4, which was not affected by the emission plume, corroborates the validity of this assumption, because the gas abundances for both XCO_2 and XCO are nearly identical between the SN82 at the steel plant and the 125HR at the NW1. To allow for a meaningful comparison of the results, the 125HR was operated in a configuration identical to the EM27/SUN (averaging 10 double-sided interferograms collected with a spectral resolution of $0.5\,\mathrm{cm}^{-1}$) and the obtained interferograms were analysed with the PROFFAST software.

The background is calculated by a linear fit of the 125HR data and then subtracted from the SN82 data to determine the XGas abundances of the emissions. The ratio can then be determined by $R = \mathrm{XCO}_{emission}/\mathrm{XCO}_{2,emission}$. The error is obtained through Gaussian error propagation, as outlined in Section A.6. The calculated ratio is expressed as a percentage and illustrated in Figure 4.9. It exhibits a range of 0 % to 5.42 %, with an overall mean value and standard deviation of $\overline{R} = 1.31 \pm 0.91\,\%$.

The observation of emission peaks highlights the rapid alteration in the plume trajectory, whereby it repeatedly intersects with the monitored air column. Consequently, there are also periods during which no plume is measured, resulting in XCO_2 and XCO values reaching the background level. An XCO_2 abundance at background level gives rise to high ratios with large errors. An XCO abundance approaching the background level results in ratios approaching zero. Although these values indicate a small error, they are meaningless in that no emission is actually measured. The small error is simply the result of the multiplication with the near-zero ratio itself within the error calculation (refer to Section A.6).

Therefore, it is more accurate to exclude XGas abundances close to the background level before calculating the ratio. The selected criteria are that the difference between the station value and the background value must exceed 0.5 ppm for XCO_2 and 5 ppb for XCO. This results in a revised mean ratio of $\overline{R} = 1.46 \pm 0.86\,\%$. This threshold appears to be the minimum appropriate for the data from Stations 1 and 2. For Stations 8 and 9, a filter threshold of 10 ppb appears to be more accurate for XCO to exclude all plateaus between the emission peaks. This may be attributed to the shorter distance of the stations to the steel plant, which allows for the accumulation of CO around this area - irrespective of the plume direction - increasing the background level. The aforementioned threshold adjustment for Stations 8 and 9 yields in a mean ratio of $\overline{R} = 1.54 \pm 0.85\,\%$. This represents the best estimate. If the threshold for XCO is set to 10 ppb for all stations, the mean ratio is found to be $\overline{R} = 1.62 \pm 0.85\,\%$.

This method is based on the assumption that the background at the steel plant is identical to the gas abundances measured by the 125HR. Furthermore, the plots demonstrate that peaks in XCO_2 are not consistently accompanied by an XCO increase at the same time step, and vice versa. CO_2 emission peaks, which are not accompanied by an CO increase, likely correspond to a measurement of other CO_2 emission sources or a not consistent mixing of the plumes of the different stacks of the steel production site. In order to reduce the dependency on the background and, consequently, the dependency on the accuracy of the BCF, and to attempt the disentanglement of different emission sources, a third method is developed and presented in the following section.

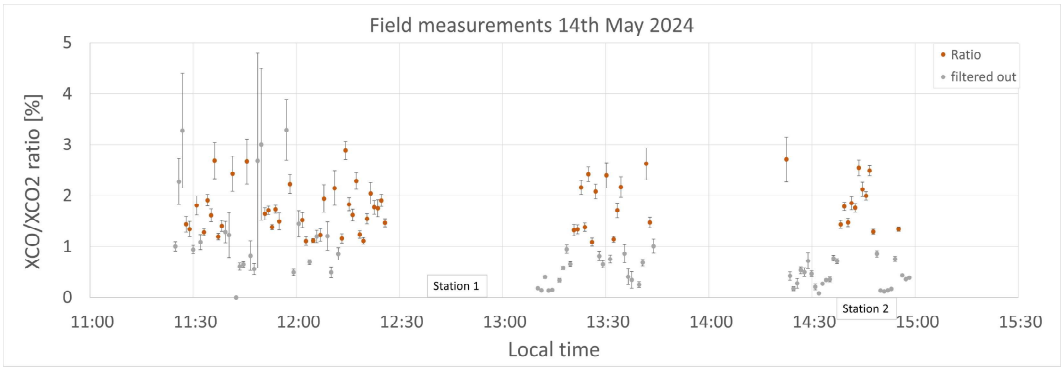

(a)

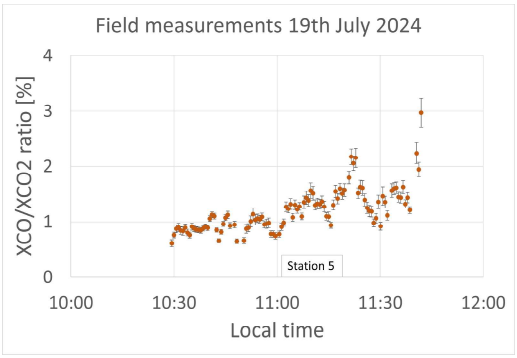

(b)

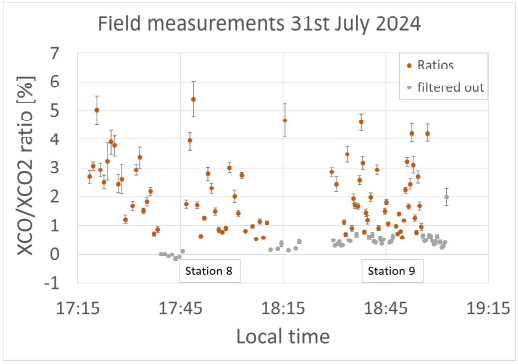

(c)

Figure 4.9: Calculated XCO/XCO_2 ratios by absolute emission abundances measured at a) Stations 1 and 2, b) Station 5 and c) Stations 8 and 9. Ratios calculated from XCO_2 not larger than 0.5 ppm and XCO not larger than 10 ppm with respect to the background are indicated in grey colour.

4.3.3 Method 3: Ratio Estimation from Differential Emission Values

A first analysis of the recorded data revealed some challenges in precisely determining the XCO/XCO_2 emission ratio for the steel production site from a greater distance. It became evident that a number of factors preclude the possibility of maintaining a constant measurement of the emission plume. The frequently changing wind directions, atmospheric features such as the upwind over the river Weser adjacent to the steel production site, other potential emission sources, and the complex viewing geometry lead to the result that the plume is frequently changing between being inside and outside the measured air column. However, this should be leveraged as an opportunity to ascertain the ratio of the emissions. It can be assumed that the steel production site is the primary source of CO and CO_2 in the area such that peaks observed in both gas abundances can be accounted to it. Thus, an increase in XCO_2 accompanied by an increase in XCO indicates that the plume is traversing the measurement column. Instead of using the absolute emission values in relation to a background, the differences in XCO and XCO_2 between two time steps within an aforementioned emission peak provide the amount of CO and CO_2 contributed by the steel production site. It is therefore possible to use these differences to determine the ratio.

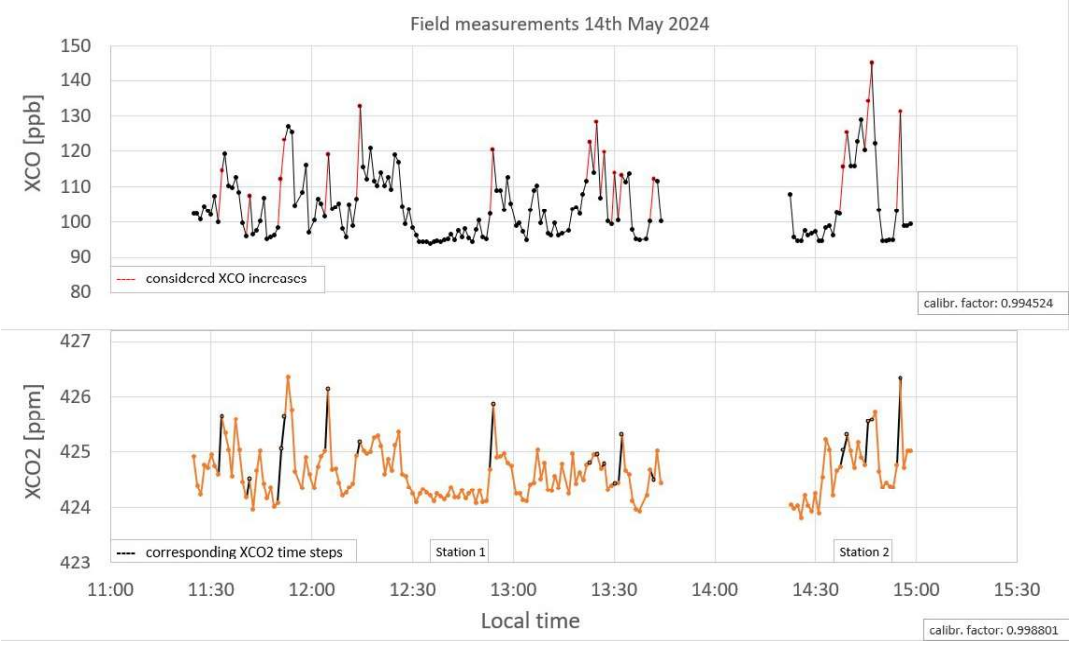

Figure 4.10: Recorded XCO (black) and XCO_2 (orange) abundances at Stations 1 and 2. XCO increases exceeding $6\,\mathrm{ppb\,min^{-1}}$ are highlighted in red, as well as the corresponding change in XCO_2 in black.

In order to avoid the consideration of differences that are only caused by noise and measurement uncertainty, a threshold is introduced for filtering the data. Moreover, the relative error in the ratio decreases with an increase in the difference between two measured abundances. Filters are chosen according to different assumptions.

A first assumption is that the steel production site is the primary emission source for CO in the measurement area. The recorded data can thus be filtered for time intervals showing a notable increase in XCO. The threshold is set to be 10 ppb between two measurements, each averaging 10 interferograms ($\approx 6\,\mathrm{ppb\,min^{-1}}$). This criterion was applied to the data set and is shown for the data from Stations 1 and 2 in Figure 4.10 as a representative example. It can be observed that not every increase in CO is accompanied by an increase in CO_2. The measurement is more sensitive to changes in CO as the emissions are larger in relation to the low background. Therefore, when the plume is measured, it is observed as plateaus of increased abundance in XCO_2, while the CO recording shows a series of abundance peaks. As a result, the ratio calculation for the data filtered in accordance with this assumption is highly variable and imprecise, as illustrated in Figure 4.11. The ratio for individual time steps varies between - 69.23 % and 717.97 %.

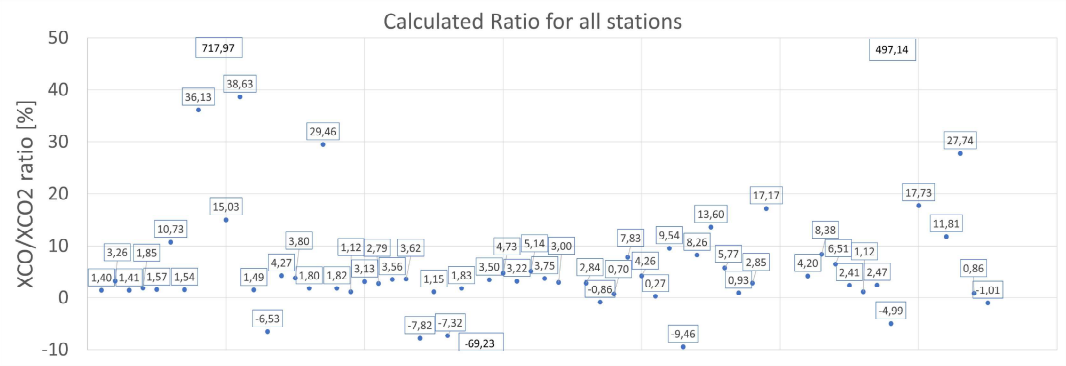

Figure 4.11: Ratios calculated for all stations under the criterion of filtering for increases in XCO exceeding a change of $6\,\mathrm{ppb\,min^{-1}}$.

The steel production site is an emitter of both CO and CO_2; thus, a second assumption can be made, namely that an increase in XCO_2 must be observed. In this way, only the initial moment when the plume moves into the measured air column is considered. The threshold for CO_2 is set at 0.5 ppm between two measurements, each averaging 10 interferograms ($\approx 0.3\,\mathrm{ppm\,min^{-1}}$). The additional application of this criterion results in a more consistent calculation of the ratio, as illustrated in Figure 4.12. The drawback of this data filtering method is that the number of data points used for the ratio calculation is significantly reduced. Not only increases in the XGas abundances can be considered but also decreases, which occur when the plume is moving out of the measured air column. This is represented in Figure 4.13 for the data of Stations 1 and 2. This third assumption can therefore be additionally used to quantify the emission ratio of the steel production site while simultaneously increasing the number of data points. The ratios filtered by these three assumptions exhibit a markedly reduced degree of variation in comparison to the unfiltered data. Additionally, the number of data points is increased (compare Figure 4.14 and 4.12).

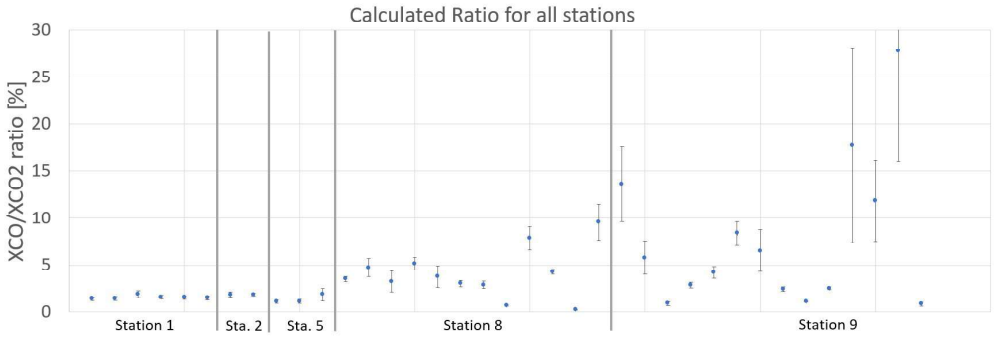

Figure 4.12: Ratios calculated for all stations under the criteria of filtering for increases in XCO exceeding a change of 6 ppb min^{-1} and increases in XCO_2 exceeding a change of 0.3 ppm min^{-1}.

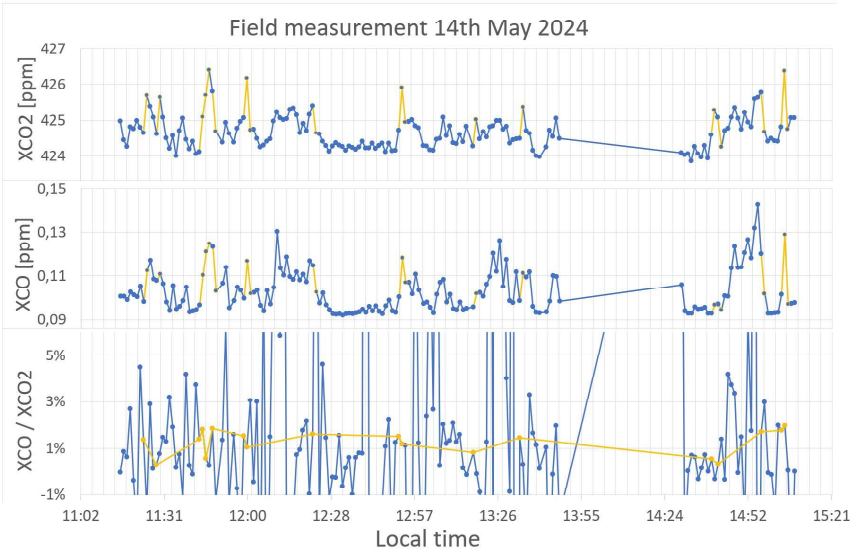

Figure 4.13: Ratios calculated for all stations. Data points meeting the criteria of increases in XCO exceeding a change of 6 ppb min^{-1} and increases in XCO_2 exceeding a change of 0.3 ppm min^{-1} are highlighted in yellow.

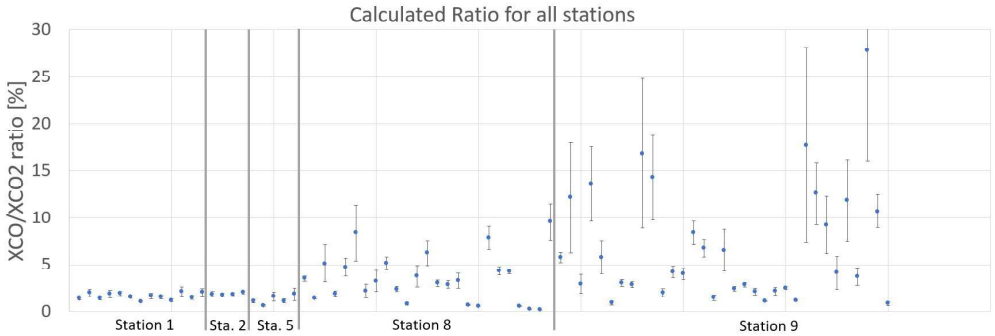

Figure 4.14: Ratios calculated for all stations under the criteria of filtering for both increases and decreases in XCO exceeding a change of 6 ppb min^{-1} and increases in XCO_2 exceeding a change of 0.3 ppm min^{-1}.

The plotted ratio in Figure 4.14 shows different behaviour for the different stations. While a low variation and a smaller mean are observed in the data from Stations 1, 2 and 5, the data indicate a larger spread and higher mean at Stations 8 and 9. This can be attributed to a number of factors. One contributing factor is the distance between the measurement station and the steel plant. The steel production site comprises multiple emission stacks, which are likely to emit with different XCO/XCO_2 ratios. A more detailed examination of the emissions from the nearby Stations 8 and 9 (see Figure 4.8) indicates a shift in emission peaks for XCO and XCO_2, which could be attributed to the fact that the plumes of the different stacks are still distinguishable and do not traverse the monitored air column simultaneously. Contrarily, the emissions at the more distant stations are presumably well-mixed. This effect is strengthened by the viewing geometry: The emission stacks of the steel production site are oriented along a direction that is nearly parallel to the line of sight to the more distant stations. Stations 1, 2 and 5 are located north-west of the steel production site, and measurements were taken at noon when wind from the south-east was mixing the individual plumes immediately after the exhaust. The locations of Stations 8 and 9 are to the south-east of the steel plant. The measurements at these stations were conducted in the late afternoon, with the Sun in the north-west. In order for the plume to traverse the measured air column, the wind was blowing from the north-east, perpendicular to the orientation line of the emission stacks. As a result, the individual plumes were not mixed immediately. However, this also means that the purely CO_2 power plant emissions are not always measured together with the steel plant emissions, leading to higher measured CO/CO_2 ratios which might be attributed to the steel plant emission ratio. Furthermore, the smaller the distance to the emission source, the narrower is the plume. As a result, it can be difficult to monitor the traversing plume at a near station with the necessary temporal resolution. This challenge was tackled by decreasing the number of averaged interferograms per measurement from 10 at Station 1 and 2, to 6 at Stations 5 and 8, down to 4 at Station 9. But clearly the XGas abundances are still rapidly changing in the data of Station 9.

These factors lead to the conclusion that two cases have to be distinguished: The measurements obtained from Stations 1, 2 and 5 give more consistent results for a steel production site emission ratio. The measurements obtained from Stations 8 and 9 are highly variable but might indicate results closer to the steel plant emission ratio. The mean XCO/XCO_2 emission ratio derived for Stations 1, 2 and 5 is found to be $\overline{R} = 1.58 \pm 0.36\,\%$, which is in good agreement with the result obtained using Method 2, with an improved standard deviation. This shows the good consistency between Method 2 and Method 3 for the calculation of the steel production site emission ratio for these stations. The mean XCO/XCO_2 emission ratio derived with Method 3 for Stations 8 and 9 is found to be $\overline{R} = 5.29 \pm 5.14\,\%$.

The drawback of Method 3 is that the choice of the XGas thresholds influences the ratio. In order to evaluate this influence, the production site emission ratio was calculated for Stations 1, 2 and 5 with varying thresholds defining the minimum change in XGas abundances considered for the ratio calculation. With the help of the number of data points and the variance of the calculated mean ratio (see Figure A.7), a quality metric was derived.

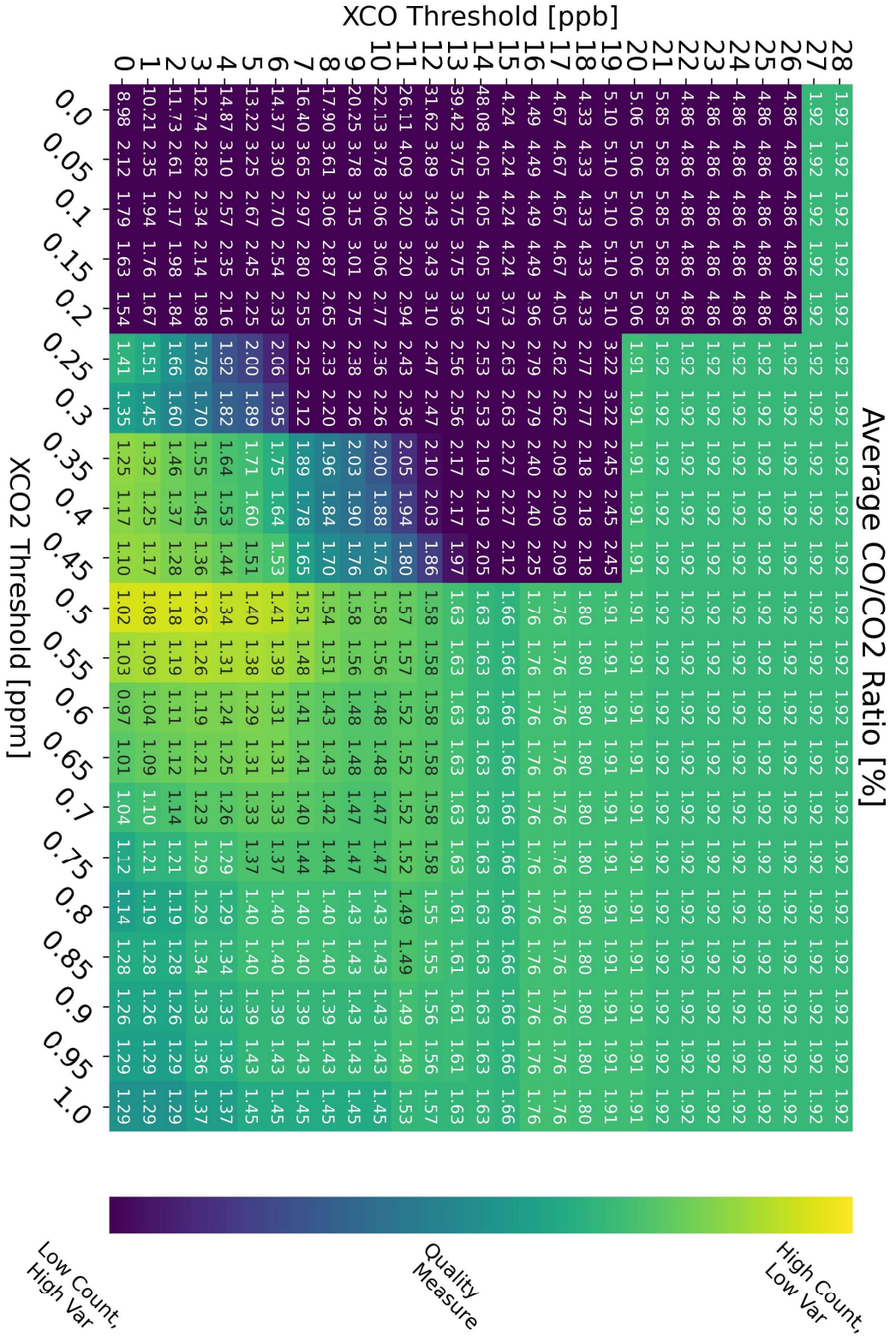

Figure 4.15: Steel production site emission ratios calculated for Stations 1, 2 and 5 in dependence on different XCO and XCO_2 thresholds. The threshold defines the minimum change in XGas abundances between two 10-scans measurements. The background color is set by a quality metric, defined by the standard deviation and the number of data points, indicating accurate (yellow) and less accurate (blue) values.

The ratios shown in Figure 4.15 are colored according to the quality metric. The lighter the color the more accurate the ratio. The data point count is decreasing from the plot origin towards the upper right corner where the thresholds are set higher, exceeded by less XGas abundance differences (see Figure A.7a). The variance does not show such a clear pattern. It is very high for low thresholds as the ratio from small differences is highly influenced by measurement noise (see Figure A.7b).

It can be observed that the thresholds of 10 ppb for XCO and 0.5 ppm for XCO_2 were well chosen, representing an accurate estimate of the XCO/XCO_2 ratio. The plot suggests that the precision is improved by lowering the XCO threshold as the number of data points increases without increasing the variance. This should be treated with care, as lowering the threshold only for the numerator of the ratio includes more ratios close to zero. These values might not reflect the true ratio but also do not increase the variance significantly. However, the data leads to the conclusion that production site ratios with a low variance lie all within the interval of 1.02 to 2.05 %.

The emission ratio obtained by the EM27/SUN measurements ($\overline{R} = 1.54 \pm 0.85\,\%$ with Method 2 and $\overline{R} = 1.58 \pm 0.36\,\%$ with Method 3 for Stations 1, 2 and 5) can be interpreted as the ratio characterising the emission of the entire steel production site. It is in agreement with the steel production site emission ratio calculated by the values of the thru.de portal of 1.49 %. In order to allow for a comparison with the steel plant emission ratio for the specific steel plant of $6.28 \pm 4.09\,\%$ and the overall sector-specific 5.09 % (4.27 % - 6.11 %, 1σ) as determined by satellite-based measurements (Schneising et al. 2024), the theoretical steel plant emission ratio from the measurements can be calculated. Under the assumption that the relative ratio of the the CO_2 emissions of the power plant and the steel plant as given in the thru.de portal is correct, the steel plant emission ratio can be estimated. Therefore, the whole amount of the measured CO is attributed to the steel plant and the steel plant emission ratio is calculated according to the theoretical CO_2 fraction accounted to the steel plant. This results for Method 2 in a revised CO/CO_2 emission ratio of $3.46 \pm 0.85\,\%$, which is still markedly lower than the ratio determined by Schneising et al. 2024 but in good agreement with the theoretical value from the thru.de portal of 3.33 %. An illustrative comparison is given in Table 5.1.

Further reasons for this difference have yet to be investigated but possible factors shall be discussed here. Firstly, the study based on satellite measurements did not measure the CO_2 emissions directly but relied on emission data from the EU ETS. The higher ratio could be the result of an underestimation of the CO_2 emission. Next, further measurements must be conducted at sites in diverse directions and at varying distances from the steel production site in order to assess how well the individual plumes are mixed. Finally, it has yet to be established whether the steel plant operates using a consistent production process or alternates between different production steps, which could result in fluctuations in the CO/CO_2 emission ratio.

4.3.4 Lagrangian Transport Model

Lagrangian transport forward models can be used for the simulation of emission plumes and the determination of their properties. The trajectories of particles emitted by a source are calculated by utilising meteorological data fields as described in Section 2.6. A model run was conducted to simulate the emissions of the steel production site on 14th May 2024, when EM27/SUN measurements were taken at Stations 1 and 2. Given that the trace gases of interest are CO and CO_2 and that the plume is measured in cloud-free conditions, both precipitation and radioactive decay can be considered to have no influence on the simulation. The detailed configuration of the FLEXPART model can be found in Section B.0.3. Model and meteorological data were provided by Dr. Poulidis from the LAMOS group of the IUP Bremen.

The emissions are simulated from a point source located at the largest stack of the steel plant, situated at 53.125 °N and 8.688 °E, and 125 m in height. Assuming a stack exhaust diameter of 3 m, the plume rise above the tip, resulting from the typical exhaust velocity of 15 m/s, is approximately 5 m (ASHRAE 1996). Accordingly, the particle release is set at the line from 125 to 130 m above the stack. It is assumed that the emission occurs at a constant rate between 1 a. m. and 10 p. m., with a total of 100 000 particles emitted, having a total mass of $5.5 * 10^9$ kg. This is an arbitrary number as default value that can be scaled according to the measurements.

The data product contains concentrations in mass per volume, recorded at 10-minute intervals on a pre-defined output grid. The grid encompasses a rectangular area surrounding the steel production site, extending from 53.11 °N, 8.59 °E to 51.185 °N, 8.715 °E. The grid cell size is 0.0025 °N × 0.0025 °E. The altitude dimension comprises 77 layers, extending from ground level to an altitude of 20 000 m. The layer thickness increases with altitude, allowing for higher resolution at the emission level.

Figure 4.16 illustrates the result of the emission plume simulation. It shows the concentration of the plume as a mass per unit area integrated over the vertical columns. The plot demonstrates that the wind direction and therefore the plume trajectory direction remained relatively constant throughout the day under study. In contrast, the shape of the plume, especially its width, undergoes a change over the course of the day. Prior to sunrise and following sunset, the plume is observed to be narrower than during the diurnal period. This is attributed to the smaller mixing during the nocturnal hours. The variation during the daytime, and therefore during the measurements with the EM27/SUN, is considerably smaller (see Figure B.4 for further details). As illustrated in the subplot at 12:10 a. m., the simulation indicates that the plume traversed both measurement stations.

An additional dimension of interest is the height of the plume. Figure 4.17 illustrates the development of the plume height over a day. It can be observed that the plume reaches the ground in the immediate vicinity of the stack during the daytime due to the presence of high vertical mixing. In contrast, minimal vertical mixing occurs during nocturnal hours, resulting in a plume that concentrates within a specific height layer (see Figures B.7 and B.8). It should be noted that FLEXPART approximates the nocturnal boundary layer as completely stable, which raises the question of how large the actual diffusivity is during the night.

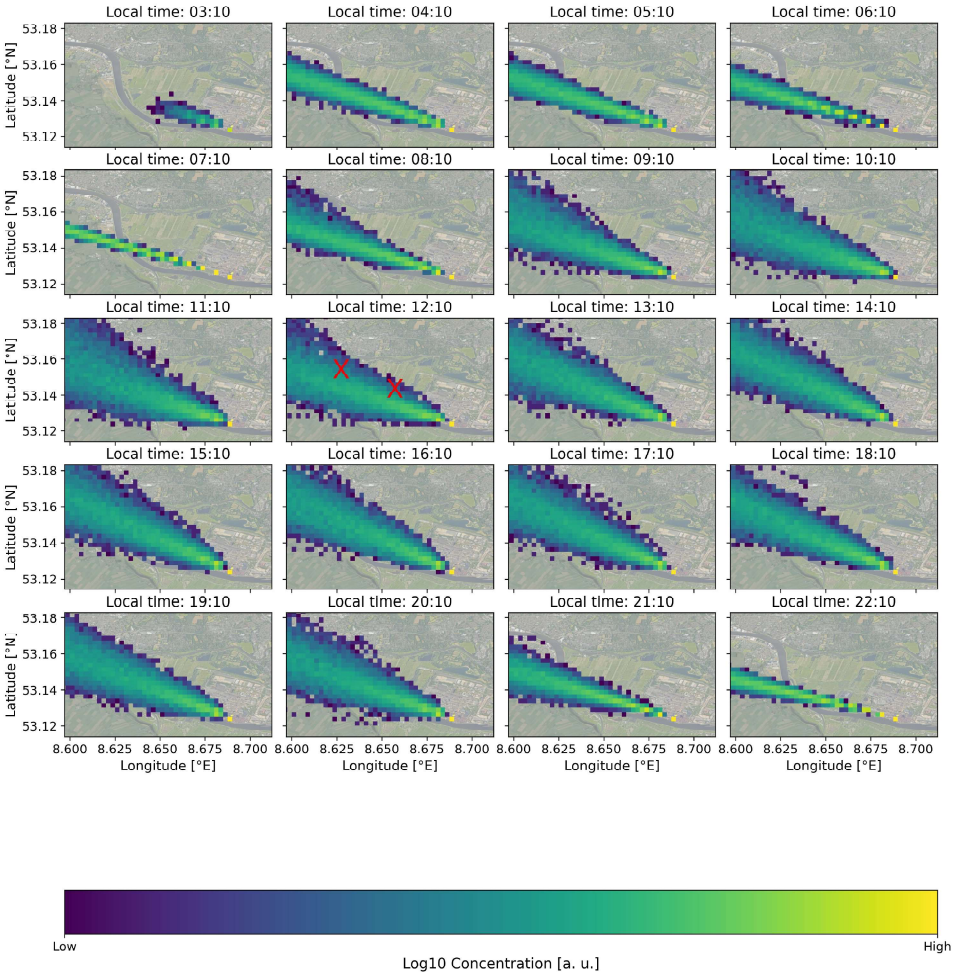

Figure 4.16: Plume shape and trajectory simulated with FLEXPART for 14th May 2024. The illustrated concentration [mass/area] is given on a log10 scale. The subplot at 12:10 includes marks for the measurement Stations 1 and 2.

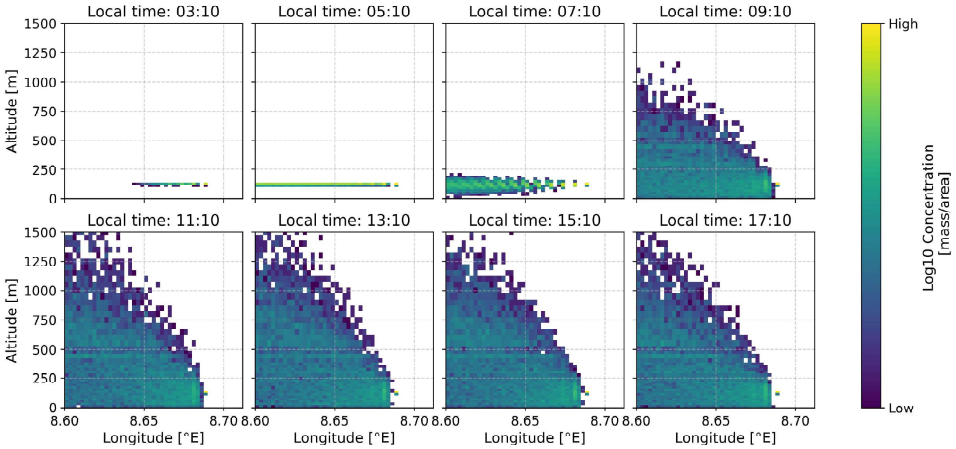

Figure 4.17: Plume height as a function of longitude simulated with FLEXPART for 14th May 2024. The illustrated concentration [mass/area] is given on a log10 scale.

This understanding of the plume characteristics may facilitate the deployment of additional measurement methodologies, such as in-situ observations in the vicinity of the steel plant during daytime hours or tall tower measurements at greater distances during nocturnal hours.

Moreover, the simulation can be combined with the EM27/SUN measurements, thereby enabling an estimation of the steel production site emissions. By focusing on the time intervals of the measurements and the location of the measurement sites (see Figures B.4 to B.6), it can be seen that the plume crossed the slant column measured by the EM27/SUN. In order to calculate the simulated concentration that would have been observed by the EM27/SUN at Station 1 during the measurement period on 14 May, the grid boxes of the model output containing concentration data are aggregated over the column of interest. To this end, the vector between the location of measurement Station 1 and the current position of the Sun is determined for each simulated time step. Next, the aforementioned path is divided into discrete segments of 0.5 m. The path length is multiplied by the corresponding concentration (mass × volume), as provided by the simulation for the grid box containing the specified length step. The overall concentration in units of mass per area is obtained by summing up the contributions of each step. The result of the calculation is then compared to the XCO abundance measured by the EM27/SUN at Station 1 at the same measurement time, as illustrated in Figure 4.18.

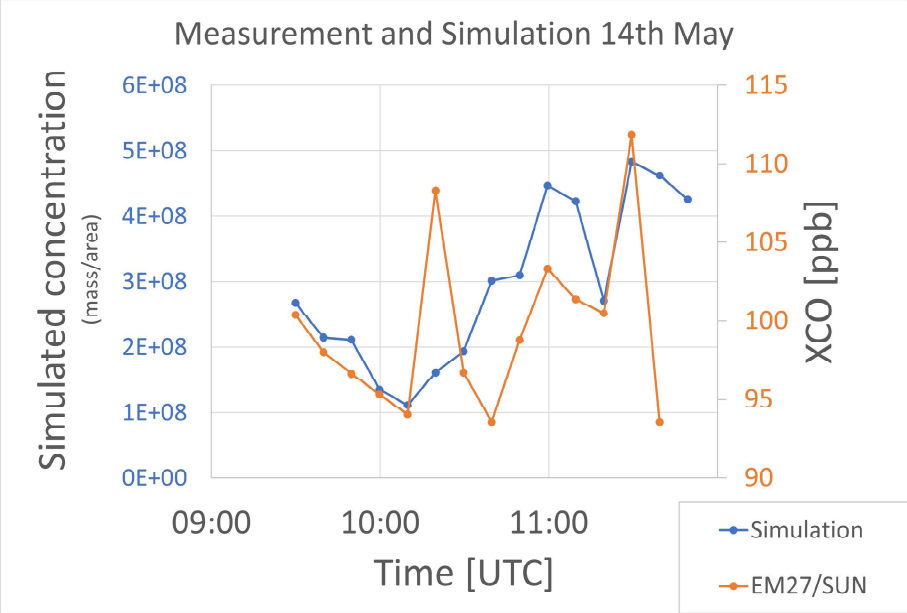

Figure 4.18: Comparison of the XCO concentration measured by the EM27/SUN (orange) and the simulated column load due to the steel plant emissions for the slant column (blue) for Station 1.

The plot demonstrates a distinct discrepancy between the simulated column concentration and the measured gas abundance. While both values exhibit a comparable decline over the initial 40 minutes, the measured XCO records a pronounced emission peak that is not evident in the simulation. Subsequently, both variables demonstrate an increase, which is then followed by a pronounced decline in the

measured XCO, a phenomenon not observed in the simulated concentration. This result suggests that the simulation may be employed to estimate the emissions from the steel production site for a slowly varying plume, but is less effective at tracking rapid changes, which are likely to be caused by quickly changing wind patterns of short duration.

The following section investigates whether a mass balance approach can provide a first estimation of the total emissions from the steel production site. In this context, a mass balance approach means to attribute the total measured gas enhancement to the plume as simulated with the model. A scaling of the simulated column such that it matches the measurement leads to an estimate of the total emissions. The measured emission signal is obtained by subtracting the measured number of CO molecules in the background (125HR) from the calibrated station measurement (EM27/SUN). This value is directly provided by the PROFFAST analysis for the total column in molecules/m^2. It is then multiplied by the molecular weight of CO $m_{CO} = 4.65 * 10^{-23}$ g to yield a mass per unit area. As the total emitted mass for the simulation was kept at the default value of $5.5 * 10^9$ kg, it is necessary to scale the simulated values to match the measured values. The mean scaling factor is found to be $2.40 * 10^{-5} \pm 0.53 * 10^{-5}$. The scaled simulated concentration and the calculated measured concentration are shown in Figure 4.19. It is evident that the measured data exhibits a greater degree of variability due to the temporal sensitivity to wind gusts. The overall mean appears to exhibit a similar slope. If the total emission mass is scaled in accordance with the aforementioned factor, it corresponds to 6.29 ± 1.39 t/h of CO emissions and accordingly 55.06 ± 12.16 kt/yr. This result appears to be reasonable when compared to the values found by Schneising et al. 2024 of 92 ± 59 kt/yr and the CO emission estimate of 71.9 kt/yr of the thru.de portal (Umweltbundesamt 2022).

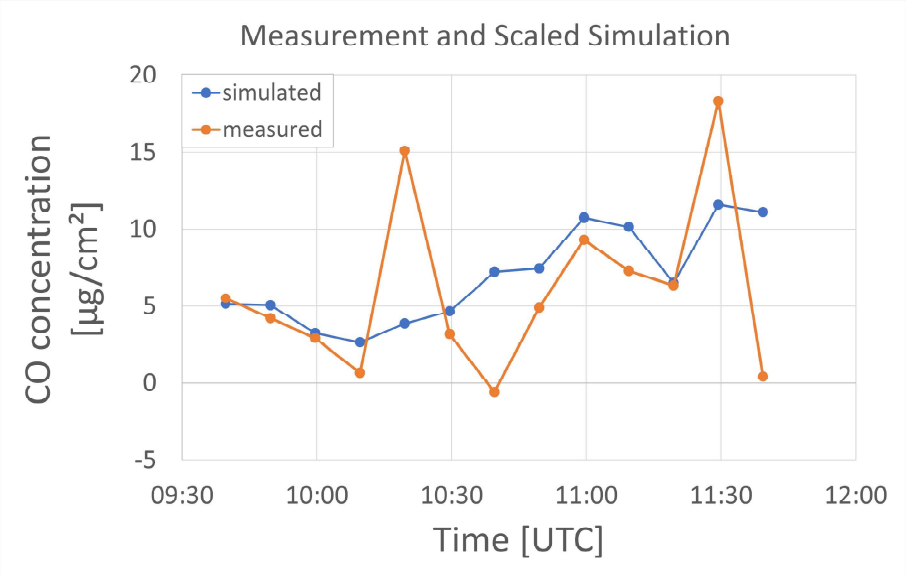

Figure 4.19: Comparison of the XCO concentration measured by the EM27/SUN (orange) at Station 1 and the corresponding simulated column load due to the steel plant emissions for the slant column (blue) scaled for a best fit.

This shows that the CO emissions yielded by this straightforward mass balance methodology are in line with the other emission estimates, suggesting that this approach can be utilized to ascertain the overall emissions from a strong point source. The accuracy can be significantly enhanced by incorporating multiple factors: While the XCO BCF was used to correct the number of CO particles measured by the EM27/SUN, a BCF specifically for the CO particles ought to be established. A more robust result can be obtained by considering the averaging kernel of the FTIR spectrometer and simulating a measurement that corresponds to the emissions modeled by FLEXPART. This was not yet implemented as the accurate averaging kernel could not yet be accessed. For the height of the plume, the averaging kernel is slightly smaller than 1 and the application would lead to a larger emission estimate. Additionally, the simulation itself can be optimized by combining the FLEXPART model with the numerical Weather Research and Forecasting (WRF) model, thereby increasing the resolution of the meteorological data, which plays a pivotal role in small-scale simulations of single point sources.

Nevertheless, applying the same approach to the measured CO_2 emissions and scaling the simulated column load accordingly results in an emission estimate of $2.36 \pm 0.52\,\mathrm{kt/h}$ and, hence, $20.6 \pm 4.59\,\mathrm{Mt/yr}$. The calculation exceeds thereby the expected value of $2.3\,\mathrm{Mt/yr}$ by one order of magnitude. This emphasises again that the CO_2 emissions from the power plant and from the steel plant are still distinguishable. The CO emissions can be nicely simulated by a single emission source because it is only emitted by the steel plant. In order to obtained an estimate of the CO_2, at least two emission sources have to be simulated, an additional one for the power plant. Moreover, the mass balance approach can be substituted with a backwards Lagrangian inverse modelling approach that employs a priori emission maps. In conjunction with more measurement points in vicinity of the steel production site, sampling different parts of the plume, this approach appears to hold considerable promise for future applications of inversions in emission estimation. Nevertheless, the application of this methodology would extend beyond the scope of this thesis.

4.3.5 DOAS Measurements

DOAS measurements were conducted at the steel production site on 1st August 2024 and supported by Thomas Visarius and Dr. Kezia Lange of the IUP Bremen DOAS group. The objective is to ascertain whether DOAS can provide additional value in emission plume measurements with the EM27/SUN. Moreover, the effectiveness and complementarity of the two different measurement techniques in various conditions is analysed. The configuration of the instruments is demonstrated in Figure 4.20.

(a) (b)

Figure 4.20: Mobile measurements were conducted by car with simultaneous employment of a DOAS instrument and an EM27/SUN spectrometer. a) The car and the two sensors of the DOAS instrument (red cirlce, vertically upwards) and the EM27/SUN (red arrow, directed towards the Sun). b) Configuration inside the car showing the Laptop of the EM27/SUN and the DOAS unit.

Initially, car DOAS measurements with an average speed of 30 km/h were conducted along roads perpendicular to the expected wind direction (hence, direction of the plume movement) at various distances from the emission source. The wind, blowing from the north-northeast, carried the plume toward the south-southwest, which was ideal as the roads lead from west to east. This initial phase involved recording data along these transects to establish the presence and spread of the emission plume. Two of such transects are shown in Figure 4.21.

The findings confirm that the plume could be effectively detected and significant conversion of emitted nitrogen oxide (NO) to NO_2 took already place. The increasing spread of the plume can be observed by comparing the transect taken at a distance of approximately 900 m to the emission stack in Figure 4.21a with the cross-section recorded at a distance of approximately 1400 m in Figure 4.21b. The plume cross-section increases from approximately 400 m to 1 000 m. Moreover, the higher column loads of NO_2 observed at the greater distance can be attributed to either an ongoing conversion of NO to NO_2 or varying NO_2 emissions. A more detailed analysis of these properties would be possible if both measurements were collected within a shorter time interval. In fact, consecutive measurement drives were conducted at four different distances within 20 minutes. However, the GPS recording was interrupted, preventing the retrieval of meaningful data.

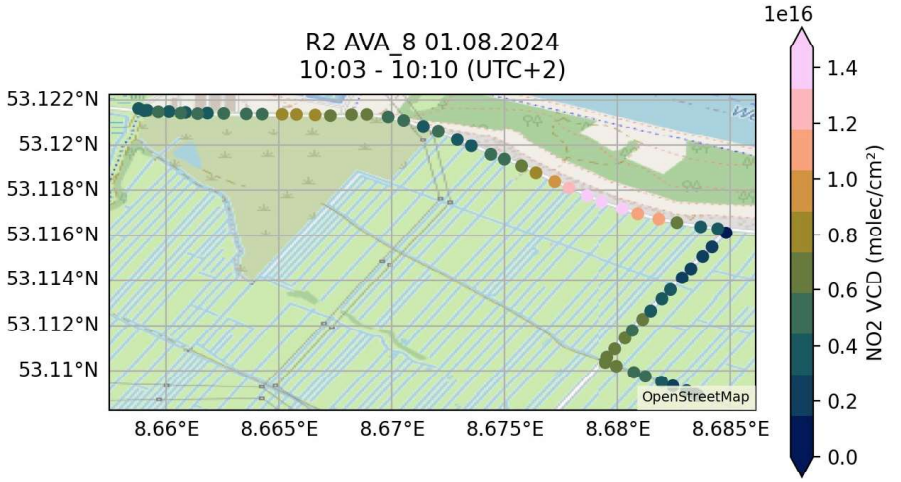

(a)

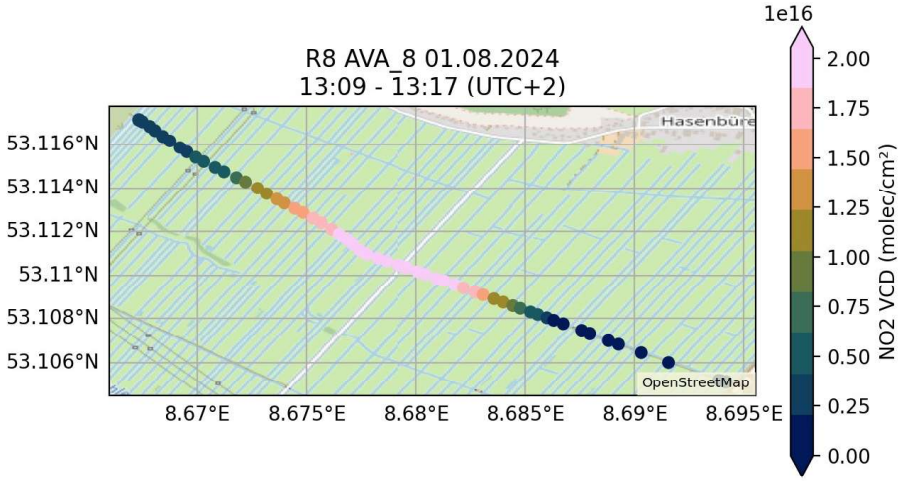

(b)

Figure 4.21: Two plume cross-sections indicated by NO_2 measurements with the DOAS instrument in different distances from the steel plant. (provided by Dr. Lange)

Next, subsequent simultaneous DOAS and EM27/SUN measurements were carried out in two different distances from the source. For these measurements, stationary observations were made every 50 to 100 meters within the expected plume area, with each station being observed for approximately five minutes. A total of 16 stops were used: Stops 1 to 10 were measured between 10:30 and 12:00 local time at a distance of 900 m from the emission stack, and Stops 11 to 16 were measured from 12:10 to 13:00 at a distance of 1400 m. The EM27/SUN measurements had then to be stopped due to excessive cloud cover. The locations of the stops are shown on the map in Figure 4.22.

The XCO_2 and XCO abundances measured with the EM27/SUN illustrated in Figure 4.23 show significant increases due to the steel production site emissions in comparison to the background measured with the 125HR. Emission peaks leading to an increase of the column-averaged mole fraction of approximately 7.5 ppm in XCO_2 and 200 ppb in XCO are observed.

Figure 4.22: Map of the stops for simultaneous measurements of the DOAS and the EM27/SUN.

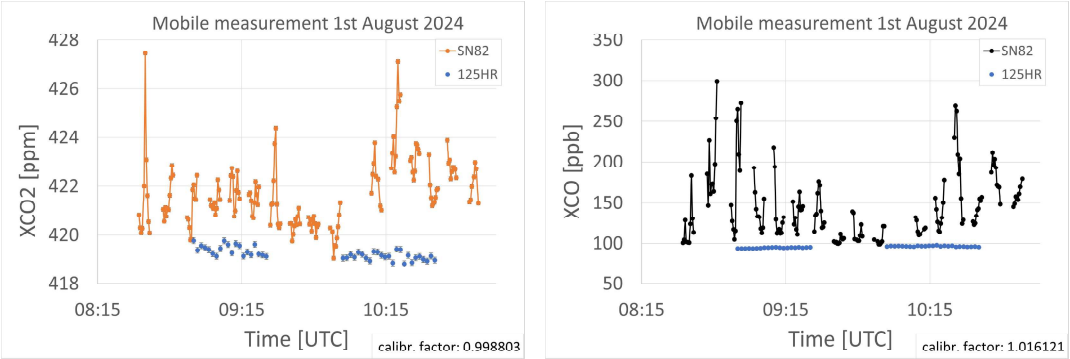

(a) (b)

Figure 4.23: Results of the mobile EM27/SUN measurements showing a) the XCO_2 abundance and b) the XCO abundance both against the corresponding background recorded by the 125HR.

The results of the EM27/SUN are compared to the NO_2 column loads collected with the DOAS instrument as illustrated in Figure 4.24a for all 16 stops. The NO_2 values correspond to a relative difference to background values which were recorded at the beginning of the measurement near the NW1 building and assumed to be near-zero. Each series of connected data points corresponds to a specific measurement stop. The NO_2 values recorded in the same time intervals as the XCO fractions are highlighted in green. The diagram reveals an interesting observation: while there appears to be a potential correlation between the measurements for Measurement Series 2 (the more distant stops 11 to 16), the emission maxima for Measurement Series 1 (Stops 1 to 10) are clearly offset. This offset could potentially be explained by the "viewing geometry", a factor that needs careful consideration when interpreting the data of the two instruments.

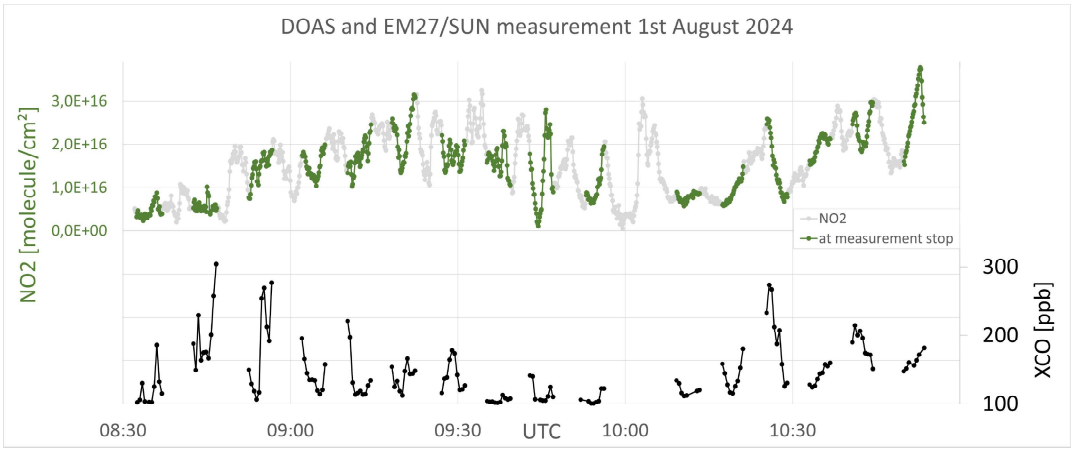

(a)

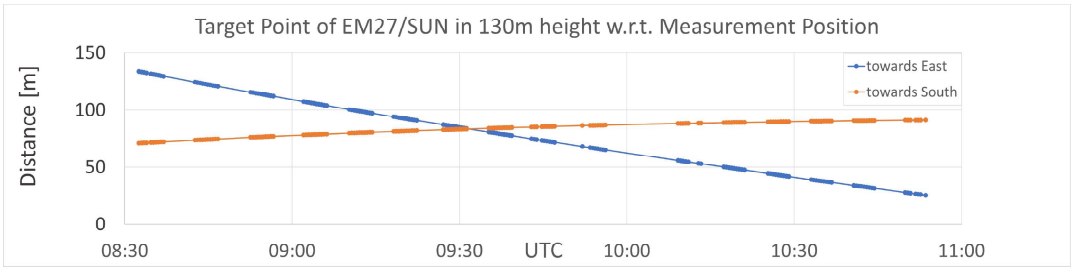

(b)

Figure 4.24: a) Results of the simultaneous DOAS and EM27/SUN measurements showing recorded NO_2 and XCO values. b) Calculated difference in the viewing geometry between the target point of the DOAS instrument and the EM27/SUN for a height of 130 m (average plume height).

In order to provide a clearer understanding of the viewing geometry, calculations were made based on the solar position angles (see Figure 4.24b). These calculations determined the specific point at a height of 130 m (the average plume height according to modeling) that is observed from the EM27/SUN spectrometer in relation to the DOAS measurement point vertically above the measurement stop. Given the north-south movement of the plume, the difference in the east-west direction is particularly important. According to the calculation, at Stop 1 the EM27/SUN targeted a point that was shifted by about 130 m along the plume cross-section; a significant shift compared to the whole plume width of 400 m. As the Sun moved from east to south throughout the day, this distance gradually decreased. However, the north-south shift along the plume's movement direction also needs to be considered, as the plume broadens with increasing distance from the source.

Taking the viewing geometry into account allows for a more refined comparison by shifting the EM27/SUN measurements along the viewing direction (which aligns with the driving direction). This adjustment would bring the two emission maxima measured in NO_2 and XCO for Measurement Series 1 closer together. A shift of approximately 130 m, which corresponds to the distance between two stations for Measurement Series 1, would improve the correlation between the measurements. In contrast, such a shift would degrade the correlation for Measurement Series 2.

However, the influence on Measurement Series 2 is significantly smaller since it was conducted at a greater distance and later point in time and therefore in a wider plume and smaller solar azimuth angle.

A bold assumption underlying this analysis is that the plume remains relatively stationary. This assumption could be validated with further plume modeling. Wind data, which is available in about two months after the measurement, could provide additional confirmation. While stationary measurements already show the temporal fluctuation of the plume, it has to be noted that the distance between the NO_2 minima at Stations 2 and 10 is approximately 400 meters, consistent with the plume width observed in the transect measurement. Similarly, the distance between CO minima at Stations 1 and 8 is around 420 meters, which is measured farther to the south (due to the viewing geometry). This suggests an relative stability of the time-averaged plume direction.

The findings highlight several important conclusions: (1) The use of DOAS measurements to detect emission plumes has been demonstrated to be an effective method; (2) the width of plumes can be accurately measured using DOAS at varying distances, thus providing a means of validating plume models; (3) the ability to calculate the viewing geometry prior to measurements being taken allows for the optimisation of the positioning of the EM27/SUN instrument; and (4) segmented measurements with the EM27/SUN can be challenging due to the long measurement time relative to plume movement. This indicates that stationary EM27/SUN measurements under conditions where the plume traverses the measurement column may prove more effective. Simultaneous DOAS transects can also record the plume behaviour. These findings highlight the additional value of DOAS measurements in achieving accurate and meaningful emission estimates.

Future measurements should also include SO_2 analysis as this might help to disentangle the plumes of the power plant and the steel plant. While NO_2 emissions are only attributed to the steel plant, SO_2 emissions are attributed to both facilities (Umweltbundesamt 2022).

Chapter 5

Conclusion and Outlook

The primary objective of this thesis was to examine and quantify GHG emissions, particularly CO and CO_2 and their emission ratio, from the steel production site in Bremen. This was achieved through the utilisation of advanced measurement and modelling techniques. By employing the EM27/SUN spectrometer, the IFS 125HR spectrometer, a DOAS instrument, and Lagrangian transport models, this study developed a comprehensive methodology for the assessment of emissions from large emission sources and their spatial distribution. The findings of this study provide valuable insights into atmospheric GHG monitoring of single, large emitters.

The first key conclusion is the validation of the EM27/SUN spectrometer as a reliable tool for measuring GHG emissions from stationary and mobile platforms. The stability of the device was demonstrated through the continuous performance of side-by-side measurements. The intercalibration of the EM27/SUN SN82 with the IFS 125HR at the University of Bremen indicates a reliable comparison for XCO_2 and XCH_4 measurements by introducing a constant bias compensation factor of 0.9988 ± 0.0003 and 0.9998 ± 0.0006, respectively. It must be noted that the intercalibration of XCO is of greater concern due to the larger variation observed in the corresponding BCF (0.9974 to 1.0273) on individual days.

The study focused on estimating the XCO/XCO_2 ratio in emissions from the Bremen steel production site. As access was restricted, the emission plume was measured at various locations at varying distances from the emission stacks. It became evident that the reliability of the measurements heavily depends on accurate knowledge of the wind direction, ensuring that the spectrometer is positioned within the plume's trajectory. Additionally, the measurements at more distant stations provided a more consistent representation of the emissions, as the highly variable and narrow plume was challenging to be resolved by the EM27/SUN at nearby sites. Although these measurements resulted in a reproducible CO/CO_2 ratio, this has to be understood as the emission ratio of the entire industrial facility for steel production, including the steel plant and the two associated power plants, rather than a sector-specific steel plant emission ratio.

The steel production site emission ratio obtained by calculating the absolute emission signals was found to be $R = 1.54 \pm 0.85\,\%$. The absolute emissions were obtained by subtracting the background levels measured by the 125HR from the

collected EM27/SUN data. This methodology is based on the assumption that the 125HR accurately reflects the background level at the steel plant. This dependency was mitigated by calculating the ratio exclusively from the EM27/SUN recordings, by considering the alterations in gas abundances introduced by selected emission peaks in both CO and CO_2. The best estimate of the ratio was found to be $R = 1.58 \pm 0.36\,\%$. This result is in accordance with the previously obtained value and with the steel production site emission ratio of 1.49 % as calculated with the data of the thru.de portal. The comparison to the steel plant ratio of $5.09 \pm 0.89\,\%$ calculated based on satellite measurements of CO was attempted by considering the theoretical fraction of CO_2 contributions solely from the steel plant. The revised steel plant emission ratio from the EM27/SUN measurements of $3.46 \pm 0.85\,\%$ is still markedly lower. The discrepancy between the satellite-based measurements and the EM27/SUN recordings can be attributed to a number of potential causes, the precise nature of which requires further investigation.

Table 5.1: CO/CO_2 emission ratios and total CO emissions of the steel plant in Bremen. Comparable values are given in Schneising et al. 2024 and the thru.de portal (Umweltbundesamt 2022).
*no error estimates provided

Quantity	**This thesis**	**Schneising et al.**	**thru.de**
Steel plant CO/CO_2 ratio [%]	3.46 ± 0.85	5.09 ± 0.89	3.33*
Steel production site CO/CO_2 ratio [%]	Met. 2: 1.54 ± 0.85 Met. 3: 1.58 ± 0.36	-	1.49*
CO emissions [kt/yr]	55.06 ± 12.16	92 ± 59	71.9*

The use of a Lagrangian transport model further refined the analysis by simulating the dispersion of the emission plume. The model facilitated the identification of the plume's movement and dilution over time, thereby enhancing the accuracy of the spectrometer data interpretation. This understanding of the plume characteristics presents potential avenues for future in-situ measurements of the plume. The high dispersion of the plume during the day makes direct measurements of CO and CO_2 near the steel plant a promising future investigation. The use of drones to collect air samples at the simulated average plume height can serve for verification. Additionally, the dispersion of the plume in a distinct altitude layer during the night indicates that the plume might be observable with the Tall Tower in Steinkimmen.

Moreover, a quantitative comparison between the measured and modelled data suggested the possibility of total emission estimations based on a straightforward mass balance approach. The resulting CO emission estimate is in good agreement with values obtained in the satellite study and reported in the thru.de portal (refer to Table 5.1). The same does not hold for the CO_2 estimate which has to be simulated by multiple emission sources. Future research should include the use of a more sophisticated plume model that utilises meteorological data of higher resolution (for example, by application of the WRF model) and a priori emission maps in order to allow for backwards Lagrangian inverse modelling. The application of this methodology to additional measurement points in the vicinity of the steel plant, sampling different parts of the plume, appears to offer considerable promise for the accurate

estimation of the total steel production site emissions.

DOAS measurements were determined to be an effective measurement technique for monitoring the plume and its properties in near real-time. Such measurements can be employed for the purpose of verifying simulations of the plume and supporting EM27/SUN measurements. However, the complex difference in the viewing geometry of EM27/SUN and DOAS introduces an additional spatial variation to the temporal variation of the plume, which makes a robust analysis challenging. Future measurements should rely on a stationary measuring EM27/SUN, whose optimal location for the plume measurement can be determined by the DOAS instrument, which can then continuously monitor the behaviour of the plume over time. An additional analysis of SO_2 would possibly allow for a disentanglement of the plumes from the power plant and the steel plant.

In summary, this study identified a number of prospective experiments based on the presented methodology:

1. Should access to the steel production site be granted, it would be beneficial to examine the feasibility of Method 1 (stack tip measurements).

2. Further stationary EM27/SUN measurements in different directions and varying distances from the steel production site are favourable. Such measurements should be accompanied by a DOAS instrument, which would enable the identification of the optimal measurement location and facilitate the continuous monitoring of the emission plume.

3. The modelling approach should be refined by utilising a backwards Lagrangian inverse modelling approach employing the WRF model and a priori emission maps.

4. The results of the DOAS measurements can be further employed for the purpose of validating and constraining the plume model. In addition, an analysis of SO_2 should be included in order to attempt the disentanglement of the steel plant and power plant plume.

5. The EM27/SUN measurements could be expanded to other large emitters.

6. In-situ and drone measurements taken near the steel production site during the daytime could be used to quantify the emission ratio.

7. The potential for quantifying the steel production emissions with the data from the Tall Tower in Steinkimmen on days with favourable wind direction, preferably during nighttime, should be investigated.

In conclusion, this thesis presents a comprehensive investigation into the GHG emissions from the steel production site in Bremen, demonstrating the effectiveness and substantial potential of combining advanced measurement technologies with robust modelling techniques. The findings establish a foundation for future studies and have significant implications for environmental monitoring.

Appendix A

Measurement Data

A.1 Station Setups

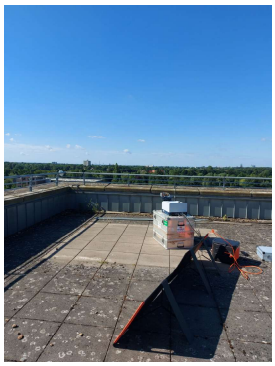

(a) NW1 roof

(b) NW1 dome

(c) Station 1

(d) Station 2

(e) Station 4

(f) Station 7

(g) Station 8

(h) Station 9

Figure A.1: Measurement setup at the different locations.

Table A.1: Locations of the 125HR at NW1 and the 9 measurement stations.

Station	Date	Latitude [°N]	Longitude [°E]
NW1	-	53.10376	8.84952
1	14.05.2024	53.15600	8.62888
2	14.05.2024	53.14510	8.65964
3	16.07.2024	53.12720	8.71050
4	19.07.2024	53.12400	8.66439
5	19.07.2024	53.16220	8.62199
6	25.07.2024	53.14314	8.69015
7	29.07.2024	53.13935	8.69313
8	31.07.2024	53.11760	8.69540
9	31.07.2024	53.11670	8.7057

A.2 Side-by-side Measurements

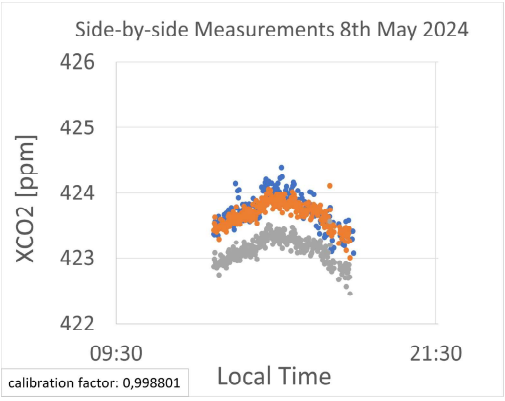

(a)

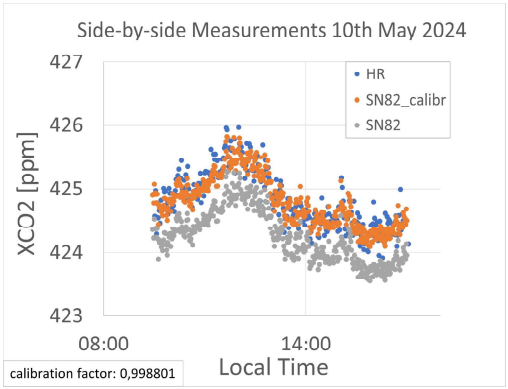

(b)

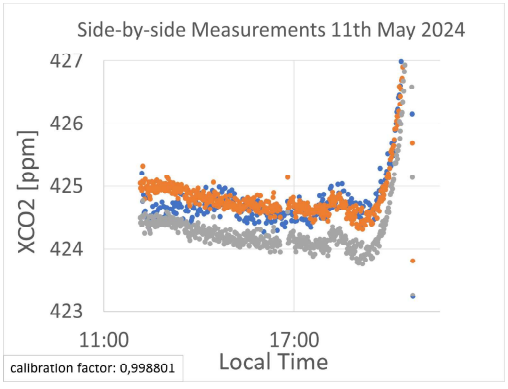

(c)

Figure A.2: XCO_2 abundances measured by the IFS 125HR (blue) and the EM27/SUN SN82 (grey) and its calibrated values (orange) on a) 8th May 2024, b) 10th May 2024 and c) 11th May 2024.

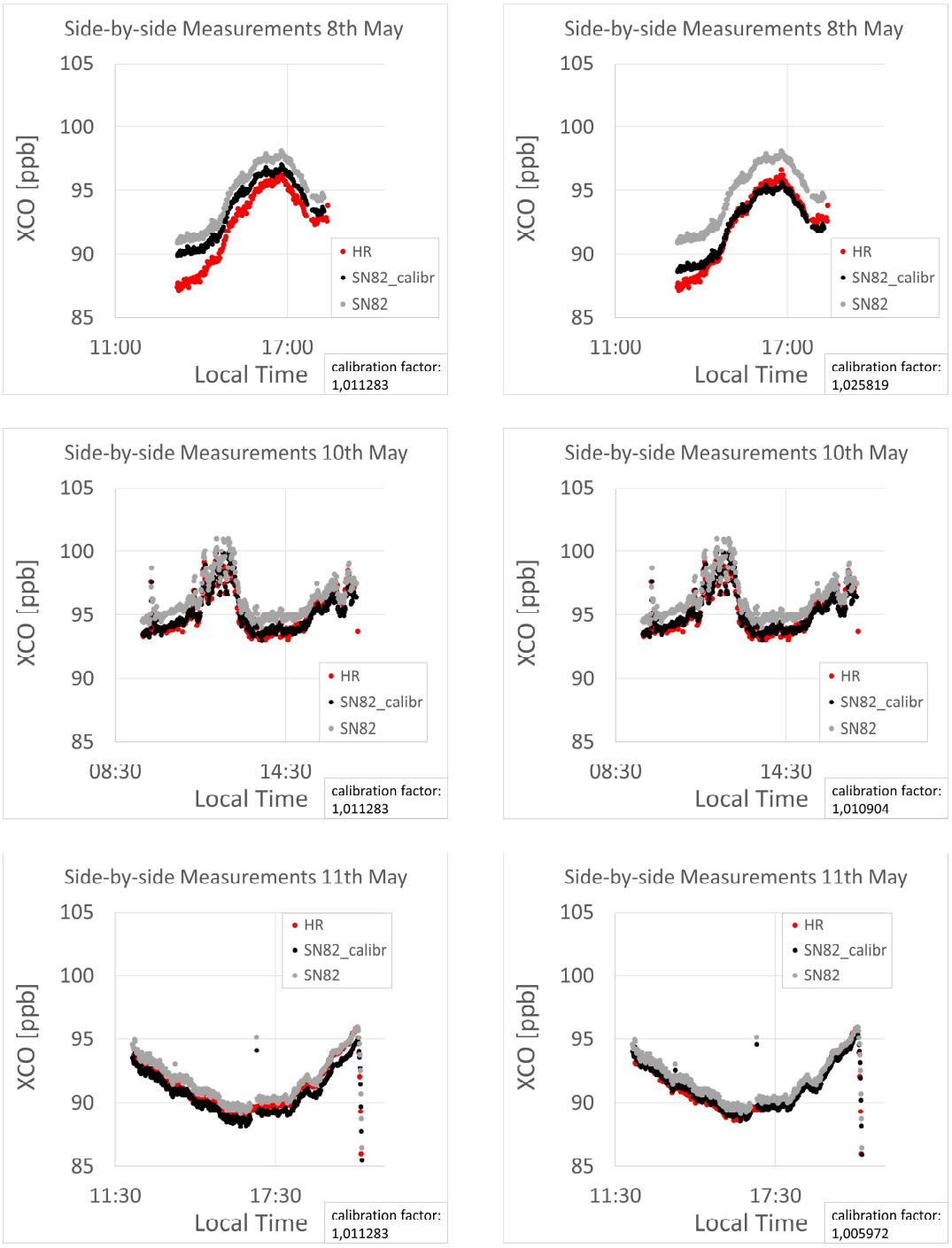

Figure A.3: XCO abundances measured by the IFS 125HR (red) and the EM27/SUN SN82 (grey) and its calibrated values (black) on 8th, 10th and 11th May 2024. The left panel shows the data calibrated according to the mean bias compensation factor and the right panel shows the data calibrated with the daily bias compensation factor.

A.3 Recorded Data

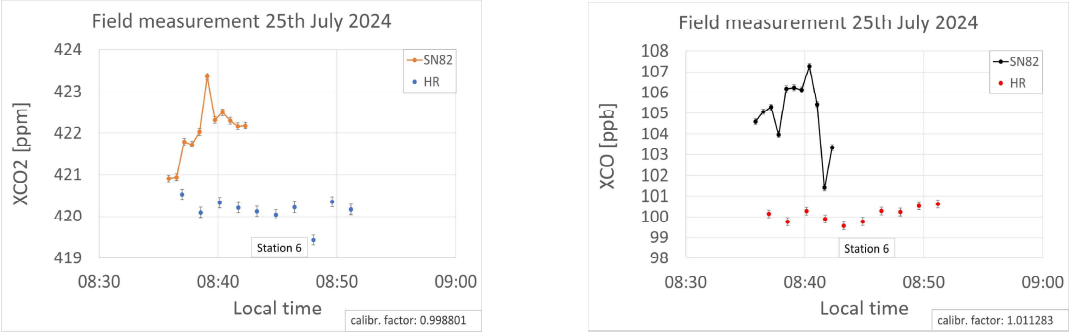

(a) (b)

Figure A.4: XCO2 (a) and XCO (b) abundances recorded with the EM 27/SUN SN82 at Station 6 (orange/black) and the IFS 125HR (blue/red) on 25th July 2024.

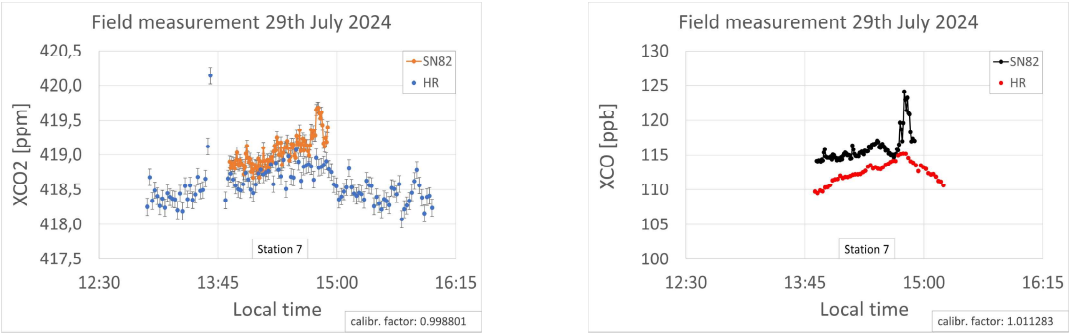

(a) (b)

Figure A.5: XCO2 (a) and XCO (b) abundances recorded with the EM27/ SUN SN82 at Station 7 (orange/black) and the IFS 125HR (blue/red) on 29th July 2024.

A.4 Error Estimation for Single XGas Measurements

To estimate the accuracy of the measurements with the EM27/SUN SN82 and the IFS 125HR spectrometer, the standard deviation was determined. That was done by isolating data in a time interval with linearly changing gas abundance of data filtered as described in Section 4.1.1 as shown in Figure A.6. A trend line for the specific data part was calculated and the difference of the single measurements towards this trend line. The standard deviation in these differences was determined to give an estimate of the accuracy in the single XGas measurement. This procedure was applied to XCO_2, XCO and XCH_4 of both instruments EM27/SUN SN82 and IFS 125HR. They were found to be 0.12 ppm, 0.19 ppb and 0.72 ppb for XCO_2, XCO and XCH_4 for the 125HR, respectively, and 0.08 ppm, 0.14 ppb and 0.47 ppb for the EM27/SUN SN82.

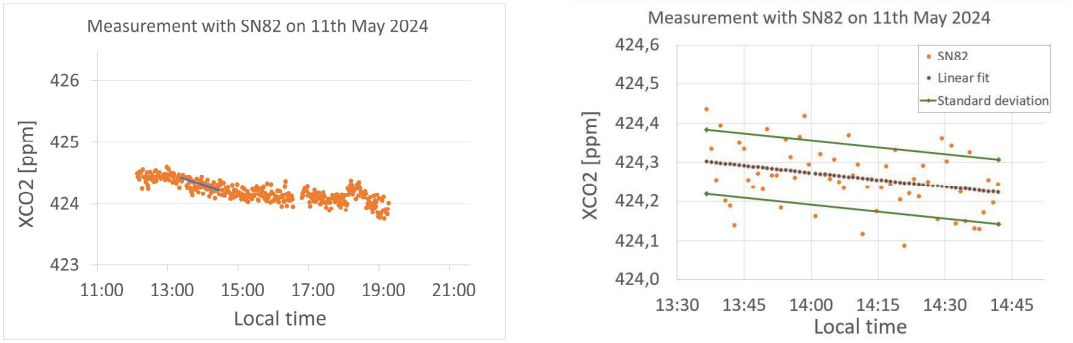

(a) (b)

Figure A.6: a) Specification of a time interval with linearly changing XGas concentration (blue line). b) Determination of the trend line (blue dots) and standard deviation (green line) of the single measurments (orange dots).

A.5 Error Estimation for the Bias Compensation Factor

The optimal bias compensation factor $K_{ref,opt}^{cal}$ of a day is calculated by minimizing the residual between the reference data and the calibrated data. The values used for this procedure are binned average values of single XGas measurements with an error as described in Section A.4. To determine the error of the binned value, the standard error s_i is calculated for each bin according to the equation:

$$s_i = \frac{\sigma_i}{\sqrt{n_i}} \tag{A.1}$$

where σ_i is the error of the single measurement, identical for all data points for the same XGas species and instrument, and n_i is the number of recorded values in bin i.

For each bin, a bias compensation factor $K_{ref,i}^{cal}$ can be calculated according to Equation 4.1. Gaussian error propagation for division leads to an uncertainty calculated by:

$$\sigma_{K_i} = K_i \cdot \sqrt{\left(\frac{s_{cal,i}}{\mathrm{XGas}_i^{cal}}\right)^2 + \left(\frac{s_{ref,i}}{\mathrm{XGas}_i^{ref}}\right)^2} \tag{A.2}$$

The uncertainty in $K_{ref,opt}^{cal}$ is then approximated by the error in the daily mean value of all $K_{ref,i}^{cal}$ according to Gaussian error propagation for addition:

$$\sigma_{K_{opt}} = \sqrt{\frac{\sum_{i=1}^{N} \frac{(K_i - K_{opt})^2}{\sigma_{K_i}^2}}{\sum_{i=1}^{N} \frac{1}{\sigma_{K_i}^2}}} \tag{A.3}$$

where N is the number of bins per day.

A.6 Error Estimation for the XCO/XCO_2 Ratio

Each XGas measurement has an uncertainty σ_{XGas} as described in Section A.4. The XGas value of the emission are for both methods 1 and 2 obtained by taking the difference between two XGas values for the same species, $XGas_{emission}$ = $XGas_1$ - $XGas_2$. The corresponding error is then given by Gaussian error propagation for subtraction:

$$\sigma_{XGas,emission} = \sqrt{\sigma^2_{XGas,1} + \sigma^2_{XGas,2}} \tag{A.4}$$

This applies to both species XCO_2 and XCO. For the calculated ratio

$$R = \frac{\mathrm{XCO}_{emission}}{\mathrm{XCO2}_{emission}} \tag{A.5}$$

the error is given by Gaussian error propagation for division:

$$\sigma_R = R \cdot \sqrt{\left(\frac{\sigma_{XCO,emission}}{XCO_{emission}}\right)^2 + \left(\frac{\sigma_{XCO_2,emission}}{XCO_{2,emission}}\right)^2} \tag{A.6}$$

For method 1 $\sigma_{XGas,1}$ is the uncertainty in the measurement with the EM27/SUN SN82 and $\sigma_{XGas,2}$ is the uncertainty in the measurement with the IFS 125HR. For method 2 $\sigma_{XGas,1}$ and $\sigma_{XGas,2}$ are identical as both values are recorded by the SN82.

The error of the mean ratio is given by its standard deviation.

A.7 Influence of the Choice of Threshold on Calculating the Mean Ratio by XGas Abundance Differences

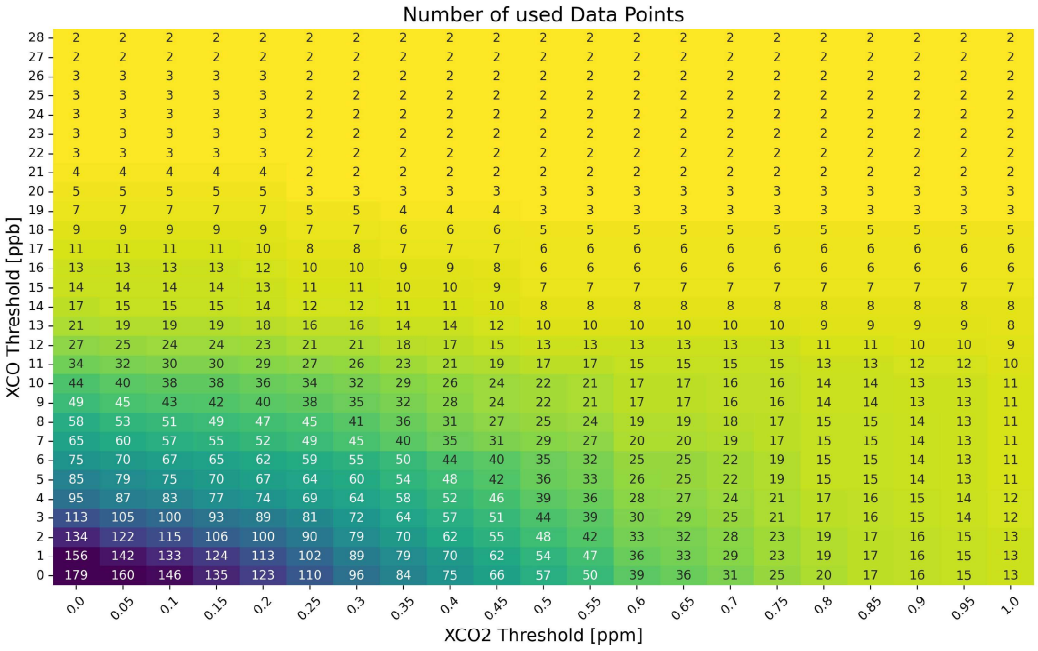

(a)

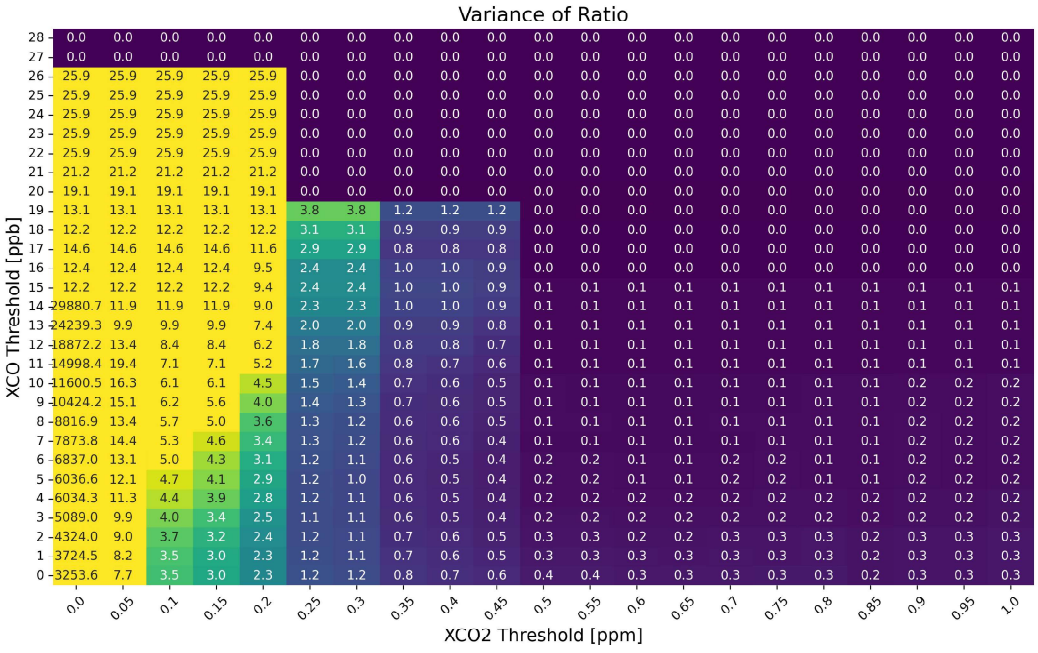

(b)

Figure A.7: a) Number of considered data points for the calculation of the mean ratio and b) its standard deviation; in dependence on the chosen thresholds for XCO and XCO_2.

Appendix B

Programming Details

B.0.1 FLEXPART Simulation Setup

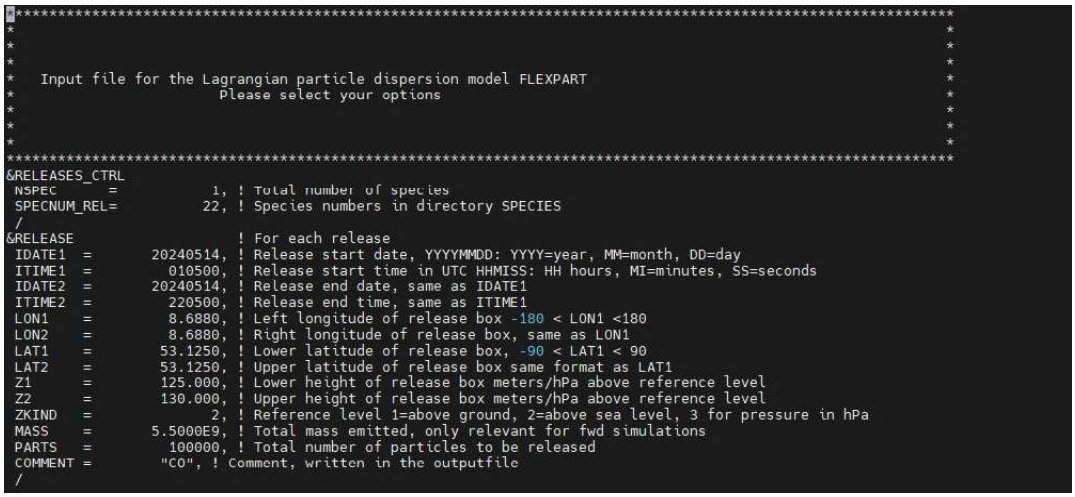

```
*****************************************************************************************************************
*                                                                                                               *
*                                                                                                               *
*                                                                                                               *
*   Input file for the Lagrangian particle dispersion model FLEXPART                                            *
*                        Please select your options                                                             *
*                                                                                                               *
*                                                                                                               *
*                                                                                                               *
*****************************************************************************************************************
&RELEASES_CTRL
 NSPEC      =           1, ! Total number of species
 SPECNUM_REL=          22, ! Species numbers in directory SPECIES
 /
&RELEASE                  ! For each release
 IDATE1  =       20240514, ! Release start date, YYYYMMDD: YYYY=year, MM=month, DD=day
 ITIME1  =         010500, ! Release start time in UTC HHMISS: HH hours, MI=minutes, SS=seconds
 IDATE2  =       20240514, ! Release end date, same as IDATE1
 ITIME2  =         220500, ! Release end time, same as ITIME1
 LON1    =         8.6880, ! Left longitude of release box -180 < LON1 <180
 LON2    =         8.6880, ! Right longitude of release box, same as LON1
 LAT1    =        53.1250, ! Lower latitude of release box, -90 < LAT1 < 90
 LAT2    =        53.1250, ! Upper latitude of release box same format as LAT1
 Z1      =        125.000, ! Lower height of release box meters/hPa above reference level
 Z2      =        130.000, ! Upper height of release box meters/hPa above reference level
 ZKIND   =              2, ! Reference level 1=above ground, 2=above sea level, 3 for pressure in hPa
 MASS    =       5.5000E9, ! Total mass emitted, only relevant for fwd simulations
 PARTS   =         100000, ! Total number of particles to be released
 COMMENT =         "CO", ! Comment, written in the outputfile
 /
```

Figure B.1: FLEXPART Releases File with settings for simulation.

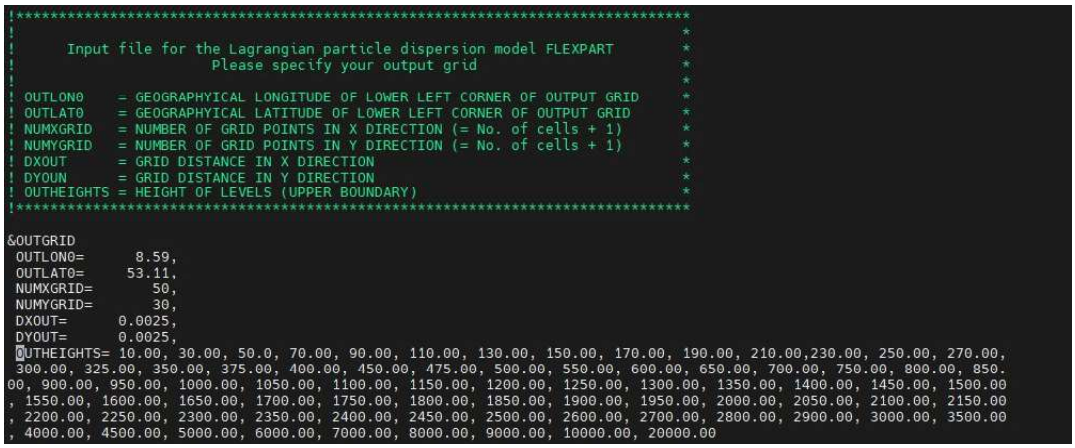

```
!*****************************************************************************
!                                                                            *
!      Input file for the Lagrangian particle dispersion model FLEXPART      *
!                     Please specify your output grid                        *
!                                                                            *
! OUTLON0    = GEOGRAPHYICAL LONGITUDE OF LOWER LEFT CORNER OF OUTPUT GRID   *
! OUTLAT0    = GEOGRAPHYICAL LATITUDE OF LOWER LEFT CORNER OF OUTPUT GRID    *
! NUMXGRID   = NUMBER OF GRID POINTS IN X DIRECTION (= No. of cells + 1)     *
! NUMYGRID   = NUMBER OF GRID POINTS IN Y DIRECTION (= No. of cells + 1)     *
! DXOUT      = GRID DISTANCE IN X DIRECTION                                  *
! DYOUN      = GRID DISTANCE IN Y DIRECTION                                  *
! OUTHEIGHTS = HEIGHT OF LEVELS (UPPER BOUNDARY)                             *
!*****************************************************************************

&OUTGRID
 OUTLON0=      8.59,
 OUTLAT0=     53.11,
 NUMXGRID=       50,
 NUMYGRID=       30,
 DXOUT=      0.0025,
 DYOUT=      0.0025,
 OUTHEIGHTS= 10.00, 30.00, 50.0, 70.00, 90.00, 110.00, 130.00, 150.00, 170.00, 190.00, 210.00,230.00, 250.00, 270.00,
 300.00, 325.00, 350.00, 375.00, 400.00, 450.00, 475.00, 500.00, 550.00, 600.00, 650.00, 700.00, 750.00, 800.00, 850.
00, 900.00, 950.00, 1000.00, 1050.00, 1100.00, 1150.00, 1200.00, 1250.00, 1300.00, 1350.00, 1400.00, 1450.00, 1500.00
, 1550.00, 1600.00, 1650.00, 1700.00, 1750.00, 1800.00, 1850.00, 1900.00, 1950.00, 2000.00, 2050.00, 2100.00, 2150.00
, 2200.00, 2250.00, 2300.00, 2350.00, 2400.00, 2450.00, 2500.00, 2600.00, 2700.00, 2800.00, 2900.00, 3000.00, 3500.00
, 4000.00, 4500.00, 5000.00, 6000.00, 7000.00, 8000.00, 9000.00, 10000.00, 20000.00
```

Figure B.2: FLEXPART Outgrid File with settings for simulation.

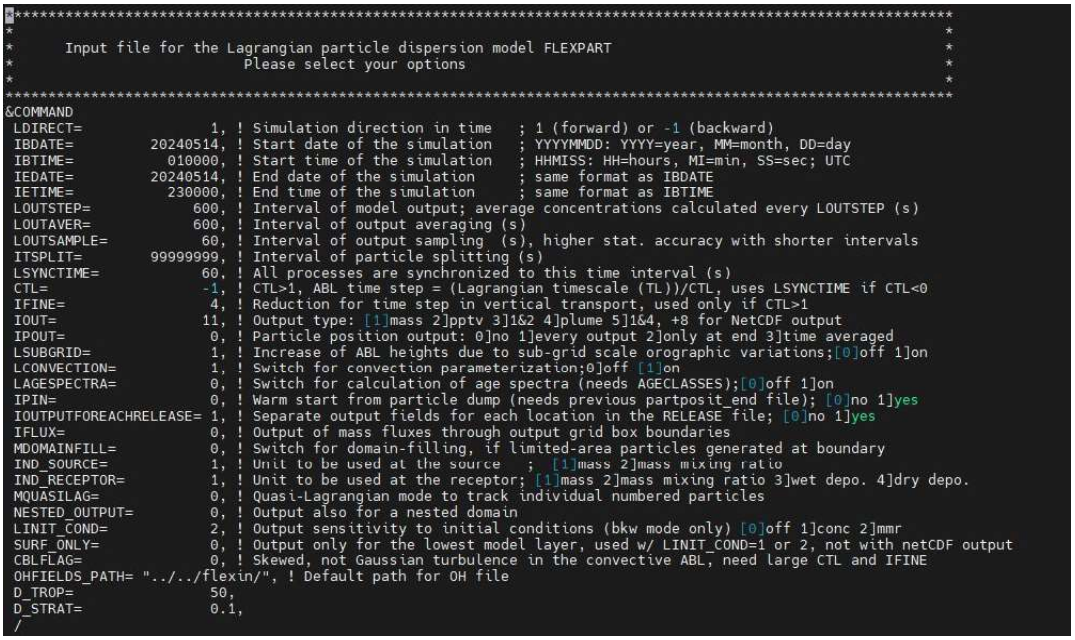

```
*****************************************************************************************************************
*                                                                                                               *
*      Input file for the Lagrangian particle dispersion model FLEXPART                                         *
*                           Please select your options                                                          *
*                                                                                                               *
*****************************************************************************************************************
&COMMAND
 LDIRECT=               1, ! Simulation direction in time   ; 1 (forward) or -1 (backward)
 IBDATE=         20240514, ! Start date of the simulation   ; YYYYMMDD: YYYY=year, MM=month, DD=day
 IBTIME=           010000, ! Start time of the simulation   ; HHMISS: HH=hours, MI=min, SS=sec; UTC
 IEDATE=         20240514, ! End date of the simulation     ; same format as IBDATE
 IETIME=           230000, ! End time of the simulation     ; same format as IBTIME
 LOUTSTEP=            600, ! Interval of model output; average concentrations calculated every LOUTSTEP (s)
 LOUTAVER=            600, ! Interval of output averaging (s)
 LOUTSAMPLE=           60, ! Interval of output sampling  (s), higher stat. accuracy with shorter intervals
 ITSPLIT=        99999999, ! Interval of particle splitting (s)
 LSYNCTIME=           60, ! All processes are synchronized to this time interval (s)
 CTL=                 -1, ! CTL>1, ABL time step = (Lagrangian timescale (TL))/CTL, uses LSYNCTIME if CTL<0
 IFINE=                4, ! Reduction for time step in vertical transport, used only if CTL>1
 IOUT=                11, ! Output type: [1]mass 2]pptv 3]1&2 4]plume 5]1&4, +8 for NetCDF output
 IPOUT=                0, ! Particle position output: 0]no 1]every output 2]only at end 3]time averaged
 LSUBGRID=             1, ! Increase of ABL heights due to sub-grid scale orographic variations;[0]off 1]on
 LCONVECTION=          1, ! Switch for convection parameterization;0]off [1]on
 LAGESPECTRA=          0, ! Switch for calculation of age spectra (needs AGECLASSES);[0]off 1]on
 IPIN=                 0, ! Warm start from particle dump (needs previous partposit_end file); [0]no 1]yes
 IOUTPUTFOREACHRELEASE= 1, ! Separate output fields for each location in the RELEASE file; [0]no 1]yes
 IFLUX=                0, ! Output of mass fluxes through output grid box boundaries
 MDOMAINFILL=          0, ! Switch for domain-filling, if limited-area particles generated at boundary
 IND_SOURCE=           1, ! Unit to be used at the source   ;  [1]mass 2]mass mixing ratio
 IND_RECEPTOR=         1, ! Unit to be used at the receptor; [1]mass 2]mass mixing ratio 3]wet depo. 4]dry depo.
 MQUASILAG=            0, ! Quasi-Lagrangian mode to track individual numbered particles
 NESTED_OUTPUT=        0, ! Output also for a nested domain
 LINIT_COND=           2, ! Output sensitivity to initial conditions (bkw mode only) [0]off 1]conc 2]mmr
 SURF_ONLY=            0, ! Output only for the lowest model layer, used w/ LINIT_COND=1 or 2, not with netCDF output
 CBLFLAG=              0, ! Skewed, not Gaussian turbulence in the convective ABL, need large CTL and IFINE
 OHFIELDS_PATH= "../../flexin/", ! Default path for OH file
 D_TROP=              50,
 D_STRAT=             0.1,
 /
```

Figure B.3: FLEXPART Command File with settings for simulation.

B.0.2 Additional Simulation Plots

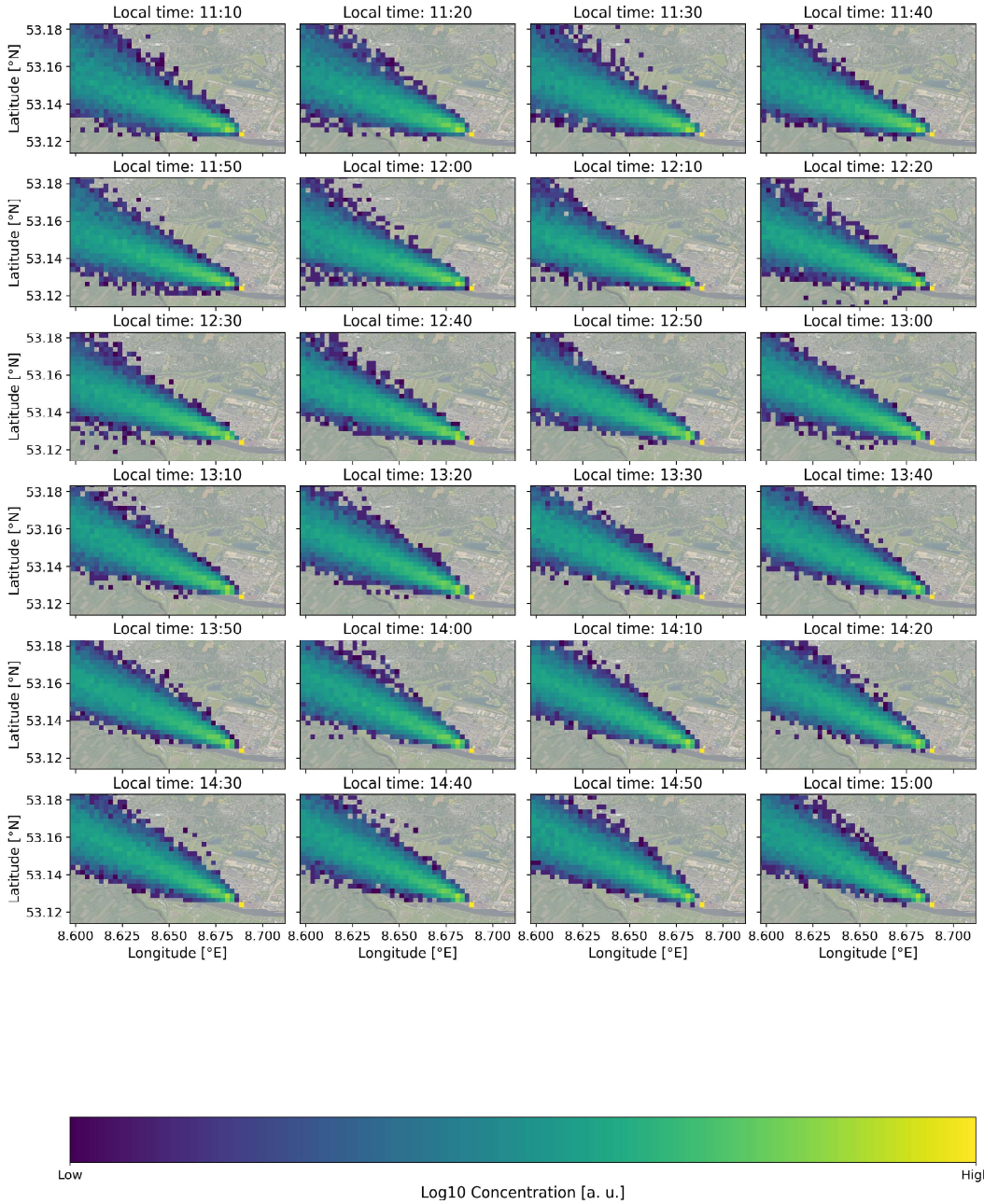

Figure B.4: Plume shape and trajectory simulated with FLEXPART for measurement time on 14th May 2024. The illustrated concentration [mass/area] is given on a log10 scale.

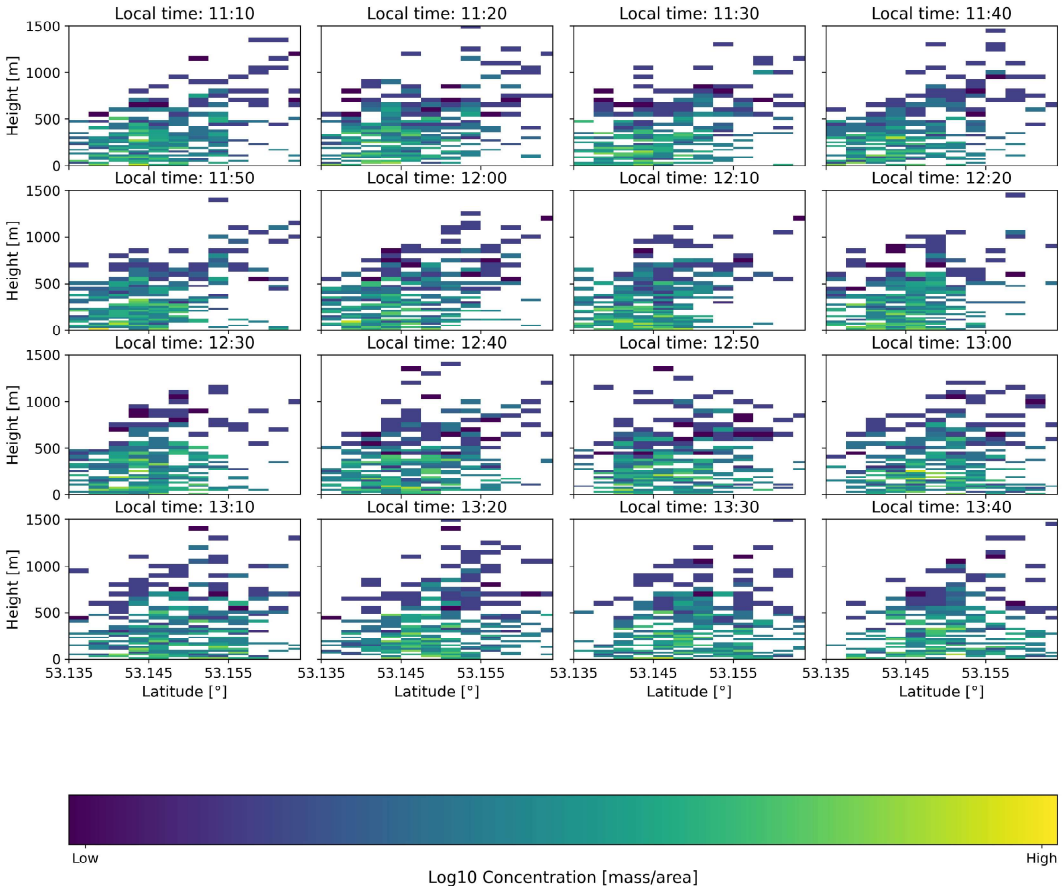

Figure B.5: Plume height at longitude 8.629 °E (Station 1) simulated with FLEXPART for the measurement time on 14th May 2024. The illustrated concentration [mass/area] is given on a log10 scale. Station 1 is located at 53.156 °N measuring south-wards.

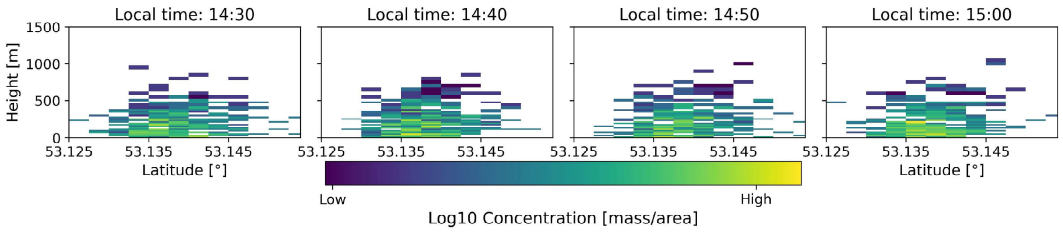

Figure B.6: Plume height at longitude 8.659 °E (Station 2) simulated with FLEXPART for the measurement time on 14th May 2024. The illustrated concentration [mass/area] is given on a log10 scale. Station 2 is located at 53.145 °N measuring south-wards.

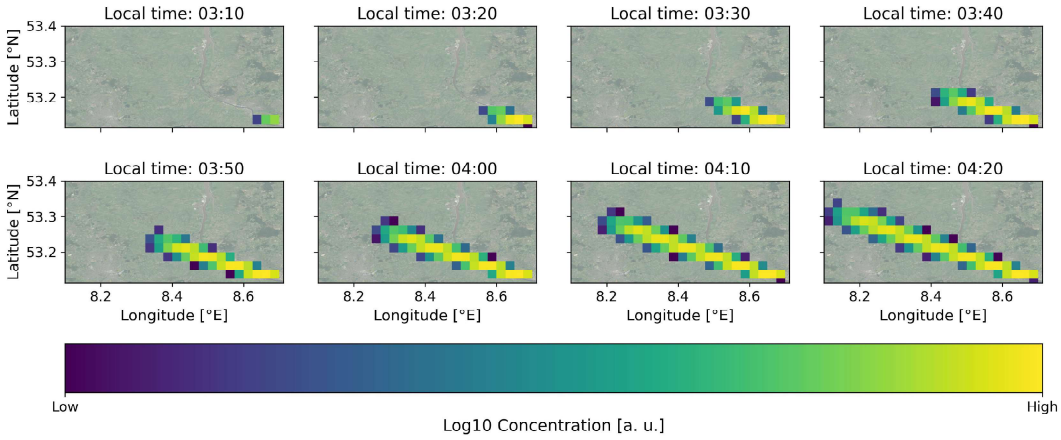

Figure B.7: Plume trajectory simulated with FLEXPART for the hours before sunrise on 14th May 2024 on larger scale. The illustrated concentration [mass/area] is given on a log10 scale.

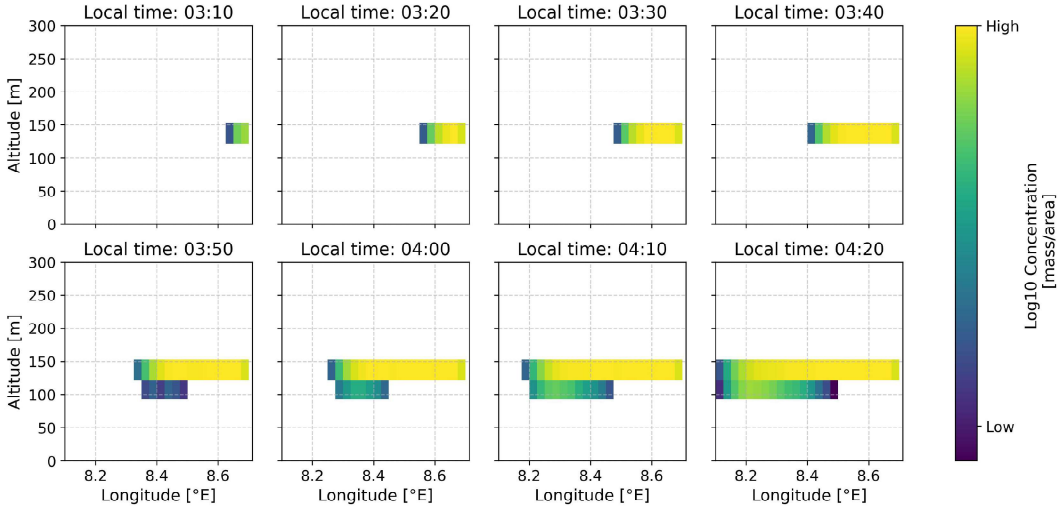

Figure B.8: Plume height simulated with FLEXPART for the hours before sunrise on 14th May 2024 on larger scale. The illustrated concentration [mass/area] is given on a log10 scale.

B.0.3 Python Programs

For this thesis, python codes were written for the calculation of the BCF ('calibration routine.py'), the calculation of the XCO/XCO_2 ratio ('ratios all files.py') and the calculation of the simulated slant column load ('slant columns all.py'). **This link** leads to a GitHub repository containing the used python codes:

https://github.com/lgrosch/Master_Thesis.git

Acronyms

BCF bias compensation factor. 25–28, 32, 35, 47, 53, 68

CH_4 methane. 1, 4, 6, 13, 17, 26–28, 53, 60

CO carbon monoxide. iii, 2–4, 13, 17, 22–24, 26–28, 30, 32–43, 45–47, 49–54, 59, 60, 62, 63, 68

CO_2 carbon dioxide. iii, 1–4, 6, 13, 17, 22–24, 26–28, 30, 32–43, 47, 49, 50, 53, 54, 58, 60, 62, 63, 68

COCCON Collaborative Carbon Column Observing Network. 2

DMF dry-air mole fractions. 2

DOAS Differential Optical Absorption Spectroscopy. iii, v, 21, 22, 24, 48–53, 55

EU ETS European Union Emissions Trading System. 22, 23, 42

FFT Fast Fourier Transform. 12

FLEXPART FLEXible PARTicle dispersion model. 20, 43, 44, 47, 64–68

FTIR Fourier Transform Infrared. 2, 3, 11, 13, 16, 17, 47

FWHM full width at half maximum. 9

GHG greenhouse gas. iii, 1, 3, 6, 7, 18, 22, 23, 53, 55

GOSAT Greenhouse gases Observing SATellite. 1

GPL General Public License. 20

H_2O water vapour. 1, 13

HCHO formaldehyde. 22

HITRAN High-resolution Transmission Molecular Absorption Database. 14

ICOS Integrated Carbon Observation System. 1

ILS instrumental line shape. 17, 25

IMK-ASF Institute for Meteorology and Climate Research - Atmospheric Trace Gases and Remote Sensing. 2

IR infrared. 7, 14

IRWG Infrared Working Group. 2

LPDM Lagrangian Particle Dispersion Mode. 20

MIR mid-infrared. 2, 13

N_2O nitrous oxide. 1, 4, 6, 13

NDACC Network for Detection of Atmospheric Composition Change. 2

NIR near-infrared. 2, 13, 21

NO nitrogen oxide. 48

NO_2 nitrogen dioxide. 22–24, 48–52

O_2 oxygen. 13, 17, 19

O_3 ozone. 22

OPD optical path difference. 2, 11, 12, 17

ppb parts per billion. 4, 26, 28, 32, 35, 37–39, 42, 49, 60

ppm parts per million. 1, 4, 6, 26, 32, 35, 36, 38, 39, 42, 49, 60

RTE radiative transfer equation. 14, 21

SO_2 sulfur dioxide. 22, 23, 52, 55

SZA solar zenith angle. 16, 26

TCCON Total Carbon Column Observing Network. 2

TROPOMI TROPOspheric Monitoring Instrument. 2, 23

UV ultraviolet. 4, 21

VIS visible. 21

VOCs volatile organic compounds. 22

WMO World Meteorological Organisation. 2

WRF Weather Research and Forecasting. 47, 54, 55

Bibliography

Agency, International Energy (2020). *Iron and Steel Technology Roadmap: Towards more sustainable steelmaking*. URL: https://www.iea.org/reports/iron-and-steel-technology-roadmap.

Alberti, C., F. Hase, M. Frey, D. Dubravica, T. Blumenstock, A. Dehn, P. Castracane, G. Surawicz, R. Harig, B. C. Baier, C. Bès, J. Bi, H. Boesch, A. Butz, Z. Cai, J. Chen, S. M. Crowell, N. M. Deutscher, D. Ene, J. E. Franklin, O. García, D. Griffith, B. Grouiez, M. Grutter, A. Hamdouni, S. Houweling, N. Humpage, N. Jacobs, S. Jeong, L. Joly, N. B. Jones, D. Jouglet, R. Kivi, R. Kleinschek, M. Lopez, D. J. Medeiros, I. Morino, N. Mostafavipak, A. Müller, H. Ohyama, P. I. Palmer, M. Pathakoti, D. F. Pollard, U. Raffalski, M. Ramonet, R. Ramsay, M. K. Sha, K. Shiomi, W. Simpson, W. Stremme, Y. Sun, H. Tanimoto, Y. Té, G. M. Tsidu, V. A. Velazco, F. Vogel, M. Watanabe, C. Wei, D. Wunch, M. Yamasoe, L. Zhang, and J. Orphal (2022). "Improved calibration procedures for the EM27/SUN spectrometers of the COllaborative Carbon Column Observing Network (COCCON)". In: *Atmospheric Measurement Techniques* 15.8, pp. 2433–2463. DOI: 10.5194/amt-15-2433-2022. URL: https://amt.copernicus.org/articles/15/2433/2022/.

ASHRAE (1996). *Handbook: Systems and Equipment*. Atlanta, GA: ASHRAE.

Bergamaschi, P., A. Colomb, M. De Mazière, L. Emmenegger, D. Kubistin, I. Lehner, K. Lehtinen, M. Leuenberger, C. Lund Myhre, M. Marek, S. M. Platt, C. Plaß-Dulmer, M. Ramonet, M. Schmidt, F. Apadula, S. Arnold, H. Chen, S. Conil, C. Couret, P. Cristofanelli, G. Forster, J. Hatakka, M. Heliasz, O. Hermansen, A. Hoheisel, T. Kneuer, T. Laurila, A. Leskinen, J. Levula, M. Lindauer, M. Lopez, I. Mammarella, G. Manca, F. Meinhardt, J. Muller-Williams, M. Ottosson-Löfvenius, S. Piacentino, J. Pitt, B. Scheeren, M. Schumacher, M. K. Sha, P. Smith, M. Steinbacher, L. L. Sørensen, G. Vítková, C. Yver-Kwok, A. di Sarra, F. Conen, V. Kazan, Y.-A. Roulet, T. Biermann, M. Delmotte, D. Heltai, K. Komínková, O. Laurent, C. Lunder, P. Marklund, J.-M. Pichon, P. Trisolino, ICOS Atmosphere Thematic Centre, ICOS ERIC - Carbon Portal, ICOS Flask, Calibration Laboratory (FCL), and ICOS Central Radiocarbon Laboratory (CRL) (2022). *ICOS Atmosphere Release 2022-1 of Level 2 Greenhouse Gas Mole Fractions of CO2, CH4, N2O, CO, meteorology and 14CO2*. Data set. DOI: 10.18160/KCYX-HA35.

Burchart-Korol, D. (2013). "Life cycle assessment of steel production in Poland: a case study". In: *Journal of Cleaner Production* 54, pp. 235–243. DOI: 10.1016/j.jclepro.2013.04.031. URL: https://doi.org/10.1016/j.jclepro.2013.04.031.

Burrows, J. P., U. Platt, and P. Borrell (2011). *Tropospheric Remote Sensing from Space*. The Remote Sensing of Tropospheric Composition from Space. Springer

Berlin Heidelberg, pp. 1–65. ISBN: 978-3-642-14791-3. DOI: 10.1007/978-3-642-14791-3_1.

Butz, A., A. S. Dinger, N. Bobrowski, J. Kostinek, L. Fieber, C. Fischerkeller, G. B. Giuffrida, F. Hase, F. Klappenbach, J. Kuhn, P. Lubcke, L. Tirpitz, and Q. Tu (2017). "Remote sensing of volcanic CO2, HF, HCl, SO2, and BrO in the downwind plume of Mt. Etna". In: *Atmospheric Measurement Techniques* 10.1, pp. 1–14. DOI: 10.5194/amt-10-1-2017.

Butz, A., V. Hanft, R. Kleinschek, M. Frey, A. Muller, M. Knapp, I. Morino, A. Agusti-Panareda, F. Hase, J. Landgraf, S. Vardag, and H. Tanimoto (2022). "Versatile and Targeted Validation of Space-Borne XCO2, XCH4 and XCO Observations by Mobile Ground-Based Direct-Sun Spectrometers". In: *Frontiers in Remote Sensing* 2. ISSN: 2673-6187. DOI: 10.3389/frsen.2021.775805.

Climate Change (IPCC), Intergovernmental Panel on (2023). "Technical Summary". In: *Climate Change 2021 – The Physical Science Basis: Working Group I Contribution to the Sixth Assessment Report of the Intergovernmental Panel on Climate Change*. Cambridge University Press, pp. 35–144.

Crippa, M., E. Solazzo, G. Huang, D. Guizzardi, E. Koffi, M. Muntean, C. Schieberle, R. Friedrich, and G. Janssens-Maenhout (2020). "High resolution temporal profiles in the Emissions Database for Global Atmospheric Research". In: *Scientific Data* 7, p. 121. DOI: 10.1038/s41597-020-0462-2. URL: https://doi.org/10.1038/s41597-020-0462-2.

Crommelynck, D., A. Fichot, V. Domingo, and R. III Lee (1996). "SOLCON Solar Constant Observations from the ATLAS Missions". In: *Geophysical Research Letters* 23.17, pp. 2293–2295. DOI: 10.1029/96GL01878.

Cusworth, D. H., R. M. Duren, A. K. Thorpe, M. L. Eastwood, R. O. Green, P. E. Dennison, C. Frankenberg, J. W. Heckler, G. P. Asner, and C. E. Miller (2021). "Quantifying Global Power Plant Carbon Dioxide Emissions With Imaging Spectroscopy". In: *AGU Advances* 2.2. DOI: 10.1029/2020AV000350.

Davis, S., M. C. Abrams, and J. W. Brault (2010). *Fourier Transform Spectrometry*. Academic Press, pp. 190–198.

Demtröder, Wolfgang (2018). *Atoms, Molecules and Photons: An Introduction to Atomic-, Molecular- and Quantum Physics*. Graduate Texts in Physics. (cit. on pp. 13–14, 17–18). Berlin, Heidelberg: Springer. ISBN: 978-3-662-55521-7. DOI: 10.1007/978-3-662-55523-1.

Dietrich, F., J. Chen, B. Voggenreiter, P. Aigner, N. Nachtigall, and B. Reger (2021). "MUCCnet: Munich Urban Carbon Column network". In: *Atmospheric Measurement Techniques* 14.2, pp. 1111–1126. DOI: 10.5194/amt-14-1111-2021.

Douville, H., K. Raghavan, J. Renwick, R. Allan, P. Arias, M. Barlow, R. Cerezo-Mota, A. Cherchi, T. Gan, J. Gergis, D. Jiang, A. Khan, W. Pokam Mba, D. Rosenfeld, J. Tierney, and O. Zolina (2021). "Water Cycle Changes". In: *Climate Change 2021: The Physical Science Basis. Contribution of Working Group I to the Sixth Assessment Report of the Intergovernmental Panel on Climate Change*. Ed. by V. Masson-Delmotte, P. Zhai, A. Pirani, S. Connors, C. Pean, S. Berger, N. Caud, Y. Chen, L. Goldfarb, M. Gomis, M. Huang, K. Leitzell, E. Lonnoy, J. Matthews, T. Maycock, T. Waterfield, O. Yelekçi, R. Yu, and B. Zhou. Cambridge, United Kingdom and New York, NY, USA: Cambridge University Press, pp. 1055–1210. DOI: 10.1017/9781009157896.010.

Efremenko, D. and A. Kokhanovsky (2021). *Foundations of Atmospheric Remote Sensing*. cit. on pp. 8, 11, 32. Cham: Springer International Publishing. ISBN: 978-3-030-66744-3. DOI: 10.1007/978-3-030-66745-0.

Fox-Kemper, B., H. Hewitt, C. Xiao, G. Adalgeirsdóttir, S. Drijfhout, T. Edwards, N. Golledge, M. Hemer, R. Kopp, G. Krinner, A. Mix, D. Notz, S. Nowicki, I. Nurhati, L. Ruiz, J.-B. Sallée, A. Slangen, and Y. Yu (2021). "Ocean, Cryosphere and Sea Level Change". In: *Climate Change 2021: The Physical Science Basis. Contribution of Working Group I to the Sixth Assessment Report of the Intergovernmental Panel on Climate Change*. Ed. by V. Masson-Delmotte, P. Zhai, A. Pirani, S. Connors, C. Pean, S. Berger, N. Caud, Y. Chen, L. Goldfarb, M. Gomis, M. Huang, K. Leitzell, E. Lonnoy, J. Matthews, T. Maycock, T. Waterfield, O. Yelekçi, R. Yu, and B. Zhou. Cambridge, United Kingdom and New York, NY, USA: Cambridge University Press, pp. 1211–1362. DOI: 10.1017/9781009157896.011.

Frey, M., F. Hase, T. Blumenstock, J. Groß, M. Kiel, G. Mengistu Tsidu, K. Schäfer, M. K. Sha, and J. Orphal (2015). "Calibration and instrumental line shape characterization of a set of portable FTIR spectrometers for detecting greenhouse gas emissions". In: *Atmospheric Measurement Techniques* 8.7, pp. 3047–3057. DOI: 10.5194/amt-8-3047-2015. URL: https://amt.copernicus.org/articles/8/3047/2015/.

Frey, M., M. K. Sha, F. Hase, M. Kiel, T. Blumenstock, R. Harig, G. Surawicz, N. M. Deutscher, K. Shiomi, J. E. Franklin, H. Bösch, J. Chen, M. Grutter, H. Ohyama, Y. Sun, A. Butz, G. Mengistu Tsidu, D. Ene, D. Wunch, Z. Cao, O. Garcia, M. Ramonet, F. Vogel, and J. Orphal (2019). "Building the COllaborative Carbon Column Observing Network (COCCON): Long-term Stability and Ensemble Performance of the EM27/SUN Fourier Transform Spectrometer". In: *Atmospheric Measurement Techniques* 12.3, pp. 1513–1530. DOI: 10.5194/amt-12-1513-2019.

Fröhlich, C. and J. Lean (Dec. 2004). "Solar radiative output and its variability: evidence and mechanisms". In: *The Astronomy and Astrophysics Review* 12.4, pp. 273–320. ISSN: 1432-0754. DOI: 10.1007/s00159-004-0024-1.

Gisi, M., F. Hase, S. Dohe, T. Blumenstock, A. Simon, and A. Keens (2012). "XCO2-Measurements with a Tabletop FTS Using Solar Absorption Spectroscopy". In: *Atmospheric Measurement Techniques* 5.11, pp. 2969–2980. DOI: 10.5194/amt-5-2969-2012.

Gordon, I. et al. (2022). "The HITRAN2020 Molecular Spectroscopic Database". In: *Journal of Quantitative Spectroscopy and Radiative Transfer* 277, p. 107949. ISSN: 0022-4073. DOI: 10.1016/j.jqsrt.2021.107949.

Griffith, P. R. and J. A. de Haseth (2007). *Fourier Transform Infrared Spectrometry*. English. Hoboken: John Wiley & Sons.

Hall, Bradley D., Allan M. Crotwell, David R. Kitzis, Timothy Mefford, Benjamin R. Miller, Martin F. Schibig, and Pieter P. Tans (2021). "Revision of the World Meteorological Organization Global Atmosphere Watch (WMO/GAW) CO_2 calibration scale". In: *Atmospheric Measurement Techniques* 14.4, pp. 3015–3032. DOI: 10.5194/amt-14-3015-2021.

Hase, F., M. Frey, T. Blumenstock, J. Groß, M. Kiel, R. Kohlhepp, G. Mengistu Tsidu, K. Schäfer, M. K. Sha, and J. Orphal (2015). "Application of portable FTIR spectrometers for detecting greenhouse gas emissions of the major city

Berlin". In: *Atmospheric Measurement Techniques* 8.7, pp. 3059–3068. DOI: 10.5194/amt-8-3059-2015.

Hase, F., M. Frey, M. Kiel, T. Blumenstock, R. Harig, A. Keens, and J. Orphal (2016). "Addition of a Channel for XCO Observations to a Portable FTIR Spectrometer for Greenhouse Gas Measurements". In: *Atmospheric Measurement Techniques* 9.5, pp. 2303–2313. DOI: 10.5194/amt-9-2303-2016.

Hedelius, J. K., C. Viatte, D. Wunch, C. M. Roehl, G. C. Toon, J. Chen, T. Jones, S. C. Wofsy, J. E. Franklin, H. Parker, M. K. Dubey, and P. O. Wennberg (2016). "Assessment of Errors and Biases in Retrievals of XCO_2, XCH_4, XCO, and XN_2O from a 0.5 cm^{-1} Resolution Solar-Viewing Spectrometer". In: *Atmospheric Measurement Techniques* 9, pp. 3527–3546. DOI: 10.5194/amt-9-3527-2016.

Herkommer, B., C. Alberti, P. Castracane, J. Chen, A. Dehn, F. Dietrich, N. M. Deutscher, M. M. Frey, J. Groß, L. Gillespie, F. Hase, I. Morino, N. M. Pak, B. Walker, and D. Wunch (2024). "Using a portable FTIR spectrometer to evaluate the consistency of Total Carbon Column Observing Network (TCCON) measurements on a global scale: the Collaborative Carbon Column Observing Network (COCCON) travel standard". In: *Atmospheric Measurement Techniques* 17.11, pp. 3467–3494. DOI: 10.5194/amt-17-3467-2024. URL: https://amt.copernicus.org/articles/17/3467/2024/.

Herkommer, Benedikt (2024). "Improving the consistency of greenhouse gas measurements from ground-based remote sensing instruments using a portable FTIR spectrometer". Karlsruher Institut für Technologie (KIT). DOI: 10.5445/IR/1000168723.

Hodson, E. L., B. Poulter, N. E. Zimmermann, C. Prigent, and J. O. Kaplan (2011). "The El Niño–Southern Oscillation and wetland methane interannual variability". In: *Geophysical Research Letters* 38.8. DOI: 10.1029/2011GL046861.

Hoffman, Thorsten (2024). *Sonnenverlauf*. Version Version 2024-08. URL: https://www.sonnenverlauf.de/#/53.1249,8.7286,16/2024.07.29/16:30/250/1.

IMK-ASF (Dec. 2023). *PROFFAST User Manual*. [Accessed 31 Aug 2024]. Institute for Meteorology, Climate Research - Atmospheric Trace Gases, and Remote Sensing. URL: https://www.imk-asf.kit.edu/downloads/Coccon/PROFFAST_User-Manual_Dec-2023.pdf.

IMK-ASF, KIT (2023). *IMK-ASF - About IMK-ASF - Research Groups - Ground-Based Remote Sensing - COCCON - Column Sensitivities*. https://www.imk-asf.kit.edu/english/3330.php. [Accessed 31 Aug 2024].

Ishioka, M., T. Okada, and K. Matsubara (1992). "Formation and characteristics of vapor grown carbon fibers prepared in Linz-Donawitz converter gas". In: *Carbon* 30, pp. 975–979. DOI: 10.1016/0008-6223(92)90124-F. URL: https://doi.org/10.1016/0008-6223(92)90124-F.

Jones, P. D., M. New, D. E. Parker, S. Martin, and I. G. Rigor (1999). "Surface air temperature and its changes over the past 150 years". In: *Reviews of Geophysics* 37.2, pp. 173–199. DOI: 10.1029/1999RG900002.

Keppel-Aleks, G., G. C. Toon, P. O. Wennberg, and N. M. Deutscher (2007). "Reducing the Impact of Source Brightness Fluctuations on Spectra Obtained by Fourier-Transform Spectrometry". In: *Applied Optics* 46, pp. 4774–4779. DOI: 10.1364/AO.46.004774.

Kim, T. W., S. S. Bae, J. W. Lee, S.-M. Lee, J.-H. Lee, H. S. Lee, and S. G. Kang (2016). "A biological process effective for the conversion of CO-containing

industrial waste gas to acetate". In: *Bioresource Technology* 211, pp. 792–796. DOI: 10.1016/j.biortech.2016.04.038. URL: https://doi.org/10.1016/j.biortech.2016.04.038.

Kivi, R. and P. Heikkinen (2016). "Fourier transform spectrometer measurements of column CO_2 at Sodankylä, Finland". In: *Geoscientific Instrumentation, Methods and Data Systems* 5, pp. 271–279. DOI: 10.5194/gi-5-271-2016. URL: https://doi.org/10.5194/gi-5-271-2016.

Klappenbach, F., M. Bertleff, J. Kostinek, F. Hase, T. Blumenstock, A. Agusti-Panareda, M. Razinger, and A. Butz (2015). "Accurate mobile remote sensing of XCO2 and XCH4 latitudinal transects from aboard a research vessel". In: *Atmospheric Measurement Techniques* 8.12, pp. 5023–5038. DOI: 10.5194/amt-8-5023-2015.

Klose, B. and H. Klose (2016). "Die Erdatmosphäre: Ihre chemische Zusammensetzung, vertikale Struktur und Physik". In: *Meteorologie: Eine interdisziplinäre Einführung in die Physik der Atmosphäre*. Berlin, Heidelberg: Springer Berlin Heidelberg, pp. 15–81. ISBN: 978-3-662-43622-6. DOI: 10.1007/978-3-662-43622-6_2.

Knapp, M., R. Kleinschek, F. Hase, A. Agusti-Panareda, A. Inness, J. Barre, J. Landgraf, T. Borsdorff, S. Kinne, and A. Butz (2021). "Shipborne measurements of XCO2, XCH4, and XCO above the Pacific Ocean and comparison to CAMS atmospheric analyses and S5P/TROPOMI". In: *Earth System Science Data* 13.1, pp. 199–211. DOI: 10.5194/essd-13-199-2021.

Kurylo, M. J. (1991). "Network for the Detection of Stratospheric Change". In: *Remote Sensing of Atmospheric Chemistry*. Ed. by J. L. McElroy and R. J. McNeal. Vol. 1491. Proceedings of SPIE. International Society for Optics and Photonics (SPIE), pp. 168–174. DOI: 10.1117/12.46658.

Lan, X., K. W. Thoning, and E. J. Dlugokencky (2024). *Trends in globally-averaged CH4, N2O, and SF6 determined from NOAA Global Monitoring Laboratory measurements*. Version Version 2024-07. DOI: 10.15138/P8XG-AA10. URL: https://doi.org/10.15138/P8XG-AA10.

Lin, J., D. Brunner, C. Gerbig, A. Stohl, A. Luhar, and P. Webley (2012). "Lagrangian Modeling of the Atmosphere". In: *Geophysical Monograph Series. American Geophysical Union*. DOI: 10.1029/gm200.

Liu, Y., J. Lin, G. Huang, Y. Guo, and C. Duan (May 2001). "Simple empirical analytical approximation to the Voigt profile". In: *Journal of the Optical Society of America B* 18.5, pp. 666–672. DOI: 10.1364/JOSAB.18.000666.

Luther, A., R. Kleinschek, L. Scheidweiler, S. Defratyka, M. Stanisavljevic, A. Forstmaier, A. Dandocsi, S. Wolff, D. Dubravica, N. Wildmann, J. Kostinek, P. Jöckel, A.-L. Nickl, T. Klausner, F. Hase, M. Frey, J. Chen, F. Dietrich, J. Nkcki, J. Swolkień, A. Fix, A. Roiger, and A. Butz (2019). "Quantifying CH_4 Emissions from Hard Coal Mines Using Mobile Sun-Viewing Fourier Transform Spectrometry". In: *Atmospheric Measurement Techniques* 12, pp. 5217–5230. DOI: 10.5194/amt-12-5217-2019.

MacDonald, C. G., J.-P. Mastrogiacomo, J. L. Laughner, J. K. Hedelius, R. Nassar, and D. Wunch (2023). "Estimating Enhancement Ratios of Nitrogen Dioxide, Carbon Monoxide, and Carbon Dioxide Using Satellite Observations". In: *Atmospheric Chemistry and Physics* 23, pp. 3493–3516. DOI: 10.5194/acp-23-3493-2023.

Meinshausen, Malte, Elmar Vogel, Alexander Nauels, Katja Lorbacher, Nicolai Meinshausen, David M. Etheridge, Paul J. Fraser, Stephen A. Montzka, Peter J. Rayner, Cathy M. Trudinger, Paul B. Krummel, Urs Beyerle, Josep G. Canadell, John S. Daniel, Ian G. Enting, Rachel M. Law, Chris R. Lunder, Simon O'Doherty, Ronald G. Prinn, Stefan Reimann, Mauro Rubino, Guus J. M. Velders, Martin K. Vollmer, Ray H. J. Wang, and Ray Weiss (2017). "Historical greenhouse gas concentrations for climate modelling (CMIP6)". In: *Geoscientific Model Development* 10.5, pp. 2057–2116. DOI: 10.5194/gmd-10-2057-2017.

Möller, D. (Feb. 2019). *Volume 1 Fundamentals and Processes*. De Gruyter. ISBN: 978-3-11-056126-5. DOI: 10.1515/9783110561265.

NOAA (2023). *Greenhouse gases continued to increase rapidly in 2022*. Accessed: 2023-11-14. URL: https://www.noaa.gov/news-release/greenhouse-gases-continued-to-increase-rapidly-in-2022.

Park, H., S. Jeong, H. Park, L. D. Labzovskii, and K. W. Bowman (2021). "An assessment of emission characteristics of Northern Hemisphere cities using spaceborne observations of CO_2, CO, and NO_2". In: *Remote Sensing of Environment* 254, p. 112246. DOI: 10.1016/j.rse.2020.112246. URL: https://doi.org/10.1016/j.rse.2020.112246.

Platt, Ulrich and Jochen Stutz (2008). *Differential Optical Absorption Spectroscopy*. Physics of Earth and Space Environments. Springer-Verlag Berlin Heidelberg. ISBN: 978-3-540-75775-7. DOI: 10.1007/978-3-540-75776-4.

Poulidis, Alexandros Panagiotis (2021). *Lagrangian Trajectory modeling with FLEXPART*. URL: https://www.msc-ep.uni-bremen.de/services/lectures/practicals/pr_trajectories_2021.pdf. (version: 10.04.2021).

Rodgers, C. (2000). *Inverse Methods for Atmospheric Sounding: Theory and Practice*. Series on Atmospheric, Oceanic and Planetary Physics. World Scientific Publishing Company. ISBN: 9789814498685.

Roedel, W. and T. Wagner (2017). *Physik unserer Umwelt: Die Atmosphäre*. cit. on pp. 6–8. Berlin, Heidelberg: Springer Berlin Heidelberg. ISBN: 978-3-662-54257-6. DOI: 10.1007/978-3-662-54258-3.

Schneising, O., M. Buchwitz, M. Reuter, M. Weimer, H. Bovensmann, J. P. Burrows, and H. Bösch (2024). "Towards a Sector-Specific CO/CO_2 Emission Ratio: Satellite-Based Observation of CO Release from Steel Production in Germany". In: *EGUsphere* 2024, pp. 1–17. DOI: 10.5194/egusphere-2023-2709. URL: https://egusphere.copernicus.org/preprints/2024/egusphere-2023-2709/.

Schulze, E.-D. (2006). "Biological control of the terrestrial carbon sink". In: *Biogeosciences* 3.2, pp. 147–166. DOI: 10.5194/bg-3-147-2006.

Seibert, P. and A. Frank (2004). "Source-receptor matrix calculation with a Lagrangian particle dispersion model in backward mode". In: *Atmospheric Chemistry and Physics* 4, pp. 51–63.

Seneviratne, S., X. Zhang, M. Adnan, W. Badi, C. Dereczynski, A. Di Luca, S. Ghosh, I. Iskandar, J. Kossin, S. Lewis, F. Otto, I. Pinto, M. Satoh, S. Vicente-Serrano, M. Wehner, and B. Zhou (2021). "Weather and Climate Extreme Events in a Changing Climate". In: *Climate Change 2021: The Physical Science Basis. Contribution of Working Group I to the Sixth Assessment Report of the Intergovernmental Panel on Climate Change*. Ed. by V. Masson-Delmotte, P. Zhai, A. Pirani, S. Connors, C. Pean, S. Berger, N. Caud, Y. Chen, L. Gold-

farb, M. Gomis, M. Huang, K. Leitzell, E. Lonnoy, J. Matthews, T. Maycock, T. Waterfield, O. Yelekçi, R. Yu, and B. Zhou. Cambridge, United Kingdom and New York, NY, USA: Cambridge University Press, pp. 1513–1766. DOI: 10.1017/9781009157896.013.

Stohl, A., S. Eckhardt, C. Forster, P. James, N. Spichtinger, and P. Seibert (2002). "A replacement for simple back trajectory calculations in the interpretation of atmospheric trace substance measurements". In: *Atmospheric Environment* 36 (29), pp. 4635–4648. DOI: 10.1016/s1352-2310(02)00416-8.

Stohl, A., P. Seibert, M. Cassiani, D. Arnold, D. Morton, S. Riddick, and T. Arnold (2023). *FLEXPART Version 10.4 User Manual*. Last accessed: 12 December 2023. URL: https://www.flexpart.eu/downloads/26.

Suer, J., M. Traverso, and N. Jäger (2022). "Review of Life Cycle Assessments for Steel and Environmental Analysis of Future Steel Production Scenarios". In: *Sustainability* 14. DOI: 10.3390/su142114131. URL: https://doi.org/10.3390/su142114131.

Tian, Y., Y. Sun, T. Borsdorff, C. Liu, T. Liu, Y. Zhu, H. Yin, and J. Landgraf (2022). "Quantifying CO emission rates of industrial point sources from Tropospheric Monitoring Instrument observations". In: *Environmental Research Letters* 17, p. 014057. DOI: 10.1088/1748-9326/ac3b1a. URL: https://doi.org/10.1088/1748-9326/ac3b1a.

Tu, Q., F. Hase, M. Schneider, O. Garcia, T. Blumenstock, T. Borsdorff, M. Frey, F. Khosrawi, A. Lorente, C. Alberti, J. J. Bustos, A. Butz, V. Carreno, E. Cuevas, R. Curcoll, C. J. Diekmann, D. Dubravica, B. Ertl, C. Estruch, S. F. Leon-Luis, C. Marrero, J.-A. Morgui, R. Ramos, C. Scharun, C. Schneider, E. Sepulveda, C. Toledano, and C. Torres (2022a). "Quantification of CH_4 emissions from waste disposal sites near the city of Madrid using ground- and space-based observations of COCCON, IASI". In: *Atmospheric Chemistry and Physics* 22.1, pp. 295–317. DOI: 10.5194/acp-22-295-2022.

Tu, Q., F. Hase, M. Schneider, O. Garcia, T. Blumenstock, T. Borsdorff, M. Frey, F. Khosrawi, A. Lorente, C. Alberti, J. J. Bustos, A. Butz, V. Carreño, E. Cuevas, R. Curcoll, C. J. Diekmann, D. Dubravica, B. Ertl, C. Estruch, S. F. León-Luis, C. Marrero, J.-A. Morgui, R. Ramos, C. Scharun, C. Schneider, E. Sepúlveda, C. Toledano, and C. Torres (2022b). "Quantification of CH_4 emissions from waste disposal sites near the city of Madrid using ground- and space-based observations of COCCON, IASI". In: *Atmospheric Chemistry and Physics* 22.1, pp. 295–317. DOI: 10.5194/acp-22-295-2022.

Umweltbundesamt (2022). URL: https://thru.de/.

United-Nations (2015). *The Paris Agreement*. https://unfccc.int/process-and-meetings/the-paris-agreement. Accessed: 2024-08-28.

Veefkind, J., I. Aben, K. McMullan, H. Förster, J. de Vries, G. Otter, J. Claas, H. Eskes, J. de Haan, Q. Kleipool, M. van Weele, O. Hasekamp, R. Hoogeveen, J. Landgraf, R. Snel, P. Tol, P. Ingmann, R. Voors, B. Kruizinga, R. Vink, H. Visser, and P. Levelt (2012). "TROPOMI on the ESA Sentinel-5 Precursor: A GMES mission for global observations of the atmospheric composition for climate, air quality and ozone layer applications". In: *Remote Sensing of Environment* 120, pp. 70–83. ISSN: 0034-4257. DOI: 10.1016/j.rse.2011.09.027.

Wolf, Hans C. and Hermann Haken (2006). *Molekülphysik und Quantenchemie*. Springer-Lehrbuch. (cit. on pp. 13–14, 17–18). Berlin/Heidelberg: Springer-Verlag. ISBN: 978-3-540-30314-5. DOI: 10.1007/3-540-30315-4.

Wu, D., J. Liu, P. O. Wennberg, P. I. Palmer, R. R. Nelson, M. Kiel, and A. Eldering (2022). "Towards Sector-Based Attribution Using Intra-City Variations in Satellite-Based Emission Ratios Between CO2 and CO". In: *Atmospheric Chemistry and Physics* 22, pp. 14547–14570. DOI: 10.5194/acp-22-14547-2022.

Wunch, D., G. C. Toon, J.-F. L. Blavier, R. A. Washenfelder, J. Notholt, B. J. Connor, D. W. T. Griffith, V. Sherlock, and P. O. Wennberg (2011). "The Total Carbon Column Observing Network". In: *Philosophical Transactions of the Royal Society A: Mathematical, Physical and Engineering Sciences* 369.1943, pp. 2087–2112. DOI: 10.1098/rsta.2010.0240.

Yokota, T., Y. Yoshida, N. Eguchi, Y. Ota, T. Tanaka, H. Watanabe, and S. Maksyutov (2009). "Global Concentrations of CO_2 and CH_4 Retrieved from GOSAT: First Preliminary Results". In: *SOLA* 5, pp. 160–163. DOI: 10.2151/sola.2009-041.